Title
The AGN origin of cluster magnetic fields

Author
Xu, Hao

Publication Date
2009

UNIVERSITY OF CALIFORNIA, SAN DIEGO

The AGN Origin of Cluster Magnetic Fields

A dissertation submitted in partial satisfaction of the
requirements for the degree
Doctor of Philosophy

in

Physics

by

Hao Xu

Committee in charge:

Professor Michael L. Norman, Chair
Professor Patrick H. Diamond, Co-Chair
Professor Paolo Padoan
Professor Kevin B. Quest
Professor Barney J. Rickett

2009

The dissertation of Hao Xu is approved, and it is acceptable in quality and form for publication on microfilm and electronically:

Co-Chair

Chair

University of California, San Diego

2009

DEDICATION

To my parents.
And to Liming, My Love.

TABLE OF CONTENTS

LIST OF FIGURES

LIST OF TABLES

ACKNOWLEDGEMENTS

I would like to extend my deepest thanks to my thesis advisor, Michael Norman. His support and guidance has made the completion of this research possible. I thank for his incisive comments, questions and suggestions. In addition, I would like to thank my mentor in Los Alamos National Laboratory, Hui Li, who more than other person is responsible for getting me involved in this research. I thank him for his support and hosting me at LANL. I also thank him for alway giving me the best advice on what to do when difficulties arise.

I would like to thank my thesis committee, Patrick Diamond, Paolo Padoan, Kevin Quest, and Barney Rickett for their participation and useful comments.

Many thanks go to David Collins for writing MHD version of Enzo, for useful discussions, and for all of the technical support that he has given me over the years. I would not have been able to complete this work without his hard work on MHD version of Enzo. Many thanks also go to Shengtai Li for his MHD solver, which is essential to finish this work. Many thanks go to Brian O'Shea for his very useful advise.

I would like to thank my collaborators and scientific peers. In particular, I would like to thank Stirling Colgate, Steven Diehl, Ozgur Gurcan, Phil Kronberg, Shiming Liu, Wei Liu, Masanori Nakamura, Stephen Skory, Geoffrey So, Rick Wagner, Daniel Whalen, and Cong Yu.

I would also like to thank Debra Bomar, Elizabeth Daniels, Jenny Esch, Hilari Ford, Dayna Gallegos, Kay Grady, and Andi Stephens for their extremely efficient administrative support. I would also like to thank my friends Xi Chen, Zhiqiang Li, Liang Jing, Sen Yang, Eric Yu, and Lei Zhu who let me have wonderful life during my PhD study.

I would like to thank my parents for their support. Last, I would like to thank Liming for her understanding, encouragement and support.

This work was completed with support from the Center for Astrophysics and Space Sciences and the Department of Physics at the University of California in San Diego, NSF grant AST-07089960 and NRAC allocation MCA98N020. In addition, this work has been supported from the Theoretical Division of Los Alamos National

Laboratory by IGPP grant.

Chapter 2, in part, has been submitted for publication of the material as it may appear in the Astrophysical Journal Supplement Series, 2009. Collins, David C.; Xu, Hao; Norman, Michael L.; Li, Hui; Li, Shengtai, "Cosmological AMR MHD with Enzo" IOP Publishing, 2009. The dissertation author was the primary investigator and author of this paper.

Chapter 3, in part, is the material as it appears in the Astrophysical Journal, 688, L57-L60, 2008 Xu, Hao; O'Shea Brian W.; Collins, David C.; Norman, Michael L.; Li, Hui; Li, Shengtai, "The Biermann Battery in Cosmological MHD Simulations of Population III Star Formation" the University of Chicago Press, 2008. The dissertation author was the primary investigator and author of this paper.

Chapter 4, in part, is the material as it appears in the Astrophysical Journal, 681, L61-L64, 2008 Xu, Hao; Li, Hui; Collins, David C.; Li, Shengtai; Norman, Michael L., "Formation of X-Ray Cavities by the Magnetically Dominated Jet-Lobe System in a Galaxy Cluster" the University of Chicago Press, 2008. The dissertation author was the primary investigator and author of this paper.

Chapter 5, in part, is the material as it appears in the Astrophysical Journal, 2009. Xu, Hao; Li Hui; Collins, David C.; Li, Shengtai; Norman, Michael L., "Turbulence and Dynamo in Galaxy Cluster Medium : Implications on the Origin of Cluster Magnetic Fields", IOP Publishing, 2009. The dissertation author was the primary investigator and author of this material.

Appendix A, in full, has been submitted for publication of the material as it may appear in the Astrophysical Journal Supplement Series, 2009. Collins, David C.; Xu, Hao; Norman, Michael L.; Li, Hui; Li, Shengtai, "Cosmological AMR MHD with Enzo" IOP Publishing, 2009. The dissertation author was the primary investigator and author of this paper.

VITA

2000	B. Sc. in Physics, Sun Yat-sen University, Guangzhou, China
2000-2002	Graduate Teaching Assistant, University of Hong Kong, Hong Kong, China
2002	M. Phil. in Physics, University of Hong Kong, Hong Kong, China
2002-2003	Graduate Teaching Assistant, University of California, San Diego
2003-2008	Graduate Research Assistant, University of California, San Diego
2006-2009	Graduate Research Assistant, Los Alamos National Laboratory
2009	Ph. D. in Physics, University of California, San Diego

PUBLICATIONS

K. M. Lee, H. Xu, and H. F. Chau, "Parity Problem with a Cellular Automaton Solution", *Physical Review E*, 64 (2): Art. No.026702 Part 2, 2001.

X. Q. Luo, H. Xu, J. C. Yang et.al., "(3+1)-Dimensional Quantum Mechanics from Monte Carlo Hamiltonian: Harmonic Oscillator", *Communications in Theoretical Physics* 36 (1): 7-10, 2001.

H. F. Chau, H. Xu, and L. G. Liu, "Exactly Solvable Single Lane Highway Traffic Model with Tollbooths", *Physica A*, 303 (3-4): 534-542, 2002.

H. F. Chau, H. Xu, K. M. Lee, L. W. Siu and K. K. Yan, "Finding the Sign of a Function Value by Binary Cellular Automaton", *International Journal of Modern Physics C*, 13 (10): 1347-1364 2002.

H. Xu, K. M. Lee, and H. F. Chau, "Modulo Three Problem with a Cellular Automaton Solution", *International Journal of Modern Physics C*, 14 (3): 249-256, 2003.

H. Xu, H. Li, D. C. Collins, S. Li, and M. L. Norman, "Formation of X-Ray Cavities by the Magnetically Dominated Jet-Lobe System in a Galaxy Cluster", *The Astrophysical Journal*, 681, L61-L64, 2008.

H. Xu, B. W. O'Shea, D. C. Collins, M. L. Norman, H. Li, and S. Li, "The Biermann Battery in Cosmological MHD Simulations of Population III Star Formation", *The Astrophysical Journal*, 688, L57-L60, 2008.

H. Xu, H. Li, D. C. Collins, S. Li, and M. L. Norman, "Turbulence and Dynamo in Galaxy Cluster Medium : Implications on the Origin of Cluster Magnetic Fields", *The Astrophysical Journal*, 698, L14-L17, 2009.

D. C. Collins, H. Xu, M. L. Norman, H. Li, and S. Li, "Cosmological AMR MHD with Enzo", *The Astrophysical Journal Supplement Series*, 2009, summitted.

ABSTRACT OF THE DISSERTATION

The AGN Origin of Cluster Magnetic Fields

by

Hao Xu
Doctor of Philosophy in Physics

University of California San Diego, 2009

Professor Michael L. Norman, Chair

Professor Patrick H. Diamond, Co-Chair

The origin of magnetic fields in galaxy clusters is one of the most fascinating but challenging problems in astrophysics. In this dissertation, the possibility of an Active Galactic Nucleus (AGN) origin of cluster magnetic fields is studied through state of the art simulations of magnetic field evolution in large scale structure formation using a newly developed cosmological Adaptive Mesh Refinement (AMR) Magnetohydrodynamics (MHD) code – EnzoMHD. After presenting a complete but concise description and verification of the code, we discuss the creation of magnetic fields through the Biermann Battery effect during first star formation and galaxy cluster formation. We find that magnetic fields are produced as predicted by theory in both cases. For the first star formation, we obtain a lower limit of ($\sim 10^{-9}$ G) for magnetic fields when the first generation stars form. On the other hand, we find that the magnetic energy is amplified 4 orders of magnitude within $\sim$ 10 Gyr during cluster formation. We then study magnetic field injection from AGN into the Intra-Cluster Medium (ICM) and their impact on the ICM. We reproduce the X-ray cavities as well as weak shocks seen in observations in the simulation, and further confirm the idea that AGN outburst must contain lots of magnetic energy (up to 10^{61} ergs) and the magnetic fields play an important part in the formation of jet/lobe system. We present high resolution simulations of cluster formation with magnetic fields injected from high redshift AGN. We find that these local magnetic fields are spread quickly throughout the whole cluster by cluster mergers. The ICM is in a turbulent state with a Kolmogorov-like power spectrum. Magnetic fields are amplified to and maintained at the observational level of a few μG by bulk flows at large scale and the ICM turbulence at small scale. The total magnetic energy increases about 25 times to $\sim 1.2 \times 10^{61}$ ergs at the present time. We conclude that magnetic fields from AGN at high redshift may provide sufficient initial magnetic fields to magnetize the whole cluster.

Chapter 1

Introduction

Magnetic fields are an important ingredient of our universe. They are present in astronomical objects of almost all scales and plays important roles in many phenomena. In our own planet, the earth has a dipolar magnetic field with a strength of 0.6 G at the poles and 0.3 G at the equator. These fields protect human beings from the high energy cosmic ray particles. The magnetic fields in the Sun contribute to the spectacular phenomena, such as sunspots, arches, and flares. These solar activities have big impacts on people's lives and have recently been linked to climate change. For galactic systems, the Milky Way's Interstellar Medium (ISM) has a highly organized magnetic field with about 2 μG on kpc scale, with a disordered component on smaller scales which is about two and a half times larger than the ordered component (Binney & Merrifield, 1998). Outside of the Milky Way, various observations also confirmed that magnetic fields exist in galaxies of all types as well as galaxy clusters, the largest virialized systems in the universe (Widrow, 2002). In the past, when large-scale structure formations are studied numerically, magnetic fields are usually ignored, due to their limited contribution to the dynamics at large scales and, more importantly, the numerical difficulties to handle them correctly.

In the early stage, numerical simulations of large-scale structure formation (such as formation of galaxy clusters) have been primarily used to constrain cosmological parameters and to reject ideas such as the concept of "hot dark matter". Due to recent observational, theoretical, and computational advances, cosmological parameters are now known to approximately 10% accuracy. This new epoch of "precision cosmology" has encouraged a renaissance in computational astrophysics. With the rapid advances in the constraint of the basic cosmological parameters and other advances in observations, numerical simulations of large-scale structure formation can be used in a predictive sense, to study the formation of distant and highly nonlinear objects (like the first generation stars), which are too complicated to approach purely analytically. Now, new efforts are underway to increase cosmological parameters' precision to 1%. To achieve this precision in simulations, the nonthermal components, like magnetic fields and cosmic rays, can no longer be ignored.

This dissertation presents the newly developed cosmological AMR MHD code – EnzoMHD with the testing and verification of the code, and the results of numerical simulations of large-scale structure formation with magnetic fields. We compute the effect of seed fields generated by the Biermann Battery effect in Population III star formation as well as in galaxy cluster formation. We discuss the evolution of magnetic fields from the AGN outburst and the formation of magnetically driven X-ray cavities. Then we predict how the magnetic fields from AGNs may magnetize the whole cluster to the observed level. In this chapter, we will review the research on the magnetic fields in galaxy clusters, and discuss the cosmological simulations with magnetic fields.

1.1 Magnetic Fields in Galaxy Clusters

1.1.1 Observations of Cluster Magnetic Fields

The most direct way to detect cluster magnetic fields is to observe the synchrotron radiation from clusters. An extended radio source was first found in the Coma cluster 50 years ago by Large et al. (1959). A detailed study performed by Willson (1970) found that this radio source was a smooth "radio halo" not associated with any galaxy. He also concluded that the radio emission was likely from synchrotron radiation, and if there is an equipartion between magnetic field energy and relativistic particle kinetic energy, leads to a magnetic field strength of $\sim 2\ \mu G$. From then on, high sensitivity radio observations have revealed that in about 50 clusters there are diffuse radio sources, not associated with active galaxies but with the Intracluster Medium

(ICM) (Ferrari et al., 2008). These radio halos typically are extended (∼1Mpc) and close to the cluster center defined by the X-ray emission. Radio observations also find that magnetic fields are present at the outskirts of galaxy clusters, where radio sources, known as radio relics, are observed.

Magnetic field strength and configuration is usually estimated by assuming a minimal energy configuration for the total energy in relativistic particles and magnetic fields (Burbidge, 1959). Using this method, magnetic field strengths are found to be 0.1-1 μG permeating the cluster volume (Feretti, 1999). The accuracy of measuring magnetic field strength is further limited by the poorly constrained parameters of relativistic particles. Magnetic fields can also be derived without this minimum energy assumption by comparing inverse Compton (IC) X-ray emission and synchrotron radiation (Harris & Grindlay, 1979; Rephaeli et al., 1987). In typical astrophysical circumstances, inverse Compton hard X-rays are produced from up-scattering of the cosmic microwave background (CMB) photon field by the same relativistic particle population, which generates the synchrotron emission. By comparing IC X-ray emission and synchrontron radiation and with the knowledge of the CMB photon field, the magnetic field strength in clusters is estimated to be 0.2-1 μG (see review by Carilli & Taylor, 2002). This method is also not very accurate, since it has a major drawback that the IC hard X-ray is contaminated by the cluster hot plasma emission.

Faraday rotation measure of distant polarized radio sources is another available way that can be used to detect and probe cluster magnetic fields. For a distant polarized source, the rotation measure (RM), which is defined as ratio of change of polarization angle to wavelength squared, in unit of rad m^{-2}, is (Kronberg et al., 2008):

$$RM(z_s) = \frac{\delta\chi}{\lambda^2} = 8.1 \times 10^5 \int_0^{z_s} \frac{n_e(z)B_{||}(z)}{(1+z)^2}\frac{dl}{dz}dz \tag{1.1}$$

where n_e is free electron number density in cm^{-3}, $B_{||}$ is the line of sign component of magnetic fields in Gauss, and dl/dz is the comoving path increment per unit redshift in parsec. Since n_e is relatively easy to measure in galaxy cluster by fitting the thermal X-ray emission, the RM can be use to estimate the magnetic fields in the cluster in front of the radio source. Since the integration is from source to observer, the component outside of the cluster should be deducted first and the result also depends on the assumed topology of magnetic fields. Also, more than one polarization angel at different wavelengths are needed to be measured to determine RM to remove nπ degeneracy.

The RM distributions for radio sources (jet/lobes) at the centers of galaxy clusters are used to estimate the magnetic field strength and configurations. These RMs are found to be patchy, with alternating high and low RM bands, in cluster centers. These indicate that magnetic fields reverse their directions on the scales of the bands $\sim 10s$ kpc. In Hydra A, which is a cool core cluster, RMs in the north lobe are positive, and in the south lobe are negative, both with band width ~10 kpc. It implies that there is a lager-scale B-field component reversed at scale ~100 kpc in addition to the reversal fields at smaller scale. Taylor & Perley (1993) derived the large-scale field strength to be ~7 μG and small-scale field strength to be ~40 μG. For non-cool core clusters, the magnetic field strength is usually smaller, and the fields reverse direction at larger lengths.

In addition, RM may provide more information about cluster magnetic fields than their strength and directions. Vogt & Enßlin (2005) derived a Kolmogorov-like magnetic field power spectrum of the center of Hydra A using its RM map. RMs from far away sources can also be used to study the magnetic fields in the high redshift systems located in the sightline of the sources (Kronberg et al., 2008). This research suggests that magnetic fields are already present at normal galaxies up to z=3. Recently, with the detailed RM images from Very Large Array observations, Govoni et al. (2006) obtained the radial profile of magnetic fields of Abell 2255 and found that the magnetic field strength decreases from the cluster center outward, with an average field strength ~ 1.2 μG over central 1 Mpc^3. Guidetti et al. (2008) also found a similar distribution of magnetic fields in Abell 2382 with an average field strength ~ 1 μG over central 1 Mpc^3.

Other observed phenomena also provide evidence for existence of μG level magnetic fields in galaxy clusters. Sharp discontinuities in X-ray surface brightness are observed in some recently merged clusters. These discontinuities, which are not shocks since no pressure jump is observed, are called cold fronts. Magnetic fields may play a big part in forming such structures by suppressing both the thermal conduction and the Kelvin-Helmholtz instability along the contact discontinuity. Vikhlinin et al. (2001a) estimated that the magnetic field strength is between 7 and 16 μG along cold front in Abell 3667, implying that the undisturbed cluster magnetic fields are between 1 and 10 μG (Vikhlinin et al., 2001b).

Cosmic rays with energies $> 10^{20}$ ev, which lose energy due to photo-pion production through interaction with the CMB (Greisen, 1966; Zatsepin & Kuz'min, 1966), can't propagate more than 50 Mpc. This is called the GZK limit. GZK paradox is the lack of observed correlation between the direction of high energy cosmic rays and nearby AGNs, the most likely source of cosmic rays, at distances less than 50 Mpc (Elbert & Sommers, 1995). One explanation is that the high energy particles are isotropized in the IGM by magnetic fields. Farrar & Piran (2000) estimated that magnetic fields in the local cluster is larger than 0.3 μG by this method.

Direct and indirect observations comfirm the existence of magnetic fields in galaxy clusters. It is still hard to measure the field strength accurately given the limitation of observational techniques, limited numbers of sources, and our incomplete knowledge of the cluster environment. But all methods show that ICM contains μG level fields, with an order of magnitude scatter. Radio halos and relics indicate that magnetic fields are widespread throughout the cluster. Rotation measures tell us that magnetic fields have both hundred kpc and ten kpc scale structures. Power spectra obtained from RM maps also suggest that cluster magnetic fields are in a turbulent state.

1.1.2 Roles of Magnetic Fields in Galaxy Clusters

It is believed that magnetic fields have not played an important role in the formation of galaxies and clusters (Widrow, 2002), which is dominated by dark matter dynamics. For μG fields, the magnetic energy in a cluster is just a few percent of the kinetic energy at large scale, so the magnetic fields are not dynamically important, and just follow the baryons passively. But at smaller scales, magnetic fields can still have some impacts on the evolution of clusters and may play a supporting role by changing heat conduction, providing additional pressure support and helping to produce high energy cosmic rays. And since strong magnetic fields (tens μG) are observed in the early systems (Wolfe et al., 2008; Bernet et al., 2008), the effects of magnetic fields on cluster formation may be even bigger than previously expected.

But magnetic fields may become very important in some interesting phenomena. Understanding cluster magnetic fields is important to understand the cool cores in some clusters. In those clusters, the cooling time of radiative energy loss in the core region is much smaller than the Hubble time, so a large amount of gas should drop out of the hot plasmas. But observations (Tamura et al., 2001; Peterson et al., 2003) do not find spectral signatures of cooling plasma at those cluster centers, so those cluster cores must be heated in some ways. Supernova and AGN feedbacks are two possible heating sources, but they are not estimated to contribute enough energy to stop overcooling (Voit, 2005). Another way to heat cluster cores is thermal conduction from outer regions of clusters. Magnetic fields are crucial in such processes and make the situation very complicated. If the heat conductivity of the ICM is at Spitzer's value of non-magnetized plasma (Spitzer, 1962), thermal conduction will efficiently heat the core gas. But this solution has a difficulty, in that if magnetic fields are present, the thermal conduction will be severely suppressed perpendicular to the magnetic field lines. On the other hand, further research (Narayan & Medvedev, 2001) also suggests that the thermal conduction may be large enough as long as the magnetic fields are tangled. Further study is needed to understand the impact of cluster magnetic fields on the ICM thermal conductivity.

Magnetic fields may also help to answer the question of why only some clusters have cool cores. In recent cluster formation simulations with most up to date cosmology parameters (Spergel et al., 2007), all simulated clusters have a cool core, which contradicts observations that cool cores are only found in some clusters. One explanation is that current simulations don't implement supernova and AGN feedbacks and thermal conduction properly. On the other hand, magnetic fields may also contribute to the resolution of this issue by providing additional pressure support. The magnetic pressure, though small, in cluster centers can help to slow the accretion of cold gas, lowering the gas density, and then, in turn, decreasing the radiative energy loss significantly, since the radiative loss is proportional to the density squared.

Magnetic fields are associated with energetic events, like AGNs, in galaxy clusters.

An AGN outburst may inject up to $\sim 10^{62}$ ergs of energy into the ICM. Large scale radio jets from AGNs suggest that they carry significant magnetic energy (Croston et al., 2005; McNamara & Nulsen, 2007). Giant X-ray cavities observed by Chandra high-resolution X-ray observations(Nulsen et al., 2005; McNamara et al., 2005) hint that magnetic fields may be dynamically important to the ambient regions of the AGNs. By studying 64 X-ray cavities in 32 clusters, Diehl et al. (2008) show that a balance between the magnetic pressure and the thermal pressure of ambient plasmas decides the sizes of bubbles generated by AGNs. This comfirms that magnetic fields should be a major component of AGN ejections, and the properties of the magnetic fields change the cluster evolution near AGNs significantly, at least for the lifetime of the jet/lobe. The interaction of magnetic fields and ICM plasmas may decide the input energy distribution and evolution. Magnetic energy injected from AGN and the formation of magnetic bubbles will be discussed in Chapter 4.

1.1.3 Origins of Cluster Magnetic Fields

The origin of galactic and extragalactic magnetic fields is one of the most interesting and difficult problems in astrophysics. The large Spitzer conductivity of the ICM, $\sim 3 \times 10^{18}$ sec^{-1}, makes the diffusion time scale of the magnetic fields much longer than the Hubble time. Once the magnetic fields are established in the ICM at any time during their formation, the fields will remain to the present epoch unless an anomalous resistive process, like reconnection, occurs (Carilli & Taylor, 2002). It is still unclear what is the effect of turbulence in magnetized medium on the magnetic diffusion.

The almost infinite lifetime of magnetic fields in ICM makes many origins possible. They may be separated into two groups: pre-recombination and post-recombination, where recombination is the era in the Big Bang when the universe has cooled to a temperature, so electrons and ions combined to form neutrals.

Assuming magnetic fields are frozen into the plasma and no other amplification takes place except compression, it requires that magnetic field strengths of about 10^{-8} G at recombination to have the present strength observed in clusters. Observations of the CMB provide a strong upper limit of $B \leq 3 \times 10^{-8}$ G (scaled to the present epoch or ~10^{-2} G at recombination) for large-scale (megaparsec) coherent magnetic fields at the time of recombination (Jedamzik et al., 2000). This limit can't rule out the possibility that current magnetic fields are from the early universe.

There are several mechanisms to generated magnetic fields before recombination, including hydrodynamical Biermann Battery effect (Biermann, 1950), battery effect during the quark-hadron phase transition (Quashnock et al., 1989), dynamo during the electro-weak phase transition (Baym et al., 1996), and inflation field production (Turner & Widrow, 1988). Whether these mechanisms can generate the current level fields is still controversial, and whether the magnetic fields can survive during the radiation era on relevant scales is also debated (Battaner & Lesch, 2000). Magnetic fields from early universe is out of the scope of my thesis research and will not be further discussed. More about magnetic fields in early universe can be found in the review by Grasso & Rubinstein (2001).

Models for generation of ICM magnetic fields post-recombination suggest magnetic fields are injected from normal or active galaxies (De Young, 1992; Kronberg, 1996), and/or are generated by turbulent dynamo and/or shocks occurring during structure formation (Zweibel, 1988; Kulsrud et al., 1997; Ryu et al., 2008).

Rephaeli (1988) and De Young (1992) show that magnetic fields from galaxy outflow may not be solely responsible for μG cluster magnetic fields without some dynamo effects. Their argument is that the mean density ratio of the ICM to the ISM is about 0.01, so "frozen-in" magnetic fields without further amplification in the ICM are smaller than ISM fields by $0.01^{2/3} \sim 0.05$, corresponding to 0.2 to 0.5 μG cluster fields, which is too low by a factor of ten. Donnert et al. (2009) study the cluster magnetic fields from outflow of galactic fields using Smooth Particle Hydrodynamic (SPH) MHD simulations with a simple galactic wind model. They find magnetic fields of a few μG at the cluster centers, but how much the magnetic field are then amplified by ICM motions is unclear.

It was suggested that the large scale fields in the IGM are amplified and maintained by galactic dynamo (Kulsrud & Anderson, 1992; Kulsrud et al., 1997) from small seed fields generated by battery effect or from the early-universe (Widrow, 2002). But recent observations found that large magnetic fields ($\sim \mu G$) are already present at high redshift (up to z=3) (Kronberg et al., 2008). Then, the time for dynamo mechanism to build up magnetic fields is cut short dramatically to only one third(Bernet et al., 2008).

Outbursts of AGNs can inject large amounts of magnetic flux into the ICM, as mentioned at the previous subsection. The ultimate origin of these AGN fields may be the seed fields rapidly amplified by α-Ω dynamo in the accretion disk rotating around the supermassive blackhole (Colgate et al., 2001). From the view of magnetic energy, Kronberg et al. (2001) point out that about ten powerful AGN outbursts may be enough to magnetize the cluster to μG level. A Numerical study on how the magnetic fields from AGN evolve in the ICM is presented in Chapter 5.

There are several plausible ways to generate cluster magnetic fields, including field amplification by cluster mergers and/or turbulence and field injection by active or normal galaxies at high redshift. It is possible that the observed micro Gauss magnetic fields in the ICM come from a combination of all these methods. Improvements in the observations of high-redshift galaxies and clusters, such as the completion of the Expanded Very Large Array, as well as more sophisticated simulations will allow us to better understand these mechanisms and their contributions to cluster magnetic fields.

1.2 Cosmological Simulations with Magnetic Fields

1.2.1 Introduction to Astrophysics Simulations

Computational astrophysics has a long history. After World War II, electronic digital computers, which were introduced during the war to break encryption codes, compute artillery range tables and develop nuclear weapons, were adopted to astrophysics. The earliest applications included computing the first stellar structure models, and the development of numerical methods for fluid flow and shock-capturing in the 1950s (Stone, 2007).

With the increase of computational ability and the progress in numerical algorithms, simulations played a more and more important role in astrophysics research. Numerical methods contribute to and refine theoretical models, constrain cosmology parameters, and extract information from observations. In the 1980s, computational hydrodynamics made great progress in studying astrophysical jets (Norman et al., 1988). N-body simulations were successfully used to determine the profiles of dark matter halos (Navarro et al., 1996) during 1990s. At the same time, Evrard (1990) start to use hydrodynamic simulations to study the physics of X-ray cluster formation. In this decade, adaptive mesh refinement (AMR) and smooth particle hydrodynamics (SPH) simulations played a major role in understanding the first generation of stars(Abel et al., 2002; Yoshida et al., 2003).

Numerical simulation is very important to test models when there are limited or even no observations available. The properties of Population III stars are very interesting by themselves and also very important to the further evolution of the universe. These objects and their direct evolution still can not be observed directly. The range of physics involved in their formation, including dark matter dynamics, gas fluid dynamics, chemical reaction, radiative cooling, the feedback of radiation and metals, makes the pure analytically detailed study impossible. This leaves the numerical simulation the only plausible way to conduct a detailed study of Population III stars. In the last 10 years, significant advancement has been made in the simulations of formation of first generation of stars and has contributed a lot to cosmology cosmology (Abel et al., 2002; O'Shea & Norman, 2007).

The complexity of magnetic field evolution makes numerical simulation a major tool to study magnetic fields in astrophysical problems. Some very successful examples in this field include studying the magnetorotational instability (MRI) in accretion disks (Hawley & Balbus, 1992, and many references thereafter), battery effect during structure formation (Kulsrud et al., 1997), and magnetic field evolution during cluster mergers (Roettiger et al., 1999).

1.2.2 AMR and Cosmological Structure Formation Simulations

With the rapid development of computer hardware, especially distributed memory parallel supercomputers, and software, astrophysicists can perform larger and larger simulations. But simulating cosmological structure formation is still impos-

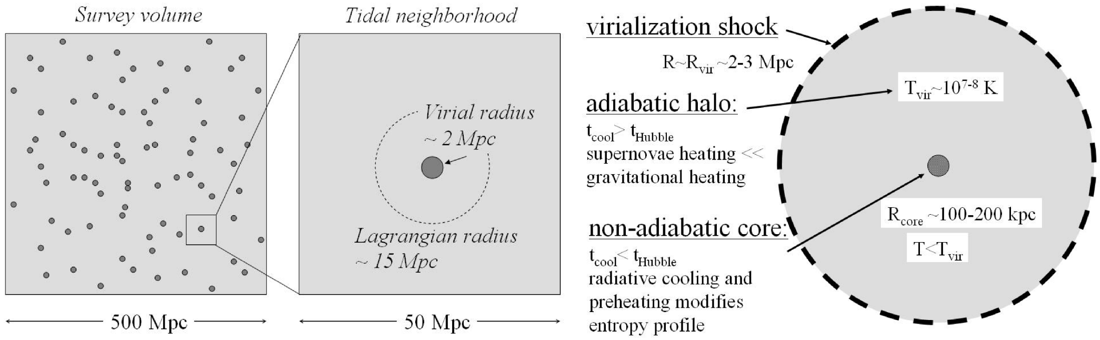

Figure 1.1: Left: Survey volume for capture statistic properties and the virial radius of a massive cluster. Right: Simplified structure of the ICM. Figure courtesy of Michael Norman, initially appeared in Norman (2005).

sible using traditional numerical methods, because it covers a very large dynamic range. Figure 1.1 illustrates the dynamic ranges involved in the simulation of formation of galaxy clusters. The physics of the galaxy cluster core region with a scale of ~ 10 kpc will be greatly influenced by the tidal effects at (100 Mpc)^3 during the cluster formation. The required spatial dynamic range for this problem is about 10000, which is much outside the computational capability of the most powerful supercomputer today and even in a near future if computed on a regular 3-Dimensional 10000^3 grid. Larger survey volumes ($\sim$500 Mpc) needed to study statistical properties of clusters makes the simulations even harder.

AMR codes have made the detailed simulations of large scale structure formation with hydrodynamics become possible since the late 1990s. AMR increases the spatial and temporal resolutions automatically only in the collapsing regions which occupy only a fraction of the total volume, so a huge amount of computer time and memory are saved while a large dynamic range is obtained. For example, an AMR simulation of 128^3 root grid with 8 level refinements can study cluster formation in a survey volume of about 350 Mpc on a side at a resolution of $\sim$10 kpc in the cluster core region using just a few hundred CPU hours with tens of computing cores. A few examples of applications of AMR simulations include formation of first generation stars (Abel et al., 2002; O'Shea & Norman, 2007), formation of galaxies clusters (Bryan & Norman, 1998), and turbulence in molecular cloud (Kritsuk et al., 2006).

Great successes have been achieved in all these applications.

1.2.3 Cosmological MHD Simulations

The absence of the ability to include magnetic fields in AMR simulations limits studying the role of magnetic fields in the large scale structure formation. The previous Eulerian MHD simulations are usually performed on a unifrom grid with a small dynamic range and for a short simulation time. Kulsrud et al. (1997) studied the Biermann Battery effect in cosmological structure formation and obtained interesting results. But the resolution in their simulations is as large as scale of interest, neglecting larger scale tidal forces. The magnetic field evolution of galaxy cluster formation was studied by Dolag et al. (1999, 2002) by SPH MHD codes with some success, though SPH code is not very good for studying either MHD (Widrow, 2002) or turbulence problems (Li & Liu, 2004).

Adding magnetic fields to an AMR code is an important extension of this powerful simulation tool, but it is also very complicated and challenging. MHD equations not only add additional complexity to the PDE solver relative to purely hydrodynamical solvers, but also require that the divergence of magnetic fields must be kept to zero during simulations. So interpolating and reconstructing magnetic fields correctly on the AMR hierarchy become very important. It is also very difficult and complicated in programming. This will be discussed in great detail in the next chapter. In this dissertation, we present the newly developed MHD version of the AMR cosmology code Enzo and the applications of this code to the evolution of magnetic fields in galaxy clusters.

1.3 Structure of the Dissertation

This dissertation is organized as follows. In the next chapter, we describe the code used in this research, EnzoMHD. In chapter 3, we present the results of studying the creation of magnetic fields from the Biermann Battery effect. It includes two parts. The first is Population III star formation, where we find that 10^{-9} G fields are formed at the core of the star forming halo. This is the minimum initial field in the first generation of stars. This field may be the seed field for the later dynamo processes. The second is battery effect during galaxy cluster formation. In this study, the final magnetic fields in the cluster is about 10^{-18} G. This indicates that the battery effect alone is too weak to be the origin of cluster magnetic fields at large scale. Chapter 4 discusses how X-ray cavities in galaxy clusters could be produced by the magnetic fields injected from their central AGNs. It indicates that magnetic fields from a super massive black hole may be large and dynamically important. Chapter 5 further studies the evolution of magnetic field from AGN at high redshift. It shows that the local magnetic fields from AGN, after numerous mergers and continuous stretching and shocking, can become cluster wide, μG level fields similar to the observations.

Chapter 2

Cosmology AMR MHD code – EnzoMHD

2.1 Introduction

Enzo is an adaptive mesh refinement (AMR), grid-based hybrid code (hydro + N-Body) which is designed to do simulations of cosmological structure formation. It uses the block-structured AMR algorithm of Berger & Colella (1989) to improve spatial resolution where required, such as in gravitationally collapsing objects. The method is attractive for cosmological applications because it: 1) is spatially- and time-adaptive, 2) uses accurate and well-tested grid-based methods for solving the hydrodynamics equations and 3) can be well optimized and parallelized. The central idea behind AMR is to solve the evolution equations on a fixed resolution grid, adding finer grids in regions that require enhanced resolution. Mesh refinement can be continued to an arbitrary level, based on criteria involving any combination of (dark-matter and/or baryon) over density, Jeans length, cooling time, etc, enabling users to tailor the adaptivity to the problem of interest. Enzo solves the following physics models: collisionless dark-matter and star particles, using the particle-mesh N-body technique (Hockney & Eastwood, 1985); gravity, using FFTs on the root grid and multigrid relaxation on the subgrids; cosmic expansion; gas dynamics, using the piecewise parabolic method (PPM) (Colella & Woodward, 1984) as extended to cosmology by Bryan et al. (1995); multi-species non-equilibrium ionization and H_2

chemistry, using backward Euler time differencing (Anninos et al., 1997); radiative heating and cooling, using subcycled forward Euler time differencing (Anninos & Norman, 1994); and a parameterized star formation/feedback recipe (Cen & Ostriker, 1993). Enzo has been successfully used in many cosmological applications, including star formation (Abel et al., 2000, 2002; O'Shea et al., 2005; O'Shea & Norman, 2007), Lyman-alpha forest (Bryan et al., 1999; Jena et al., 2005), interstellar medium (Kritsuk & Norman, 2002, 2004) and galaxy clusters (Bryan & Norman, 1998; Loken et al., 2002; Motl et al., 2004; Hallman et al., 2006). More information about Enzo is available at http://lca.ucsd.edu/projects/enzo

One important piece of physics that is missing from this list is a proper treatment of magnetic fields. Magnetic fields have a broad range of impacts in a broad range of physical situations, from galaxy clusters to protostellar core formation. Magnetic forces can shape morphology of objects by forcing flow along the field lines. They can alter the energy balance by providing sources of pressure and energy. They can alter cooling rates by trapping electrons. Alfven waves can redistribute angular momentum throughout an object. They create X-ray cavities seen in some galaxy clusters. They accelerate cosmic rays, which play a crucial role in the energy balance of the galaxy and galaxy clusters. They also play a role in galactic star formation, potentially removing angular momentum from collapsing objects and launching protostellar winds. Creating a functional cosmological MHD code takes more than a single algorithm. The purpose of this chapter is to present the construction and performance of the algorithms that will be used in MHD simulations with Enzo in this thesis and in the future, as well as simulations that have already been done (Xu et al., 2008a,b)

EnzoMHD is also a purpose code. In this chapter, we will discuss it as a cosmological code, but all the same machinery applies in non-cosmological mode. All algorithms used here reduce to the non-cosmological limit by setting $a \rightarrow 1, \dot{a} \rightarrow 0$, and $\ddot{a} \rightarrow 0$. This removes any frame dependent terms in the equations.

We will describe the numerical procedures in Section 2.2, present test problems in Section 2.3, and present conclusions and future plans in Section 2.4. Some complex numerical scheme and procedures are presented in the Appendix at the end of this dissertation. In Appendix A.3 We present a simplified schematic to unify the pieces of the solver, and in Appendix A.1 and A.2 we expand on some of the more complex numerical procedures about AMR MHD Reconstruction and Flux Correction.

2.2 Numeric

2.2.1 Cosmological MHD Equations

EnzoMHD solves the MHD equations in a comoving coordinate frame.

$$\frac{\partial \rho}{\partial t} + \frac{1}{a}\nabla \cdot (\rho \mathbf{v}) = 0 \tag{2.1}$$

$$\frac{\partial \rho \mathbf{v}}{\partial t} + \frac{1}{a}\nabla \cdot (\rho \mathbf{v}\mathbf{v} + \bar{p} - \mathbf{B}\mathbf{B}) = -\frac{\dot{a}}{a}\rho \mathbf{v} - \frac{1}{a}\rho \nabla \Phi \tag{2.2}$$

$$\frac{\partial E}{\partial t} + \frac{1}{a}\nabla \cdot [\mathbf{v}(\bar{p} + E) - \mathbf{B}(\mathbf{B}\cdot \mathbf{v})] = -\frac{\dot{a}}{a}(\rho v^2 + \frac{2}{\gamma - 1}p + \frac{B^2}{2}) - \frac{\rho}{a}\mathbf{v}\cdot \nabla \Phi \tag{2.3}$$

$$\frac{\partial \mathbf{B}}{\partial t} - \frac{1}{a}\nabla \times (\mathbf{v} \times \mathbf{B}) = -\frac{\dot{a}}{2a}\mathbf{B} \tag{2.4}$$

with the equation of state

$$E = \frac{1}{2}\rho v^2 + \frac{p}{\gamma - 1} + \frac{1}{2}B^2 \tag{2.5}$$

$$\bar{p} = p + \frac{1}{2}B^2 \tag{2.6}$$

Here, ρ is the comoving density, p is the comoving gas pressure, v is the proper peculiar velocity, $\mathbf{B}$ is the comoving magnetic field, E is the total peculiar energy per unit comoving volume, $\bar{p}$ is the total comoving pressure, γ is the ratio of the specific heats, Φ is the modified gravitational potential from both dark-matter and baryons, $a \equiv (1+z_i)/(1+z)$ is the expansion factor, where z_i and z are the initial and current redshifts, respectively, and t is the time.

In this formulation, the comoving quantities that are evolved by the solver are related to the proper observable quantities by the following equations:

$$\rho_{proper} = \rho_{comoving} * a^{-3} \tag{2.7}$$
$$p_{proper} = p_{comoving} * a^{-3} \tag{2.8}$$
$$\mathbf{v}_{proper} = \mathbf{v}_{peculiar} + \dot{a}\mathbf{x} \tag{2.9}$$
$$\Phi_{proper} = \Phi_{modified} - \frac{1}{2}a\ddot{a}\mathbf{x}^2 \tag{2.10}$$
$$\mathbf{B}_{proper} = \mathbf{B}_{comoving} * a^{-\frac{3}{2}} \tag{2.11}$$

where $\mathbf{x}$ is the comoving position, which is defined as $\mathbf{x} \equiv \mathbf{r}/a$.

The definition of comoving magnetic fields is to keep the equations as simple as possible. Due to the additional expansion factor that we use in equation 2.4, the proper magnetic field decreases proportional to a^{-2} as in all formulations of the cosmological MHD equations.

For non-cosmological simulations, the same equations hold, but with with $a = 1, \dot{a} = 0$ and $\ddot{a} = 0$. This effectively removed each appearance of a from the left hand side, and eliminates the terms involving $\dot{a}$ from the right. For ease of reference, these are:

$$\frac{\partial \rho}{\partial t} + \nabla \cdot (\rho \mathbf{v}) = 0 \tag{2.12}$$
$$\frac{\partial \rho \mathbf{v}}{\partial t} + \nabla \cdot (\rho \mathbf{v}\mathbf{v} + \bar{p} - \mathbf{B}\mathbf{B}) = -\rho \nabla \Phi \tag{2.13}$$
$$\frac{\partial E}{\partial t} + \nabla \cdot [\mathbf{v}(\bar{p} + E) - \mathbf{B}(\mathbf{B} \cdot \mathbf{v})] = -\mathbf{v} \cdot \nabla \Phi \tag{2.14}$$
$$\frac{\partial \mathbf{B}}{\partial t} - \nabla \times (\mathbf{v} \times \mathbf{B}) = 0 \tag{2.15}$$

with the same equation of state, equations 2.5 and 2.6. Here, ρ is the density, p is the gas pressure, v is the velocity, $\mathbf{B}$ is the magnetic field, E is the total energy per unit volume, $\bar{p}$ is the total gas pressure, γ is the ratio of the specific heats, Φ is the gravitational potential. The mechanism to switch between the two systems of equations will be described in Section 2.2.6.

To solve these equations, we operator split eqns (2.1)-(2.4) into four parts: the left hand side of equations (2.1)-(2.3), the left hand side of equation (2.4), the gravitational acceleration (the two terms involving $\nabla\Phi$), and the expansion terms (the two terms involving $\dot{a}$). These will be discussed in Sections 2.2.6 - 2.2.7. In Section 2.2.10, we will discuss the dual energy formulation in Enzo for hypersonic flows, and in Section 2.2.11 we will discuss the Adaptive Mesh Refinement algorithm. We first discuss the data structures used to carry all this data in Section 2.2.2

In the following, we will often have cause to separate the purely fluid dynamical quantities $\rho, \vec{v}, E$ from the magnetic field $\vec{B}$. Unless otherwise noted, 'fluid quantities' will refer to the former only.

For ease of reference, we have supplied a schematic summary of the steps involved in Appendix A.3.

2.2.2 Data Structure

In Enzo, both parallelism and AMR are done in block decomposed manner. Each patch of space, called a `grid`, is treated as a unique computational problem with Dirichlet boundary conditions which are stored in a number of Ghost Zones (see section 2.2.5). The number of ghost zones depends on the method used. The pure-hydro methods in Enzo, ZEUS and PPM, use 3 ghost zones. The method we describe here uses 5 ghost zones.

Grids are arranged in a strictly nested hierarchy, with each grid having a cell width half that of its parent (pure hydro Enzo can take any integer refinement, but the interpolation for MHD is restricted to factors of 2.). See Figure 2.1. Each processor keeps a copy of the entire hierarchy, while only one of the processors actual stores the data.

For all physics modules described in this chapter, an individual grid cares not for where it sits in space or the hierarchy, and communicates with other grids only through boundary condition fills (Section 2.2.5) and the AMR cycle (Section 2.2.11).

EnzoMHD in its default mode tracks 14 fields, stored at 3 different points of the cell. The 5 hydrodynamic quantities, $\rho, \mathbf{v}, E_{total}$ are stored at the center of the cell, denoted (i, j, k), and represent the volume average of the respective quantities. These are the same quantities stored in non-MHD Enzo.

EnzoMHD tracks 2 copies of the magnetic field and the electric field. One copy of the magnetic field is stored in the face of the cell perpendicular to that field

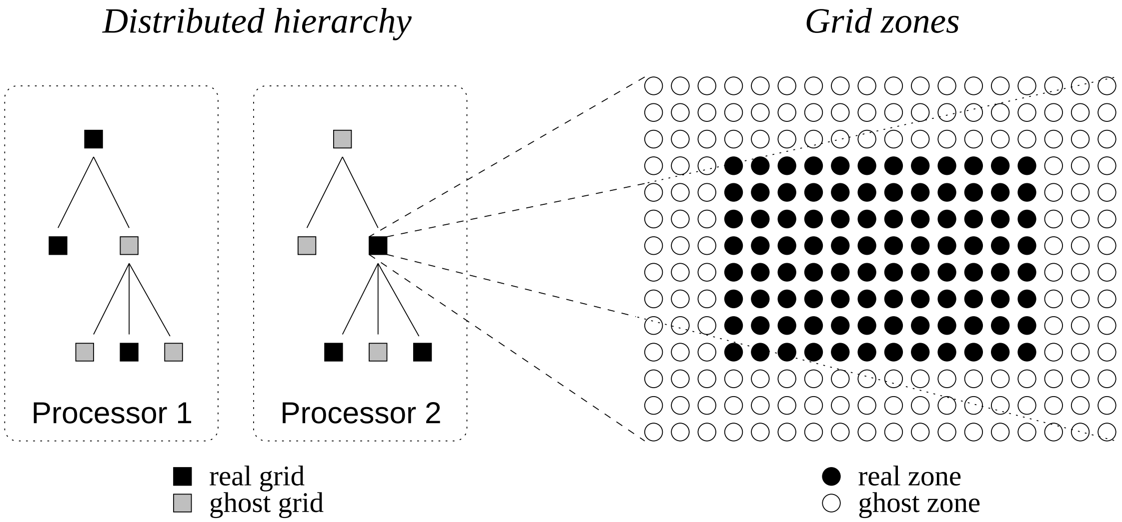

Figure 2.1: A schematic of a parallel AMR hierarchy on two processors (left) and a grid patch with ghost zones (right). Image courtesy James Bordner, initially appeared in (Norman et al., 2007).

component, and represents the area average of that field component over that face. This is the primary representation of the magnetic field. So $B_{f,x}$ is stored in the center of the x face, denoted $(i-\frac{1}{2},j,k)$, $B_{f,y}$ in the y face at $(i,j-\frac{1}{2},k)$, and $B_{f,z}$ in the z face at $(i,j,k-\frac{1}{2})$. It is this field that remains divergence free under the cell centered divergence operator:

$$\begin{aligned}\nabla\cdot\mathbf{B_f} =& \frac{1}{\Delta x}(B_{f,x,i+\frac{1}{2},j,k}-B_{f,x,i-\frac{1}{2},j,k})+\\ &\frac{1}{\Delta y}(B_{f,y,i,j+\frac{1}{2},k}-B_{f,y,i,j-\frac{1}{2},k})+\\ &\frac{1}{\Delta z}(B_{f,z,i,j,k+\frac{1}{2}}-B_{f,z,i,j,k-\frac{1}{2}})\end{aligned} \tag{2.16}$$

The magnetic data structures are one element longer in each longitudinal direction, so for an $nx\times ny\times nz$ grid patch, the $B_{f,x}$ structure is $(nx+1)\times ny\times nz$.

The second representation of the magnetic field is centered with the fluid quantities at the center of the cell. This field is used wherever a cell centered magnetic quantity is needed, most notably in the hyperbolic solver in section 2.2.6. It's equal to the first order average of the face centered magnetic field:

$$\begin{aligned}
B^{n+1}_{c,x,i,j,k} &= 0.5 * (B_{f,x,i+\frac{1}{2},j,k} + B_{f,x,i-\frac{1}{2},j,k}) \\
B^{n+1}_{c,y,i,j,k} &= 0.5 * (B_{f,y,i,j+\frac{1}{2},k} + B_{f,y,i,j-\frac{1}{2},k}) \\
B^{n+1}_{c,z,i,j,k} &= 0.5 * (B_{f,z,i,j,k+\frac{1}{2}} + B_{f,z,i,j,k-\frac{1}{2}})
\end{aligned} \tag{2.17}$$

The final data structure used in EnzoMHD is the Electric Field, which is stored along the edges of the computational cell. This represents a linear average of the electric field along that line element. Each component is centered along the edge its parallel to, so E_x lies along the x edge of the cell at $(i, j - \frac{1}{2}, k - \frac{1}{2})$, etc. It is longer than the fluid fields by one in each transverse direction, so E_x would be $nx \times (ny + 1) \times (nz + 1)$.

Each grid also stores one copy of each of the above mentioned fields for use in assigning ghost zones to subgrids. This is described further in Section 2.2.5. A temporary field for fluxes is also stored, which exists only while the hyperbolic terms are being updated. This data structure is also stored on the faces of the zone. There are three fluxes for all 7 MHD quantities.

For other configurations of EnzoMHD, more or fewer fields may be used. In purely isothermal mode (which is at present an option only in EnzoMHD, not in Enzo) the total energy field is not tracked, and the isothermal sound speed is taken as a global scalar quantity. This reduces the number of fields tracked everywhere the total energy shows up. With dual energy formalism on (see Section 2.2.10) an additional field corresponding to either gas energy or entropy is stored, giving an additional field where needed. Future work will include multi-species chemistry and more complex cooling, which will include additional fields for each species.

2.2.3 Consistency

In several places throughout the flow of Enzo, there may be more than one data structure using and writing to a given variable at a given point in space. Ghost zones and face centered fields (fluxes and magnetic fields) are examples of this. In EnzoMHD, it is imperative that all data at a given point is identical, regardless of the data structure describing it. This may seem like an unnecessary comment, but it isn't;

in pure hydro simulations, numerical viscosity will damp out small perturbations caused by slight inconsistencies in data description. Thus in practice, especially in large, stochastic simulations, errors can go unnoticed. Often these discrepancies are negligible, other times not, especially when one is concerned with the conservation of a particular variable, like $\nabla \cdot \mathbf{B}$. By construction EnzoMHD preserves $\nabla \cdot \mathbf{B}$ to machine precision, but it never *forces* $\nabla \cdot \mathbf{B} = 0$; so if it's not zero at the beginning of a time step, it's not going to be at the end, either. It is also worth mentioning that inconsistencies in any quantity will cause inconsistencies in the flow, which will in turn cause $\nabla \cdot \mathbf{B}$ issues. Thus any improper handling of *any* fluid quantity will cause errors in $\nabla \cdot \mathbf{B}$ that will persist and usually grow to catastrophic proportions in a relatively short period of time.

There is a prominent redundancy in the magnetic field, namely the field on the surface of the active zones of grids. See Figure 2.2. Care is taken to include enough ghost zones, and frequent enough ghost zone exchange between grids, that after a time step, two neighboring grids have reached exactly the same answer on the surface between the two grids completely independently.

2.2.4 Time Stepping

Enzo uses hierarchical time stepping to determine it's time step. The minimum of 4 different criteria is taken for each level, which will be described below in detail. Timesteps are taken in order of coarsest to finest, in a 'W' cycle. See Figure 2.3. Given 3 levels, level 0 takes the first step of Δt. Then level 1 takes a single step of $\Delta t/2$. Then level 2 takes one step of $\Delta t/4$. Then, given that there are only three levels, it takes another timestep so it is temporally in line with the level above. The last three steps repeat: level 1 then takes its second and final step of $\Delta t/2$ so it is now at the same time as level 0, followed by two steps on level 2.

In principle, if a given level has a cell size Δx and the next level of refinement has cell size $\frac{\Delta x}{r}$, where r is the refinement factor, the more refined grid will have, in principle, time step size $\frac{\Delta t}{r}$. In Enzo, the step size is chosen for each level and each subgrid time step. In practice, owing to more finely resolved structures having slightly higher fast shock speeds, fine grids may in fact take more than r time steps

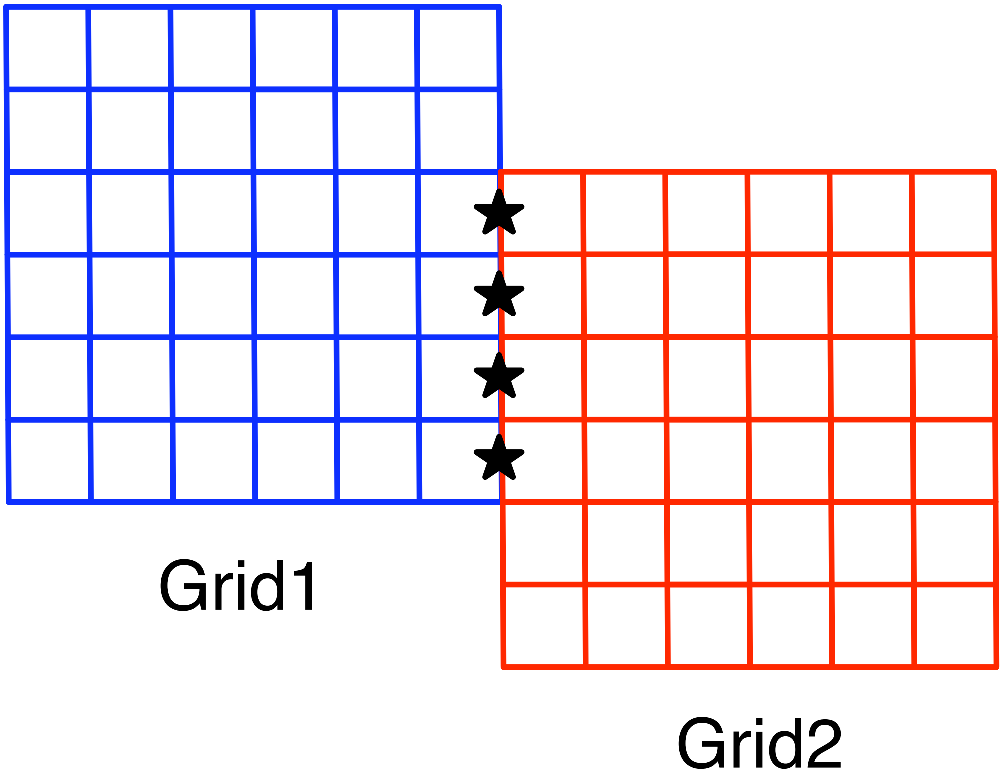

Figure 2.2: Data redundancy of the face centered magnetic fields: the face centered field denoted by the stars are updated by both grid 1 and grid 2. Enough ghost zones are exchanged to ensure that the entire stencil for the update of these fields is the same in both data structures.

for each parent grid step. In some rare cases, such as cosmological expansion limiting, a finer grid may take less than r steps.

MHD

For the MHD part, the harmonic mean of the 3 Courant conditions is used. This was demonstrated to be the most robust time stepping criterion possible for multi dimensional flows by Godunov et al. (1961).

$$\begin{aligned}\Delta t_{hydro} =& \frac{1}{1/t_x + 1/t_y + 1/t_z} \\ t_x =& min(\frac{\Delta x}{c_{f,x}}) \\ t_y =& min(\frac{\Delta y}{c_{f,y}}) \\ t_z =& min(\frac{\Delta z}{c_{f,z}})\end{aligned} \tag{2.18}$$

where the min is taken over the zones on a level, and $c_{f,x}, c_{f,y}$ and $c_{f,z}$ are the fast MHD shock speeds along each axis:

$$c_{f,x}^2 = \frac{1}{2}\left({c_s}^2 + \frac{\mathbf{B}\cdot\mathbf{B}}{\rho} + \sqrt{({c_s}^2 + \frac{\mathbf{B}\cdot\mathbf{B}}{\rho})^2 - 4{c_s}^2 B_x^2/\rho} \right) \tag{2.19}$$

and similar definition for the other two. Here c_s is sound speed.

Gravitational acceleration

The time step is also restricted to be less than the time it takes for the gravitational acceleration g alone to move a parcel of fluid half of one zone.

$$\Delta t_{accel} = min(\frac{1}{2}\sqrt{\frac{\Delta x}{g_i}}) \tag{2.20}$$

where $i = x, y, z$ and the min is taken of the zones on a level.

Cosmological expansion

An additional restriction comes from the cosmological expansion, requiring the timestep to be less than the cosmological expansion timescale,

$$\Delta t_{expansion} = \eta \frac{a}{\dot{a}} \tag{2.21}$$

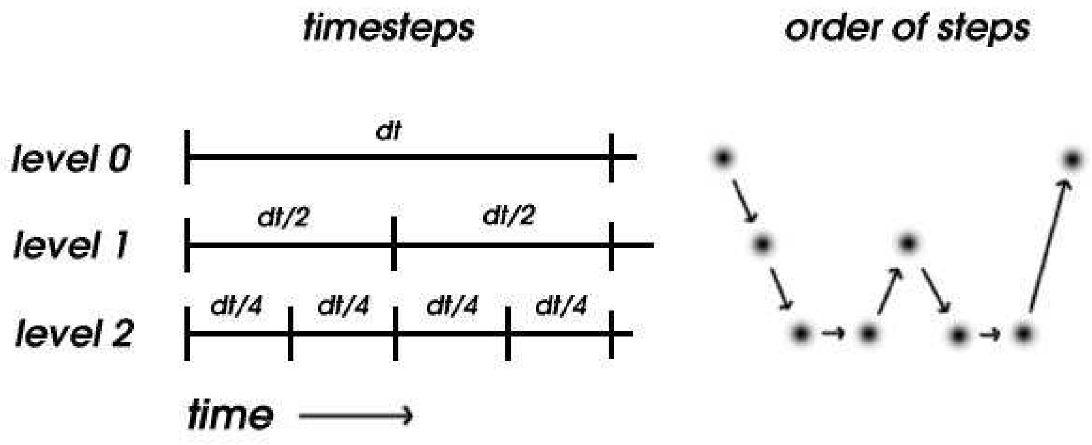

Figure 2.3: A depiction of the timestep strategy in Enzo.

where η is typically 0.01.

Particle motion

The fourth timestep criterion is based on restricting particle displacement in a single timestep to be smaller than a single zone:

$$\Delta t_{particles} = min(\frac{a\Delta x}{v_{i,p}}) \tag{2.22}$$

where min is over velocity component i and particle p.

2.2.5 Boundary Conditions and Ghost Zones

Ghost Zones are filled in one of three means.

1. **Copying.** The dominant mechanism for filling ghost zones copying from active zones that occupy the same physical space. This also takes into account periodic boundary conditions. For EnzoMHD, face centered fields are copied from the faces of all cells, including those that border on active cells. This is somewhat redundant for reasons described in 2.2.3.

2. **External** Root grids that lie along the domain wall filled with the external boundary routine. If the external boundary condition is not periodic, the grids

zones are filled by a predetermined algorithm; for instance, outflow boundary conditions set ghost zones to be equal to the outermost active zone, akin to a Neumann condition of zero slope. These involve outflow, reflecting, and a completely general 'inflow'. Note that this is called only on the root grid, and not on subgrids that happen to lie on the edge. This can cause spurious waves at reflecting or outflow boundaries with AMR. Also note for EnzoMHD, the only external boundary conditions that have been tested are periodic and outflow.

3. **Interpolation** The third mechanism is used on refined grids whose ghost zones do not occupy the active space of another grid; these grids have their ghost zones filled by interpolation from the parent grid. Since Enzo uses hierarchical time stepping, subgrid steps that begin in the middle of a parent grid step fill their ghost zones from a linear interpolation of the parent grid time steps at t^n and t^{n+1}.

2.2.6 Left hand side: hyperbolic terms

With the exception of the $1/a$ term that appears in front of each $\nabla\cdot$ operator, the left hand side of equations (2.1)-(2.4) are the familiar Ideal MHD equations. A form of equations (2.1) - (2.4) more relevant for this treatment is the following:

$$\frac{\partial \mathbf{V}}{\partial t} + \frac{\partial \mathbf{F}}{\partial x} = 0 \tag{2.23}$$

where

$$\mathbf{V} = \begin{pmatrix} \rho \\ \rho v_x \\ \rho v_y \\ \rho v_z \\ B_y \\ B_z \\ E \end{pmatrix} \tag{2.24}$$

$$\mathbf{F} = \begin{pmatrix} \rho v_x \\ \rho v_x^2 + p + B^2/2 - B_x^2 \\ \rho v_x v_y - B_x B_y \\ \rho v_x v_z - B_x B_z \\ B_y v_x - B_x v_y = -E_z \\ B_z v_x - B_x v_z = E_y \\ (E + p + B^2/2) v_x - B_x (\mathbf{B} \cdot \mathbf{v}) \end{pmatrix} \tag{2.25}$$

$$p = (E - \frac{1}{2}\rho\mathbf{v}^2 + \frac{1}{2}\mathbf{B}^2(\gamma - 1)) \tag{2.26}$$

These form a hyperbolic system of equations, which have been studied extensively in the literature. To take advantage of the work already done on this type of system of equations for our cosmological algorithm, we first multiply the cell width dx by the expansion factor a. This allows us to use any non-cosmological solver for cosmological applications. Upon completion of the solver, dx is divided by a to restore dx to the original comoving value.

Equation 2.23 is solved by first re-writing it in conservation form, that is taking suitable integrals in time and space. The resulting update is, in one dimension,

$$\hat{V}^{n+1}_{i,j,k} = \hat{V}^{n}_{i,j,k} - \frac{\Delta t}{\Delta x}(\hat{F}^{n+\frac{1}{2}}_{x,i+\frac{1}{2},j,k} - \hat{F}^{n+\frac{1}{2}}_{x,i-\frac{1}{2},j,k}) \tag{2.27}$$

where $\hat{V}$ represents the spatial average of the conserved quantities, and $\hat{F}$ represents an space and time average of the flux, centered in time at $t = t + \Delta t/2$. $\hat{V}$ is the quantity we store in the cells, and $\hat{F}$ comes from the hyperbolic solver.

The solver we use to solve the hyperbolic equations is that of Li et al. (2008), which is comes in three parts: spatial reconstruction, time centering, and the solution of the Riemann problem. Spatial reconstruction is done using piecewise linear monotonized slopes on the primitive variables $(\rho, \mathbf{v}, p, \mathbf{B})$. Time centering of the interface states by $\Delta t/2$ is performed using either the MUSCL-Hancock (Li et al., 2008) or Piecewise Linear Method (Colella & Glaz, 1985) integration. The Riemann problem is then solved using either the HLLC Riemann solver of Li (2005), HLLD solver of Miyoshi & Kusano (2005), or the isothermal HLLD solver of Mignone (2007) (The isohermal mode will not be further discussed in my thesis). These fluxes are computed for the conserved, cell centered variables $(\rho, \rho\mathbf{v}, E, \mathbf{B_c})$. These fluxes are then differentiated to obtain the update values of the fluid quantities only. The fluxes for the magnetic field are stored for use in the Constrained Transport algorithm, discussed in section 2.2.7. This is done in one dimension on successive sweeps along the x, y, and z directions. To reduce operator splitting error, the order of the sweeps is permuted. For more details, see Li et al. (2008).

2.2.7 Constrained Transport and the Divergence of B

One of the biggest challenges for an MHD code is to maintain the divergence free constraint on the magnetic field ($\nabla \cdot \mathbf{B} = \mathbf{0}$). Brackbill & Barnes (1980) found that non-zero divergence can grow exponentially during the computation and cause the Lorentz force to be non-orthogonal to the magnetic field. There are three major ways to assure the divergence remains zero. The first is a divergence-cleaning (or Hodge Projection) approach by Brackbill & Barnes (1980), which solves an extra Poisson's equation to recover $\nabla \cdot \mathbf{B} = \mathbf{0}$ at each time step. But Balsara & Kim (2004) found that non-locality of the Poisson solver introduces substantial spurious small scale structures in the solution. Additionally, solving Poisson's equation on an AMR mesh is computationally expensive. The second method involves extending the MHD equations to include a divergence wave, as done by Powell et al. (1999), Dedner et al. (2002), which then advects the divergence out of the domain. As most of our solutions are done on periodic domains, this is also an undesirable solution. The third method, and the one we have employed in Enzo, is the constrained transport (CT) method of Evans & Hawley (1988). This method centers the magnetic field on the faces of the computational cells and the electric field on the edges. Once the electric field is computed (more on this later) it's curl is taken to update the magnetic field. This ensures $\nabla \cdot \mathbf{B} = 0$ for all time, provided it's true initially.

$$\begin{aligned}\hat{B}^{n+1}_{f,x,i-\frac{1}{2},j,k} = \hat{B}^{n}_{x,i-\frac{1}{2},j,k} - \Delta t(&\frac{1}{\Delta y}(\hat{E}_{z,i-\frac{1}{2},j+\frac{1}{2},k} - \hat{E}_{z,i-\frac{1}{2},j-\frac{1}{2},k}) + \\ &\frac{1}{\Delta z}(\hat{E}_{y,i-\frac{1}{2},j,k+\frac{1}{2}} - \hat{E}_{y,i-\frac{1}{2},j,k-\frac{1}{2}}))\end{aligned} \quad (2.28)$$

Plugging equation A.24 into the divergence operator 2.16 to find $\nabla \cdot \mathbf{B}^{n+1}_f$, one finds all terms are eliminated except the initial divergence $\nabla \cdot \mathbf{B}^{n}_f$.

The CT algorithm of Evans & Hawley (1988) was extended to work with finite volume methods by Balsara & Spicer (1999). This method uses the fact that the MHD Flux has the electromotive force as two of its components (see the 5^{th} and 6^{th} components of eqn. 2.25), so using these components then incorporates all the higher order and shock capturing properties of the Godunov solver into the evolution of the electric field. These components, which are centered at the face the computational cell, are then averaged to obtain an electric field at the edges of the cell. This was the first CT method applied to Enzo, so unless otherwise noted, the simulations presented here were done with this method. The reader is encouraged to read Balsara & Spicer (1999) for the full details.

Gardiner & Stone (2005) extended this idea to include higher order spatial averaging, which eliminates a number of numerical artifacts present in Balsara & Spicer (1999) and increases the accuracy of the method. This method uses the fluxes from the Riemann solver, plus additional information from the data in the cell to construct a linear interpolation from the cell face to the cell edge. The reader is encouraged to see that paper for the details.

After the curl is taken and the face centered field $\mathbf{B_f}$ is updated, it is then averaged to obtain $\mathbf{B_c}$, via equation 2.17.

2.2.8 Right Hand Side: Gravitational Acceleration

In cosmological simulations, Enzo tracks the proper peculiar gravitational potential.

$$\nabla^2\Phi = \frac{4\pi G}{a}(\rho_b + \rho_d - \rho_0) \tag{2.29}$$

where ρ_b and ρ_d are baryonic and dark matter comoving density respectively, and ρ_0 is the comoving background density. For non-cosmological simulations, the dark matter and background density are ignored.

The gravitational potential Φ is solved in Enzo using a combination of methods. First, the root grid potential (which covers the entire computational domain) is solved for using a fast Fourier transform. Then the subgrids (which hopefully do not cover the computational domain) are solved using a multigrid relaxation technique. This resulting potential Φ is then differentiated to obtain the acceleration $\mathbf{g} = \nabla\Phi$.

Specifically,

$$\mathbf{g}_i = \frac{1}{2}\frac{(\Phi_{i+1} - \Phi_{i-1})}{dx} \tag{2.30}$$

As mentioned before, the fluxes are computed at the half time point $t + 1/2\Delta t$. In order to keep the velocity and consistent with this time centering, they are first advanced by a half time step:

$$\mathbf{v}' = \mathbf{v} + \frac{\Delta t}{2}\mathbf{g} \tag{2.31}$$

After the fluxes are differentiated to obtain the new state v_x^{n+1}, these states are then updated with the accelerations. For the velocity update, a density field centered in time is used. We follow the same formulation used by Colella & Woodward (1984)

$$\begin{aligned} {v_x}^{n+1} &= v_x'^{n+1} + \Delta t \frac{\frac{1}{2}(\rho^{n+1} + \rho^n) g_x}{\rho^{n+1}} && (2.32) \\ E^{n+1} &= E'^{n+1} - \frac{1}{2}\rho^{n+1}({v_x}'^{n+1})^2 + \frac{1}{2}\rho^{n+1}({v_x}^{n+1})^2 && (2.33) \end{aligned}$$

2.2.9 Right Hand Side: Expansion Source Terms

The cosmological expansion source terms are treated in much the same way as the gravitational source terms. First, a half time step is added to the values before the flux is computed.

$$\begin{aligned} \mathbf{v'^n} =& \mathbf{v^n} - \mathbf{\frac{1}{2}\Delta t\frac{\dot{a}}{a}}\rho^{\mathbf{n}} && (2.34) \\ p'^n =& p^n - \frac{1}{2}\Delta t\frac{\dot{a}}{a}3(\gamma - 1)p^n && (2.35) \\ \mathbf{B_c'^n} =& \mathbf{B_c^n} - \mathbf{\frac{1}{2}\Delta t\frac{\dot{a}}{2a}B_c^n} && (2.36) \end{aligned}$$

The quantities $\mathbf{v'^n}$, p'^n and $\mathbf{B'^n}$ are then used in the rest of the solver described in Section 2.2.6. After the fluxes are differentiated, the source terms are then added to the fluid quantities in full. This is done in a semi-implicit manner, by averaging the quantities to be updated in time. For instance, the expansion contribution to the magnetic field is

$$\frac{\partial \mathbf{B}}{\partial t} = -\frac{\dot{a}}{2a}\mathbf{B} \tag{2.37}$$

which is discretized

$$\mathbf{B}_{exp}^{n+1} - \mathbf{B}^{n+1} = -dt\frac{\dot{a}}{2a}(\frac{\mathbf{B}_{exp}^{n+1} + \mathbf{B}^{n+1})}{2}) \tag{2.38}$$

and solving for $\mathbf{B}_{exp}^{n+1}$ we have

$$x = \frac{\dot{a}}{4a} \tag{2.39}$$

$$\mathbf{B}_{exp}^{n+1} = \frac{(1-x)}{(1+x)}\mathbf{B}^{n+1} \tag{2.40}$$

Pressure and velocity are updated in a similar manner. See appendix A.3 for the full update.

2.2.10 Dual Energy Formalism

Hypersonic flows are quite common in cosmological simulations. Due to the extremely large gravitational forces, the ratio of kinetic energy $E_{kinetic}$ to gas internal energy $E_{internal}$ can be as high as 10^8. This leads to problems when computing the internal energy in this type of flow, as the universe does math with infinite accuracy, but computers do not. Higher order Godunov code typically track only the total energy (equation 2.5). Thus finding the internal energy from the total energy tracked by the software,

$$E_{internal} = E_{total} - E_{kinetic} - E_{magnetic}$$

involves the small difference of two (or three) large numbers, which causes problems when the small number ($E_{internal}$) is near the roundoff noise of the original numbers (E_{total} and $E_{kinetic} + E_{magnetic}$).

To overcome this, we have implemented two algorithms that solve an additional equation to track the small numbers; the modified entropy equation given in Ryu et al. (1993) and the internal energy equation given in Bryan et al. (1995). These two equations are:

$$\frac{\partial S}{\partial t} + \frac{1}{a}\nabla \cdot (S\mathbf{v}) = -\frac{3(\gamma-1)\dot{a}}{a}S \tag{2.41}$$

$$\frac{\partial \rho e}{\partial t} + \frac{1}{a}\nabla \cdot (\rho e\mathbf{v}) = -\frac{3(\gamma-1)\dot{a}}{a}\rho e + \frac{p}{a}\nabla \cdot \mathbf{v} \tag{2.42}$$

where $S \equiv p/\rho^{\gamma-1}$ is the comoving modified entropy and e is the internal energy. The modified entropy equation is valid only outside the shocks where the entropy is conserved. Use of either (not both) of these equations is at the discretion of the simulator.

Through the course of the simulation, the ratio of internal energy to total energy is monitored. When this ratio is less than some preset value η, one of the modified equations is used. As in Li et al. (2008), we use $\eta = 0.008$. They note that reducing this parameter will cause a decrease in the volume filled by low temperature gas, as most of the gas affected by the switch is cold, high velocity gas. The optimal choice for this parameter is still an open question for the general situation. Li et al. (2008) compared this two approaches and found almost identical results.

2.2.11 Adaptive Mesh Refinement

Structured AMR, initially devised by Berger & Colella (1989), is a technique for increasing resolution of a simulation in parts of a simulation that require higher resolution for increased accuracy or suppression of numerical artifacts, while conserving memory and CPU cycles in areas that don't. Refinement criteria will not be described here, as they vary from simulation to simulation. AMR has four basic necessary parts:

1. **Patch Solver** This is the algorithm that actually solves the finite volume PDEs in question, as described by Sections 2.2.6 - 2.2.10. The approximations used for the patch solver are conservative in a finite volume sense, and the rest of the choices are made to preserve that conservation.

2. **Refinement Operator** This is the routine that creates fine resolution elements from coarse ones. In Enzo, we use conservative, volume weighted interpolation for the fluid quantities $\rho, E, \vec{v}$. For the magnetic fields, we use the method described by Balsara (2001), with some slight modifications in implementation. This method constructs a quadratic divergence free polynomial, and area-weighted averages are used for the fine grid quantities. This is described in more detail in appendix A.1.

3. **Projection Operator** This is the routine that projects the fine grid data back to the parent coarse grid. For Enzo, the parent grid is simply replaced by a volume-weighted average of the fine cells. For the face centered magnetic field, this is an area weighted average, though in practice we don't explicitly average the magnetic field, as discussed in below and in appendix A.1.1

4. **Correction Operator** Once the projection operator replaces the solution on the coarse grids, the evolution on the coarse grids is no longer consistent with the underlying equations in the manner they were discretized. That is to say, the total change of any conserved quantity inside the region is no longer equal to the flux across its surface. For the Enzo hydro fields, this is corrected with the flux correction mechanism. More details on this and the modifications in EnzoMHD see appendix A.2

EnzoMHD does all of these steps for the fluid quantities, but for the magnetic field it slightly alters this procedure. In order to overcome a shortcoming in the original data structures used in Enzo, we combined the projection and correction operations for the magnetic fields in one step. The net effect of the correction operator is to ensure that all zones are updated by finest resolution fluxes available, even if they were updated by coarse data initially. For the magnetic field update, we don't project the actual magnetic field that is of interest, but rather the electric field (effectively the 'flux' for B_f), then take the curl of the newly projected electric field. Thus the coarse magnetic data co-located with the fine grids get updated with the fine data, and the bounding zones don't need correction at all.

More detail on this process can be found in Appendices A.1 and A.2

2.3 Numerical Experiments

EnzoMHD has many configurations available. Here, we test some of the possible configurations, to indicate the quality of solution possible with EnzoMHD.

2.3.1 MHD Tests without AMR

We first test our code in unigrid (fixed resolution) mode, in order to ensure consistency of the patch solver with the algorithm described in Li et al. (2008). We do two one dimensional cosmology tests (Caustics and Zel'dovich Pancake), one one-dimensional non-cosmological tests (Brio and Wu), one 2D non-cosmological test (Orszag Tang) and one 3D cosmological test.

Brio and Wu Shock Tube

The shock tube defined by Brio & Wu (1988) is a standard test of any MHD solver, as it displays a number of the important MHD waves, including a compound wave. Compound waves are not a property of pure hydrodynamics, because the system is convex. However, due do the more complex nature of the MHD equations, certain initial conditions can cause flows in which at one point the shock speed in a given family is higher than the wave speed for that family, causing a shock, but lower in the post shock region, causing a rarefaction immediately following the shock.

This can be seen in Figure 2.4. The problem was run with 800 zones to a time $t = 0.2$, using the HLLD solver in Enzo. This shock tube shows, from left to right, a fast rarefaction, slow compound (shock+rarefaction), contact, slow shock, and fast rarefaction. It can be seen that this solver captures this shock tube problem quite well.

One-dimension MHD Caustics

This test is taken from Li et al. (2008), which initially derived from a pure hydro version from Ryu et al. (1993). This problem is used to test the ability of the code to capture shocks and to deal with hypersonic flows. Initially, $v_x = -\frac{\pi}{2} sin(2\pi x)$, $\rho = 1$ and $p = 10^{-10}$. Caustics are formed because of the compression by the velocity field. The Mach number of the initial peak velocity is 1.2×10^4. The pressure can easily become negative for such high Mach number flow.

We performed the test with same magnetic field settings as in Li et al. (2008). The magnetic field in the x and z directions are always zero while $B_y = 0, 0.001, 0.02$ and 0.05. The calculation was done with 1024 cells and the results at $t = 3$ are shown

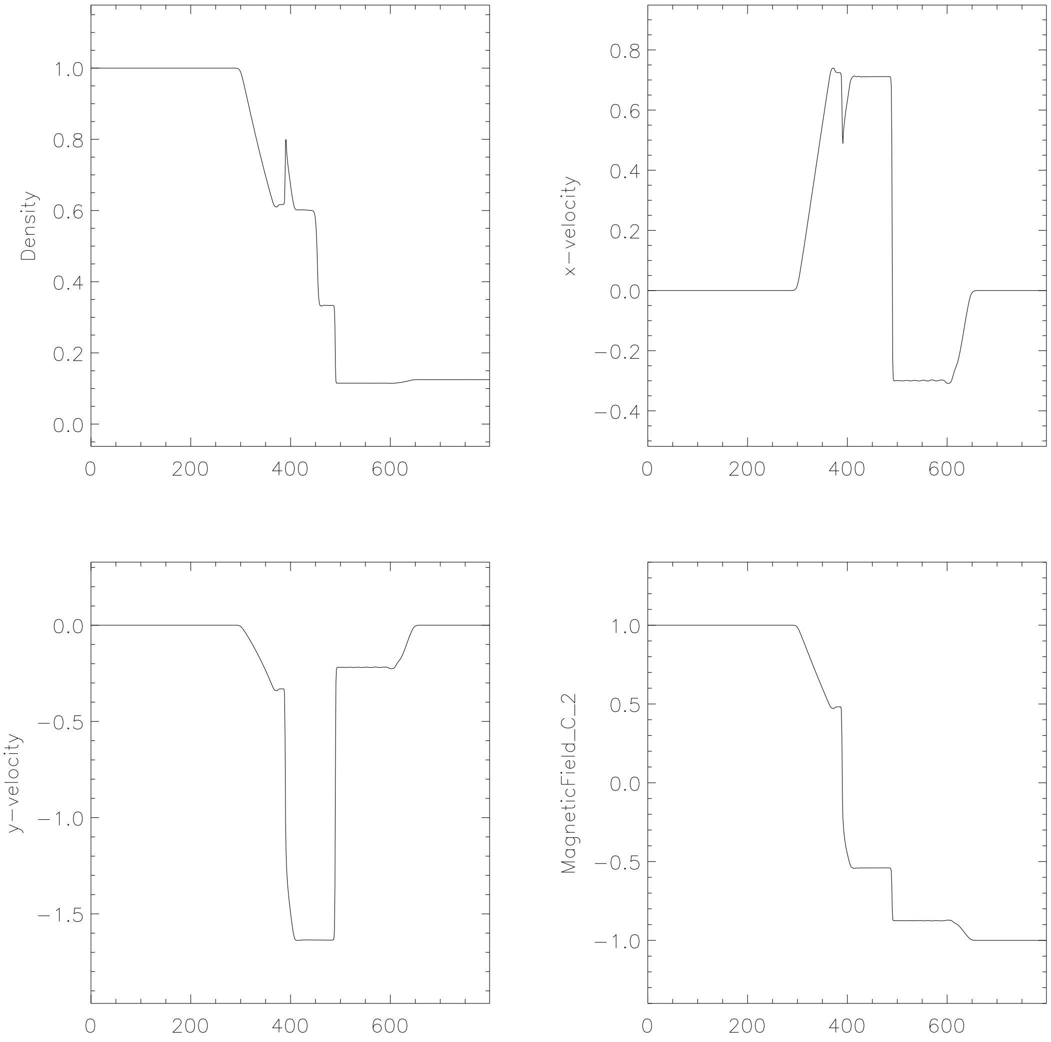

Figure 2.4: The shock tube of Brio & Wu (1988), showing from left to right a fast rarefaction, slow compound (shock+rarefaction), contact, slow shock, and fast rarefaction. T=0.08, and 800 zones were used.

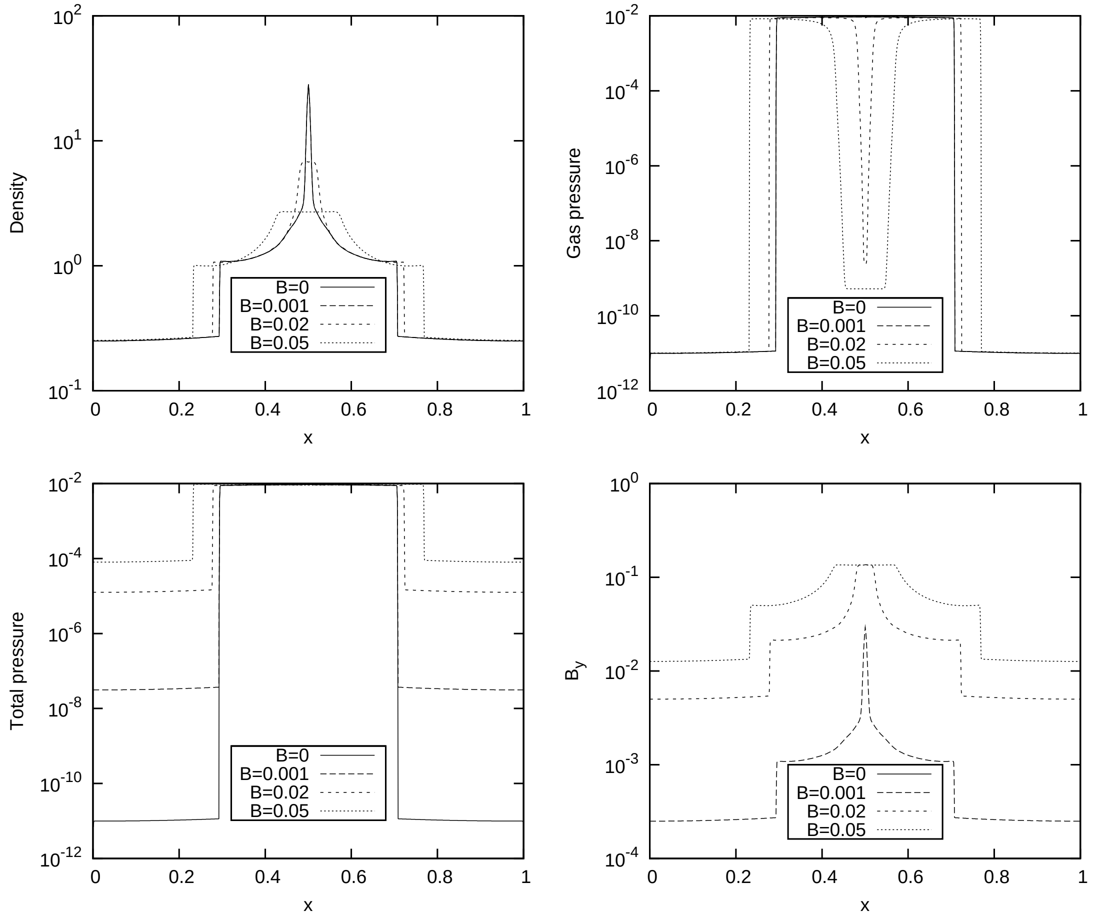

Figure 2.5: 1-D MHD caustics at $t = 3$. Density, gas pressure, total pressure and B_y are plotted. For the small field runs, almost no change can be seen, while larger field runs decrease the peak of the density considerably due to the increased pressure.

in Figure 2.5. Our results match the results from CosmoMHD (Li et al., 2008) quite well, as expected.

The Zel'Dovich Pancake

The Zel'Dovich pancake is a popular test problem for codes that include gravity in comoving coordinates. The problem setups are taken from Li et al. (2008). This takes place in a purely baryonic universe with $\Omega = 1$ and $h = \frac{1}{2}$. The initial scale factor $a_i = 1$ corresponds to $z_i = 20$. The initial velocity field is sinusoidal with the peak value $0.65/(1 + z_i)$, and $v = 0$ at the center of the box. The initial comoving box size is 64 h^{-1} Mpc. The shocks forms at $z = 1$. The initial baryonic density

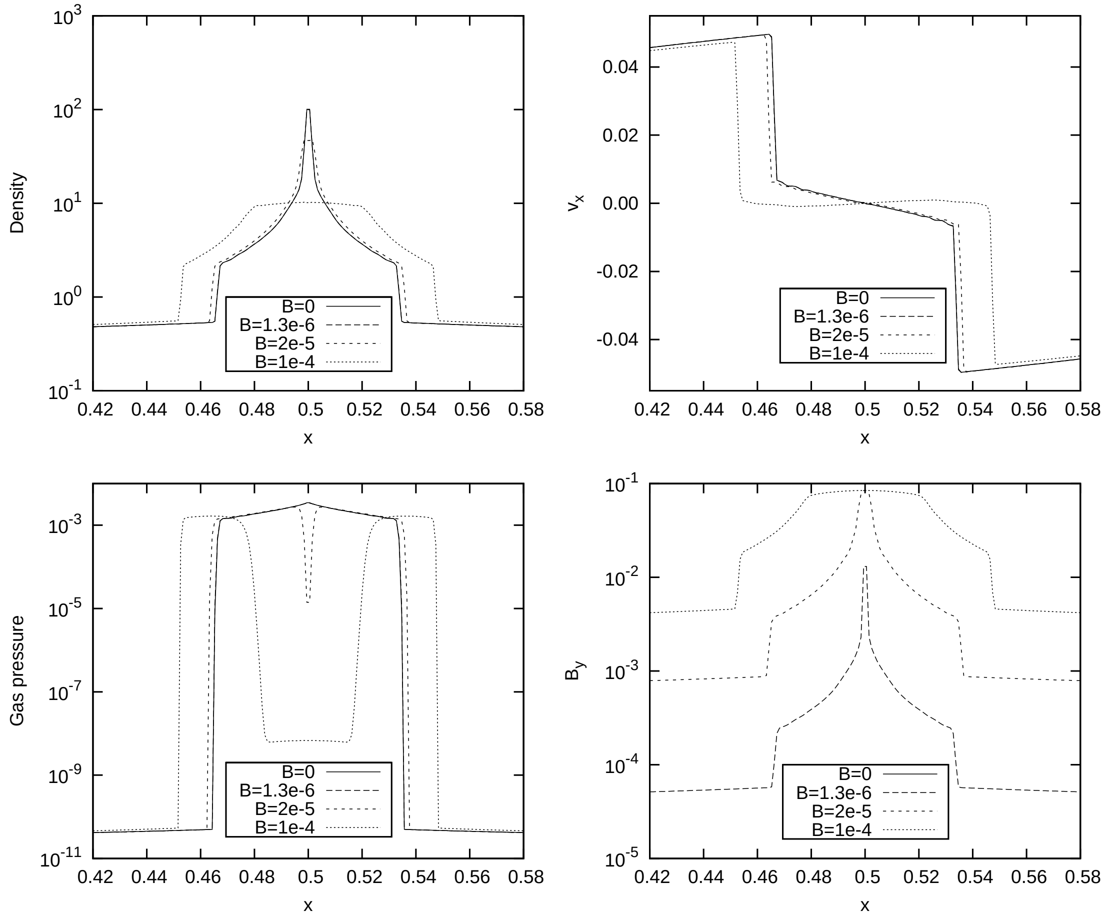

Figure 2.6: The Zel'Dovich Pancake problem with various values of the magnetic field, at $t = 0$. Increasing the magnetic field strength increases the central magnetic pressure, reducing the density and changing the overall solution structure. Results match those of Li et al. (2008).

and pressure are uniform with $\rho = 1$ and $p = 6.2 \times 10^{-8}$. The tests were run with 1024 cells, both with and without magnetic fields. Our results are almost identical to the results from CosmoMHD (Li et al., 2008), as expected. Results can be seen in Figure 2.6.

Orszag-Tang

The Orszag-Tang Vortex was originally developed by Orszag & Tang (1979) to demonstrate that small scale structure can be generated by the nonlinearities in the MHD equations. It initially starts with a single large scale rotating velocity structure and two circular magnetic structures. From these simple large scale initial conditions, substantial small scale structure is formed. It now serves as a standard test problem to demonstrate the accuracy and diffusivity of MHD codes.

The initial conditions are on a 2 dimensional periodic box, 256 zones on a side. $\mathbf{v} = v_0(-sin(2\pi y)\hat{x} + sin(2\pi x)\hat{y}, \mathbf{B} = B_0(-sin(2\pi y)\hat{x} + sin(4\pi x)\hat{y}), v_0 = 1, B_0 = 1/\sqrt{4\pi}, \rho_0 = 25/(36\pi), p_0 = 5/(12\pi)$, and $\gamma = 5/3$ which gives a peak Mach number of 1 and peak $\beta = p_0/(B_0^2/2) = 10/3$. Figure 2.7 shows the density at $t = 0.48$, from which one can see that the solution agrees with other solutions to the problem in the literature.

3D Adiabatic Universe with MHD

We have also performed the 3D adiabatic CDM Universe test described by Li et al. (2008) both with and without magnetic fields. We also compared the non-magnetized results with the results run using the PPM solver (Colella & Woodward, 1984). Adiabatic evolution of a purely baryonic Universe was computed with an initial CDM power spectrum with the following parameters: $\Omega = \Omega_b = 1$, $h = 0.5$, $n = 1$ and $\sigma_8 = 1$ in a computational volume with side length $L = 64$ h^{-1} Mpc. The transfer function from Bardeen et al. (1986) was used to calculate the power spectrum of the initial density fluctuations. Evolution was done from $z = 30$ to $z = 0$. We used 256^3 cells for each simulation. The comparisons are made at the final epoch, $z = 0$. Though this test is identical to that of Li et al. (2008), our results can't compared with theirs directly since different random seeds were used for the realization of the initial density and velocity.

Figure 2.8 shows a comparison of the mass-weighted temperature distribution, Figure 2.9 is a comparison of the volume-weighted density distribution. The discrepancies between PPM and MHD solvers are small, indicating the two codes perform roughly the same. The nature of the differences is expected, since PPM solver has third order accuracy while the MHD solver has second order accuracy and larger numerical diffusion. This allows PPM to capture shocks in fewer zones, which causes the dense shocked gas to not only have a smaller volume fraction, but also be hotter and slightly less dense than in the MHD solver.

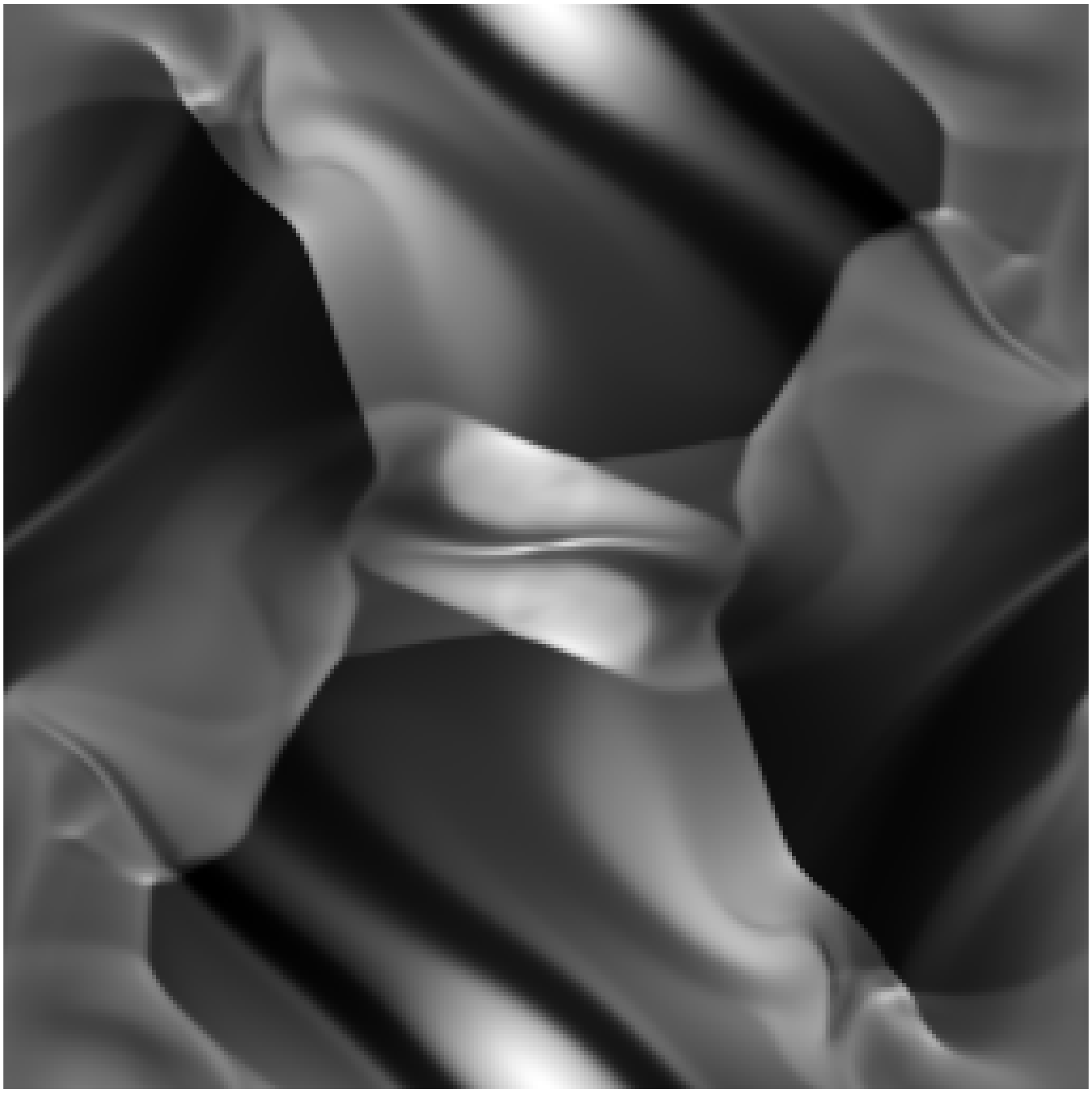

Figure 2.7: Density from the Orszag-Tang vortex, at t=0.48. Initial conditions are uniform density, with a single rotating velocity structure and two circular magnetic structures. This generates significant small scale structure, which has been used to compare effective resolution of different MHD schemes.

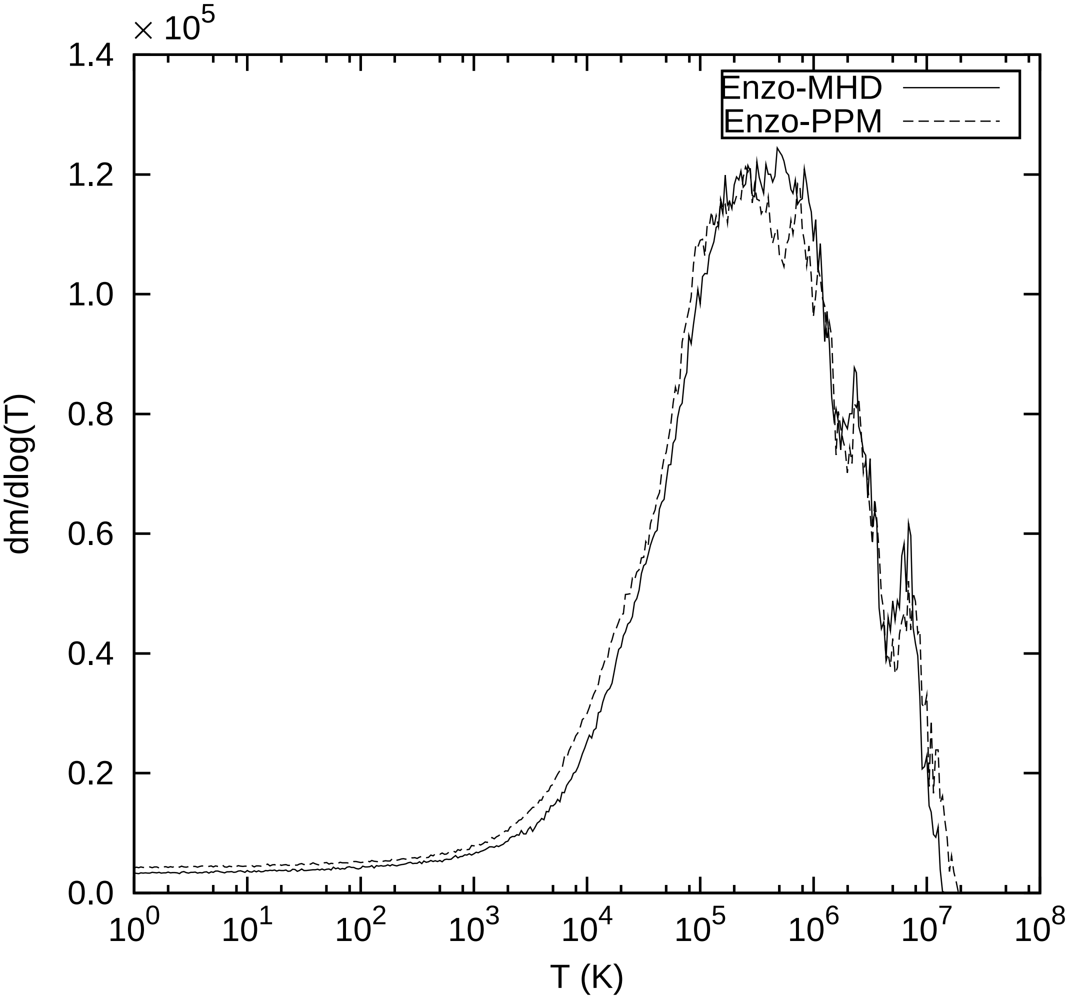

Figure 2.8: Comparison of mass-weighted temperature histogram at $z = 0$ for the 3D purely baryonic adiabatic Universe simulation. The solid line is from the MHD code and the dashed line is from Enzo-PPM.

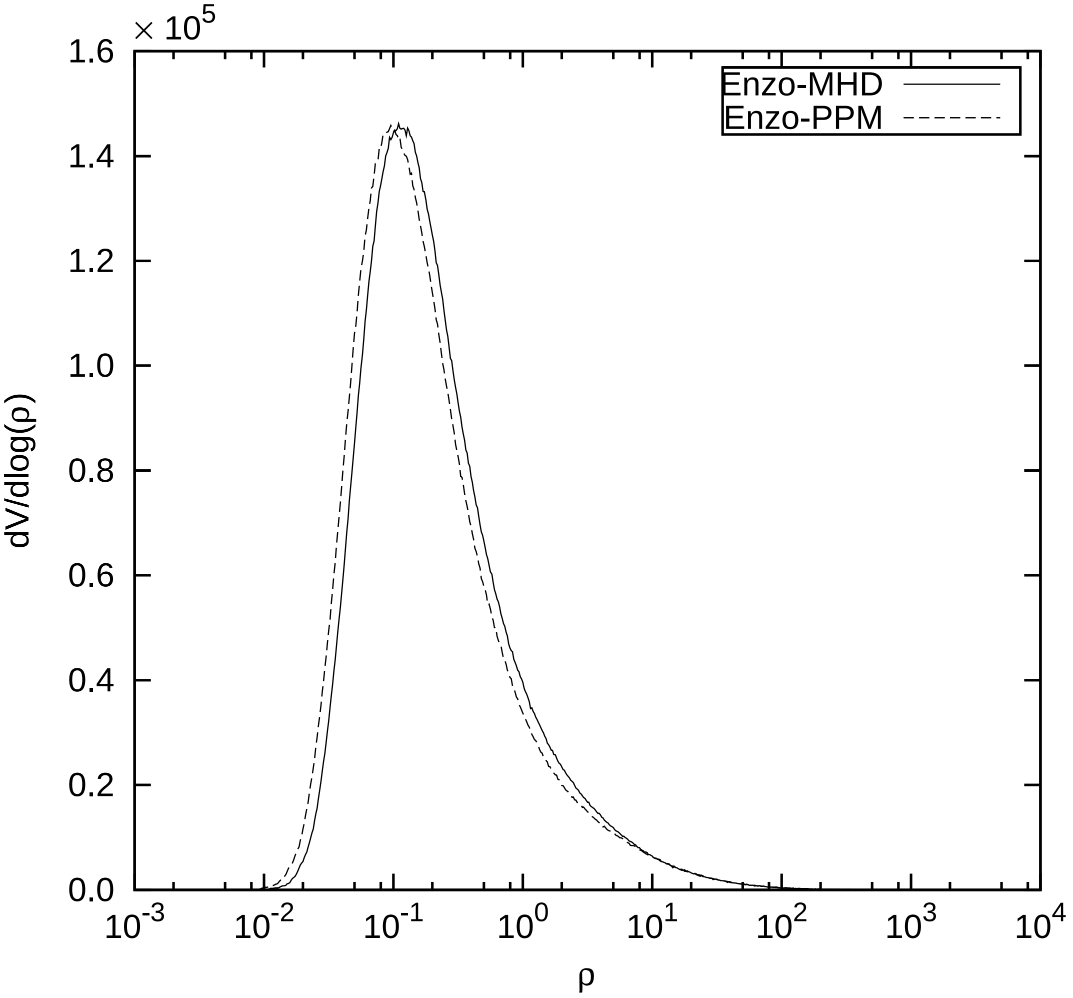

Figure 2.9: Comparison of volume-weighted density histogram at $z = 0$ for the 3D purely baryonic adiabatic Universe simulation. The solid line is from the MHD code and the dashed line is from Enzo-PPM.

We have also done a similar run with the same initial conditions to the above, but with an initial magnetic field, $B_x = B_z = 0,\ B_y = 2.5 \times 10^{-9}$ Gauss, which is 4.32×10^{-7} in code units. Figure 2.10 shows the scaled divergence of the magnetic fields, averaged over the entire box, as a function of redshift. The scaled divergence is $< |h\nabla \cdot \mathbf{B}/|\mathbf{B}|| >$, where $h = 1/256$ is the spatial scale, and $|B|$ is the local maximum magnetic field strength, is the most relevant measure of the potential numerical effects of divergence. The divergence of the magnetic fields is close to the round-off error.

2.3.2 MHD Tests with AMR

To test the Adaptive Mesh Refinement, we ran a sample of the tests from the previous section with AMR, to ensure no spurious artifacts are introduced by the AMR. These are the one dimensional caustic and pancake tests. In addition, the tests of Adiabatic Expansion and a complete galaxy cluster formation are also run.

Three-Dimension MHD Adiabatic Expansion

This test is taken from Bryan et al. (1995). This test uses a completely homogeneous universe with initial $T_i = 200$ K and $v_i = 100$ km s^{-1} in the x-direction at an initial redshift of $z_i = 20$. In the code units, the initial density is 1.0 and initial velocity is 2.78×10^{-3} and the initial pressure is 1.24×10^{-9}. Additionally we have a uniform magnetic field $B_x = B_y = B_z = 1 \times 10^{-4}$ in code units, which is 2.66×10^{-7} G in cgs units. The simulation used a 16^3 root grids with 2 levels of refinement in the center region and ran to $z = 0$.

The expansion terms in eqns (2.1) - (2.4) operate like drag terms, so that in the absence of a source, the velocity decreases as $v = v_i a^{-1}$, the temperature as $T = T_i a^{-2}$ and the magnetic field should decrease as $a^{-1/2}$.

The temperature at $z = 0$ is 0.453406 K, 0.024% below the analytic result of 0.453515 K. The velocity at $z = 0$ is 4.76176 km s^{-1}, compared to the analytic result 4.7619 km s^{-1}, a 0.0029% discrepancy. The final magnetic field strength is 6.03×10^{-10} G (2.18×10^{-5} in the code unit), a difference of 0.0006% with respect to the analytic solution. Figure 2.11 shows the B_y as a function of redshift, the solid

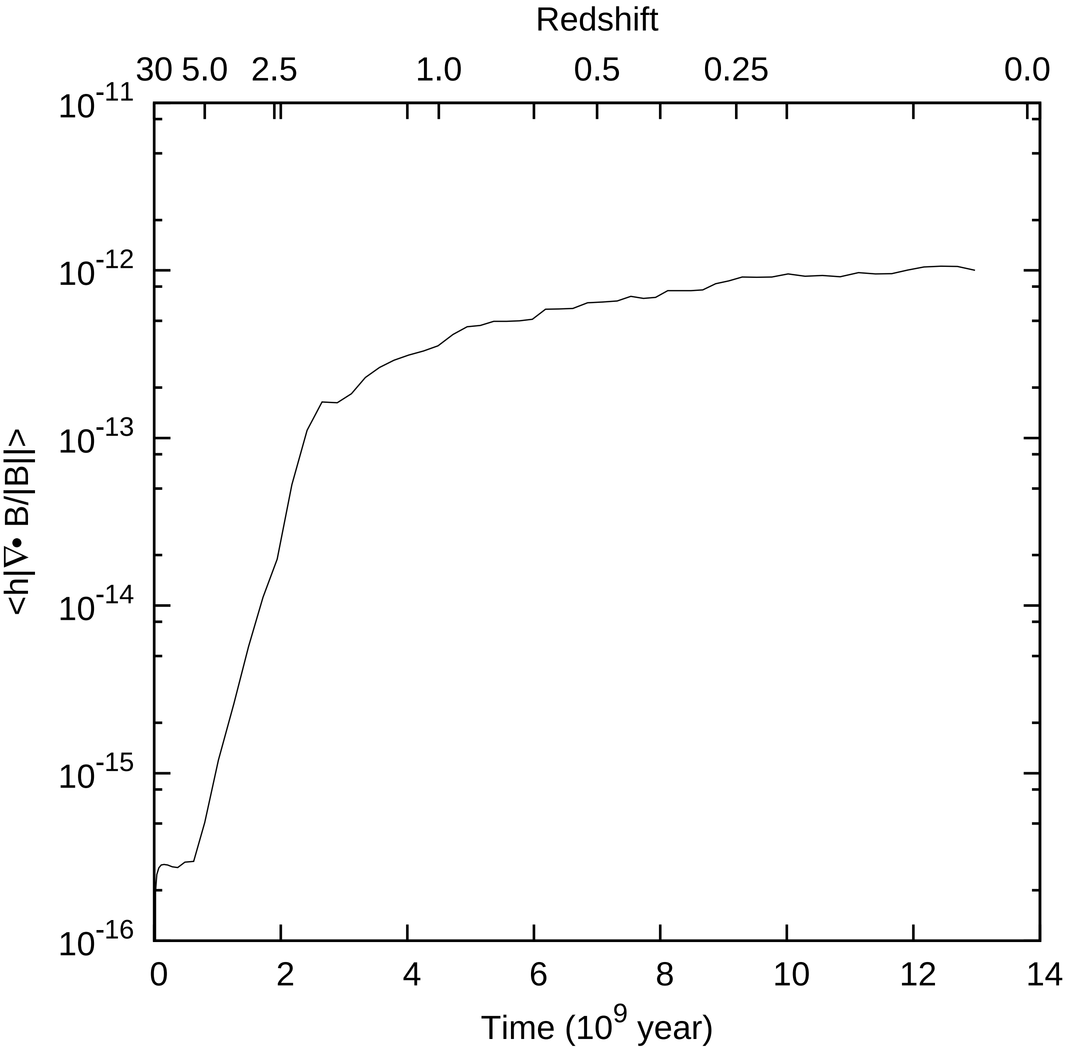

Figure 2.10: The scaled divergence $< |h\nabla \cdot \mathbf{B}/|\mathbf{B}|| >$ of the magnetic fields for the 3-D simulations of a purely baryonic adiabatic Universe. Here $h = 1/256$ is the scale length and $|B|$ is the local magnetic field norm, and the average is over the entire volume. Scaled divergence is a more relevant measure of numerical effects of divergence than the strict divergence. As desired, the divergence is near the machine round off noise, the theoretical limit.

line shows the theoretical value.

One-Dimensional MHD Caustics with AMR

We also ran the the 1d MHD caustic test with AMR, using 256 root grid zones with 2 levels of refinement, again by a factor of 2, giving an effective resolution is 1024 cells. Figure 2.12 shows comparisons of density and gas pressure of non-AMR and AMR runs with different initial magnetic field strengths, as described before. Figure 2.13 shows the comparisons of B_y for runs with different initial values of B_y. In both plots, the AMR result is sampled to the finest resolution. The AMR runs give almost identical results to the unigrid runs, while the CPU time and memory were greatly saved in the AMR runs.

Zel'Dovich Pancake with AMR

We also ran the pancake problem with AMR. The problem was set up with the same initial conditions as the unigrid run, but with a root grid of 256 root cells and 2 levels of refinement by 2. We compared these results having effectively 1024 cells to the results of our previous high resolution which actually had 1024 cells. Figure 2.14 shows comparisons of density and gas pressure between the non-AMR and AMR runs, with different initial values for B_y. Figure 2.15 shows the comparisons of B_y with different initial values. Again, the AMR computation got very similar results, while saving CPU and memory resources.

MHD Galaxy Cluster Formations

Cluster formation (without MHD) has been studied intensively by researchers using Enzo (Norman, 2005; Bryan & Norman, 1998; Loken et al., 2002; Motl et al., 2004; Hallman et al., 2006). It is one of the most important applications of Enzo's high dynamic range. Many cluster simulations have been run with Enzo with a wide variety of physics (i.e. radiative cooling, star formation, etc) and we can compare these results to similar simulations run with MHD. More information about Enzo simulated cluster can be found in Simulated Cluster Archive at http://lca.ucsd.edu/data/sca/. Here, we present just one simulation to demonstrate the MHD code.

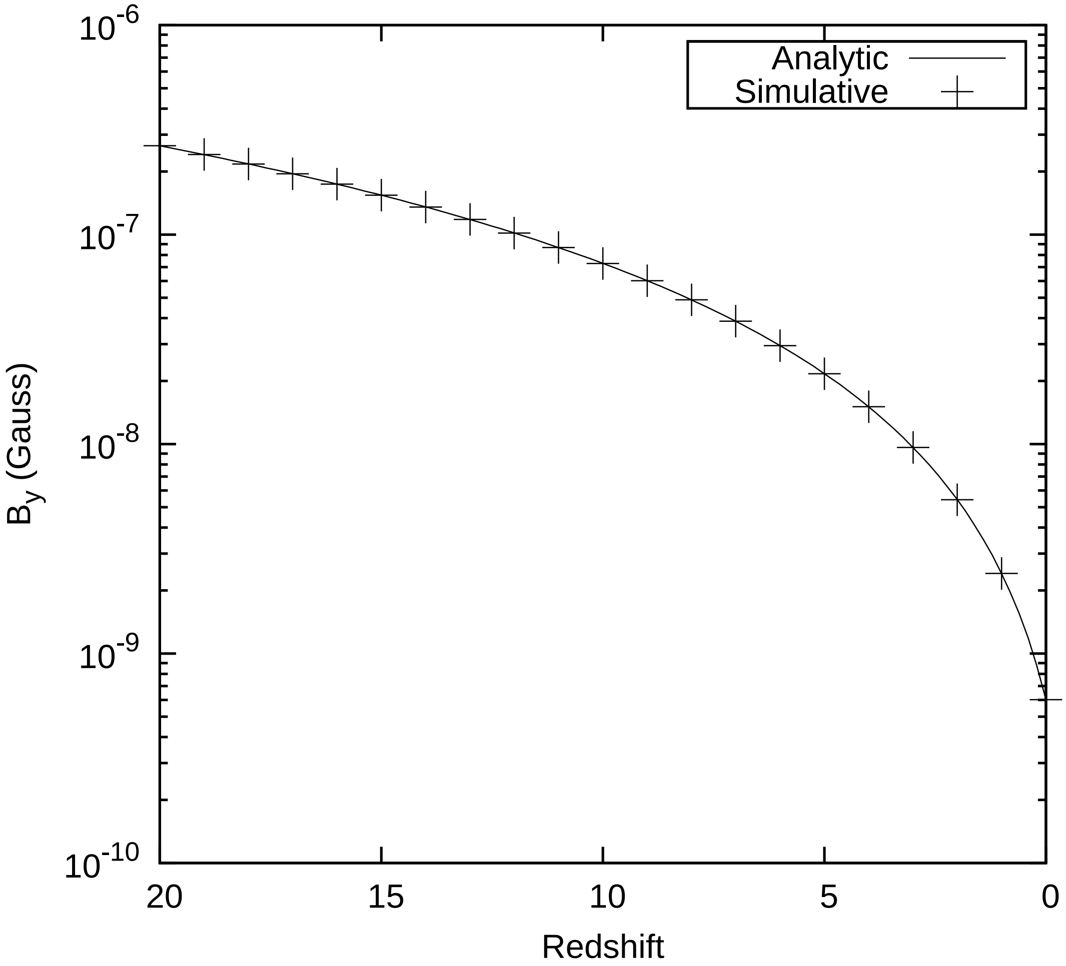

Figure 2.11: Magnetic field in the y direction in the AMR MHD adiabatic expansion test. The pluses show the results of simulation and the solid line is the analytic result.

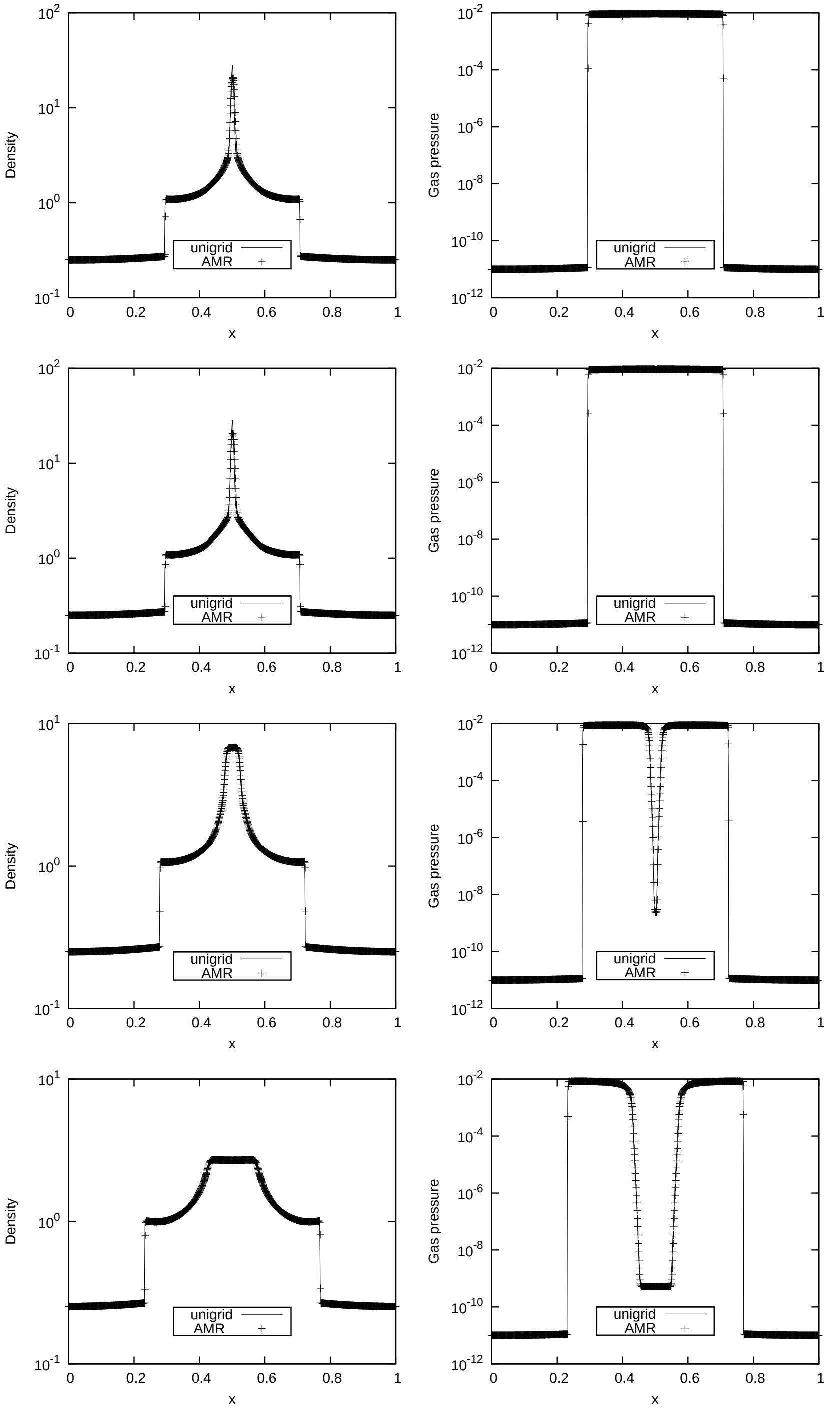

Figure 2.12: Comparisons of density and pressure in the MHD caustic tests, non-AMR vs AMR. The left column shows density and the right column shows gas pressure. Initial magnetic field of each row from top to bottom is 0, 0.001, 0.02 and 0.05.

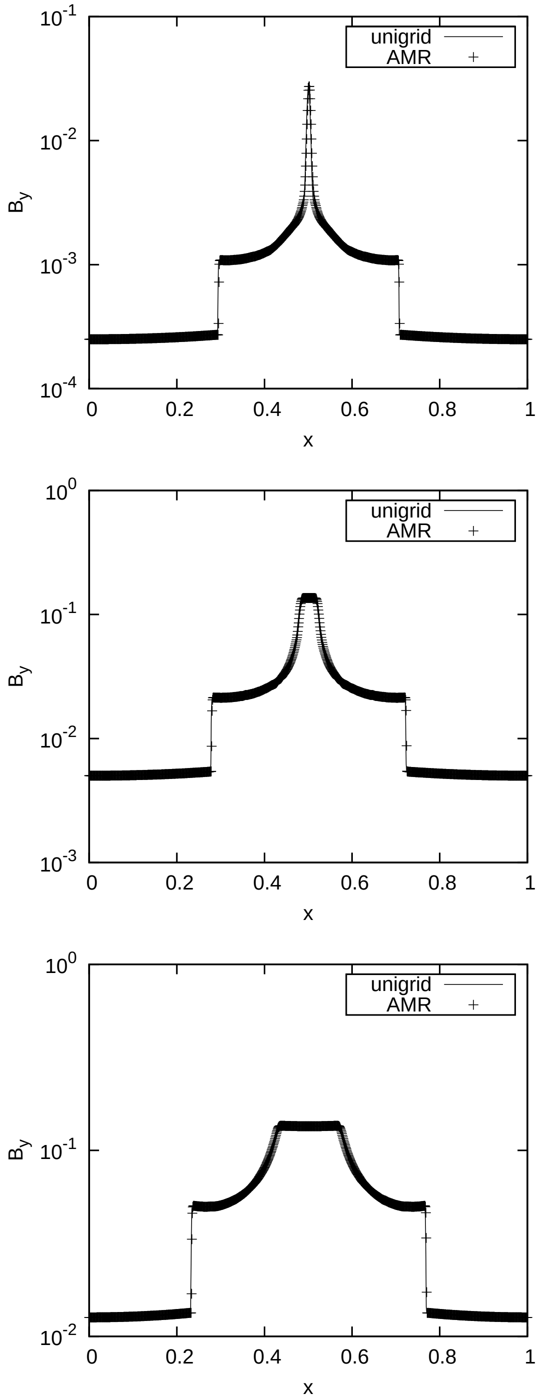

Figure 2.13: Comparison of B_y in the MHD caustic tests, non-AMR vs AMR. Initial magnetic field of each panel from top to bottom is 0.001, 0.02 and 0.05.

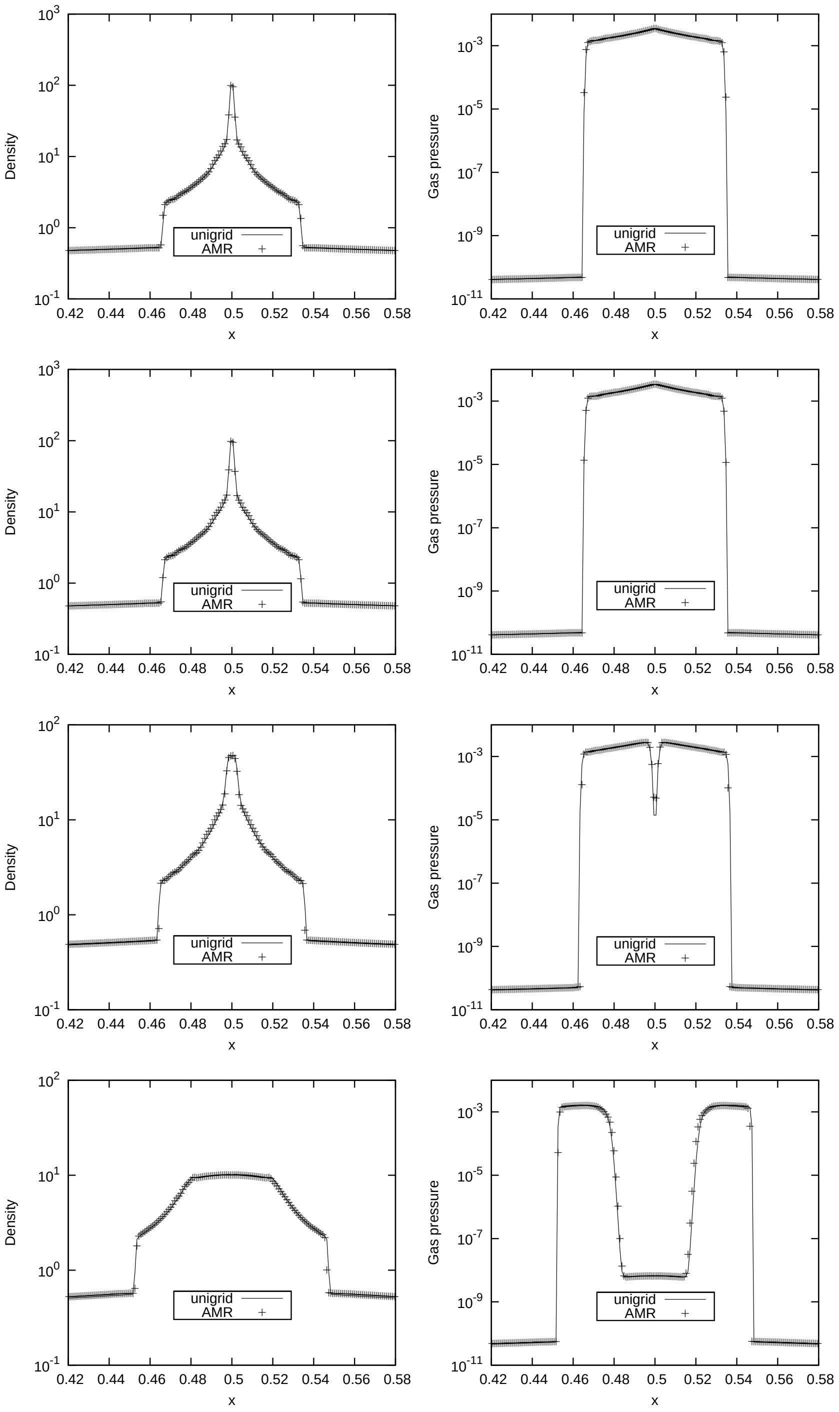

Figure 2.14: Comparisons of density and pressure in non-AMR and AMR runs of the pancake test. The left column shows density and the right column shows gas pressure. Initial magnetic field of each row from top to bottom is 0, 1.3e-6, 2e-5 and 1e-4 G.

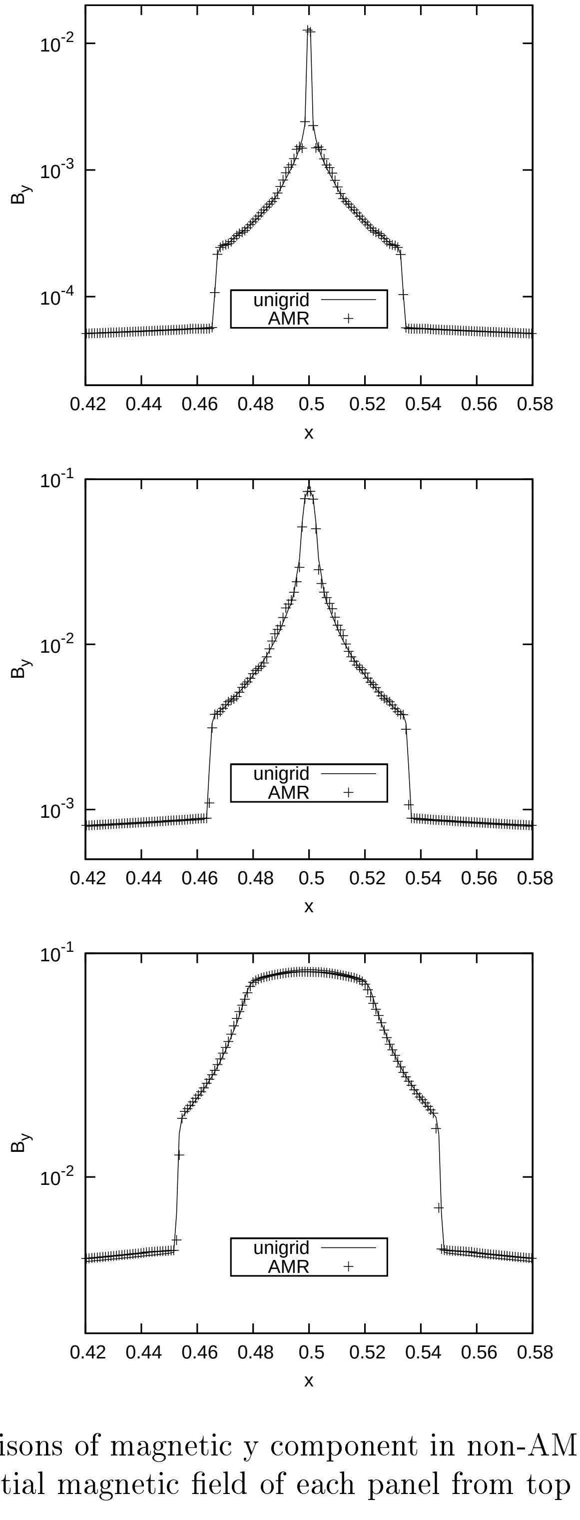

Figure 2.15: Comparisons of magnetic y component in non-AMR and AMR runs of the pancake test. Initial magnetic field of each panel from top to bottom is 1.3e-6, 2e-5 and 1e-4 G.

This simulation uses a Lambda CDM cosmology model with parameters $h = 0.7$, $\Omega_m = 0.3$, $\Omega_b = 0.026$, $\Omega_\Lambda = 0.7$, $\sigma_8 = 0.928$. The survey volume is 256 h^{-1} Mpc on a side. The simulations were computed from a 128^3 root grid with 2 level nested static grids in the center where the cluster form. This gives an effective resolution of 512^3 cells (0.5 h^{-1} Mpc per cell) and dark matter particle mass resolution of 1.49×10^{10} $M_\odot$ initially in the central region. Adaptive mesh refinement is allowed only in the region where the galaxy cluster forms, with a total of 8 levels of refinement beyond the root grid, for a maximum spatial resolution of 7.8125 h^{-1} kpc. While the baryons are resolved at higher and higher spatial and mass resolution at higher levels, the dark matter particles maintain constant mass so as not to add any additional noise. The simulations are evolved from $z = 30$ to $z = 0$, and all results are shown at the redshift $z = 0$. We concentrate our study on a cluster of $M = 1.2 \times 10^{15}$ $M_\odot$.

In order to isolate the effects of the numerical approximation from the effects of MHD, we first run the simulations adiabatically without additional physics and the magnetic field set to zero, and compare to a PPM run with identical parameters. In Table 2.1, we list the basic parameters for the clusters formed in each solver. The viral radius, R_{vir} is calculated for an over density $\frac{\delta\rho}{\rho}$ of 200. M_{vir}, M_{dm} and M_{gas} are the total mass, mass of the dark matter and mass of the baryon inside the virial radius, respectively. T_{vir} is the average of the temperature of the ICM inside the virial radius. Evidently, there is very little difference between the results from the two solvers.

Figures 2.16-2.18 show the images of the logarithmic projections of the dark matter density, gas density, and X-ray weighted temperature, respectively, at $z = 0$. Both PPM and MHD solvers show very similar images in all three quantities, differing only slightly in the small scale details.

Figure 2.19-2.21 show the radial profiles of dark matter density, gas density, and x-ray weighted temperature. The profiles match quite well in all three quantities, with only minor differences. There is a slight deviation in the radial profiles of dark matter density near the center of the cluster, but this is near the resolution limit of the simulation, so not a trustworthy data point. In the density profile, it can be seen that the MHD solver gives a slightly higher average density. The temperature

Table 2.1: Comparison of properties of clusters from Hydrodynamics and MHD simulations.

Parameter	Hydro PPM	MHD
$R_{vir}(Mpc)$	2.229	2.227
$M_{vir}(M_{\odot})$	1.265e+15	1.260e+15
$M_{dm}(M_{\odot})$	1.097e+15	1.097e+15
$M_{gas}(M_{\odot})$	1.672e+14	1.632e+14
$T_{vir}(K)$	8.684e+07	8.663e+07

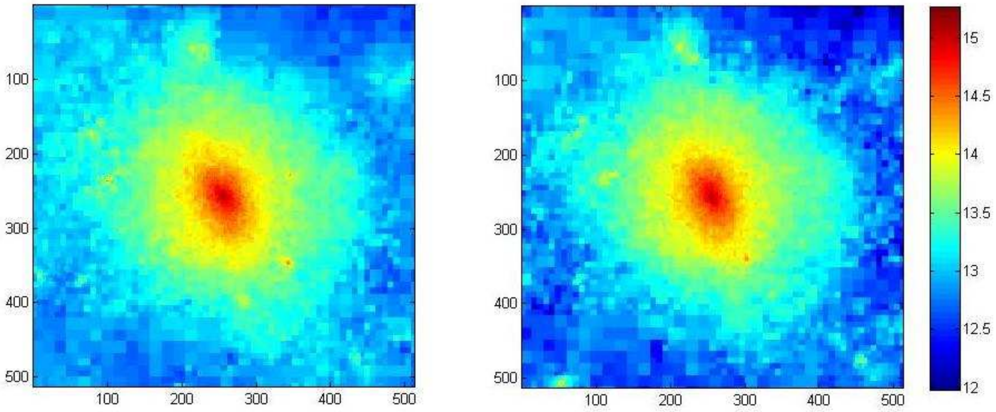

Figure 2.16: Logarithmic projected dark matter density at $z = 0$. The images cover the inner 4 h^{-1} Mpc of cluster centers. The left panel shows the result from the PPM solver and the right panel shows the result from the MHD solver. The color bar is in $M_{\odot}$ Mpc^{-2}.

agreement is good enough to not worry about.

We have also run the simulations with non-zero initial magnetic field. A uniform initial magnetic field of 9.72753×10^{-10} G (1×10^{-7} in the code unit) in the y direction was added to the system at the start of simulation at $z = 30$. Since Dolag et al. (1999) has shown that the initial magnetic fields structures are not important to the final magnetic fields structures in their MHD SPH simulations, no other initial magnetic fields configuration will be used in this chapter. Figure 2.22 shows 4 projections of the cluster center: gas density, temperature, magnetic energy, and synthetic Faraday rotation measurement $RM = \frac{e^3}{2\pi m^2 c^4} \int_0^d n_e B ds$. We can see that the gas density and temperature images are almost identical to the MHD run with zero magnetic fields.

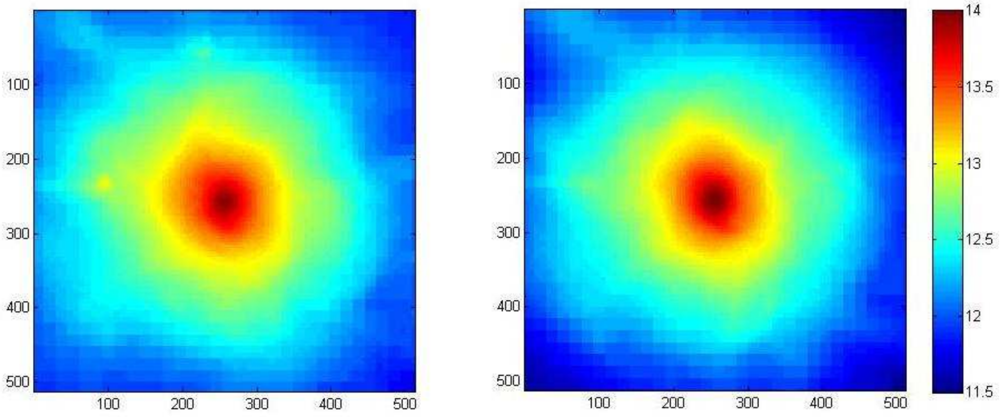

Figure 2.17: Logarithmic projected gas density at $z = 0$. The images cover the inner 4 h^{-1} Mpc of cluster centers. The left panel shows result from PPM solver and the right panel shows result from MHD solver. The color bar is in $M_{\odot}$ Mpc^{-2}.

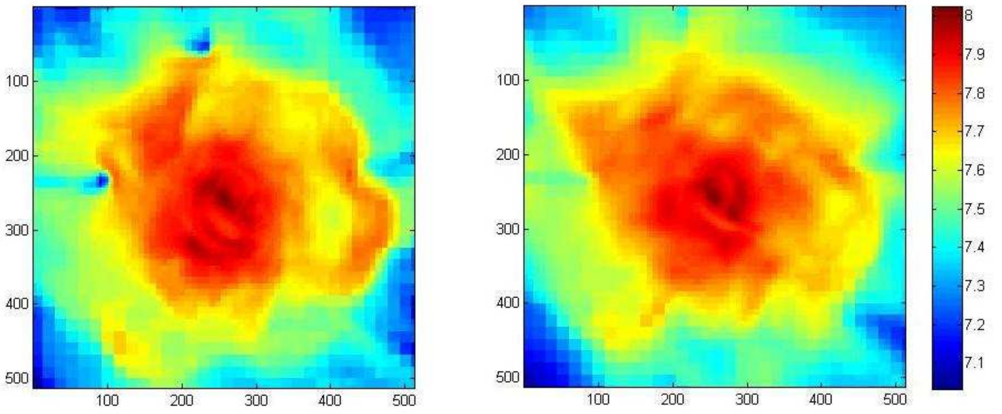

Figure 2.18: Logarithmic projected X-ray weighted temperature at $z = 0$. The images cover the inner 4 h^{-1} Mpc of cluster centers. The left panel shows result from PPM solver and the right panel shows result from MHD solver. The unit is Kelvin.

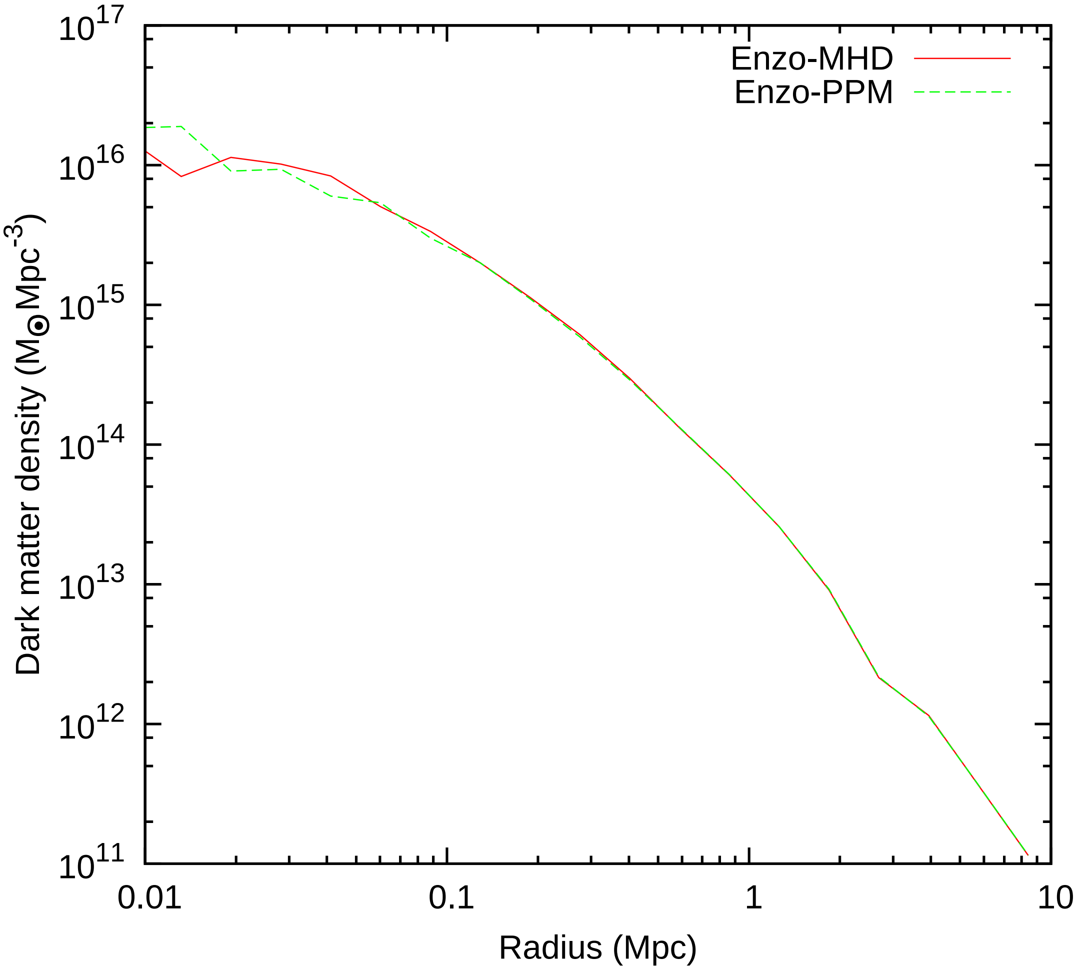

Figure 2.19: Spherically averaged dark matter density radial profile at $z = 0$ from MHD solver and PPM solver.

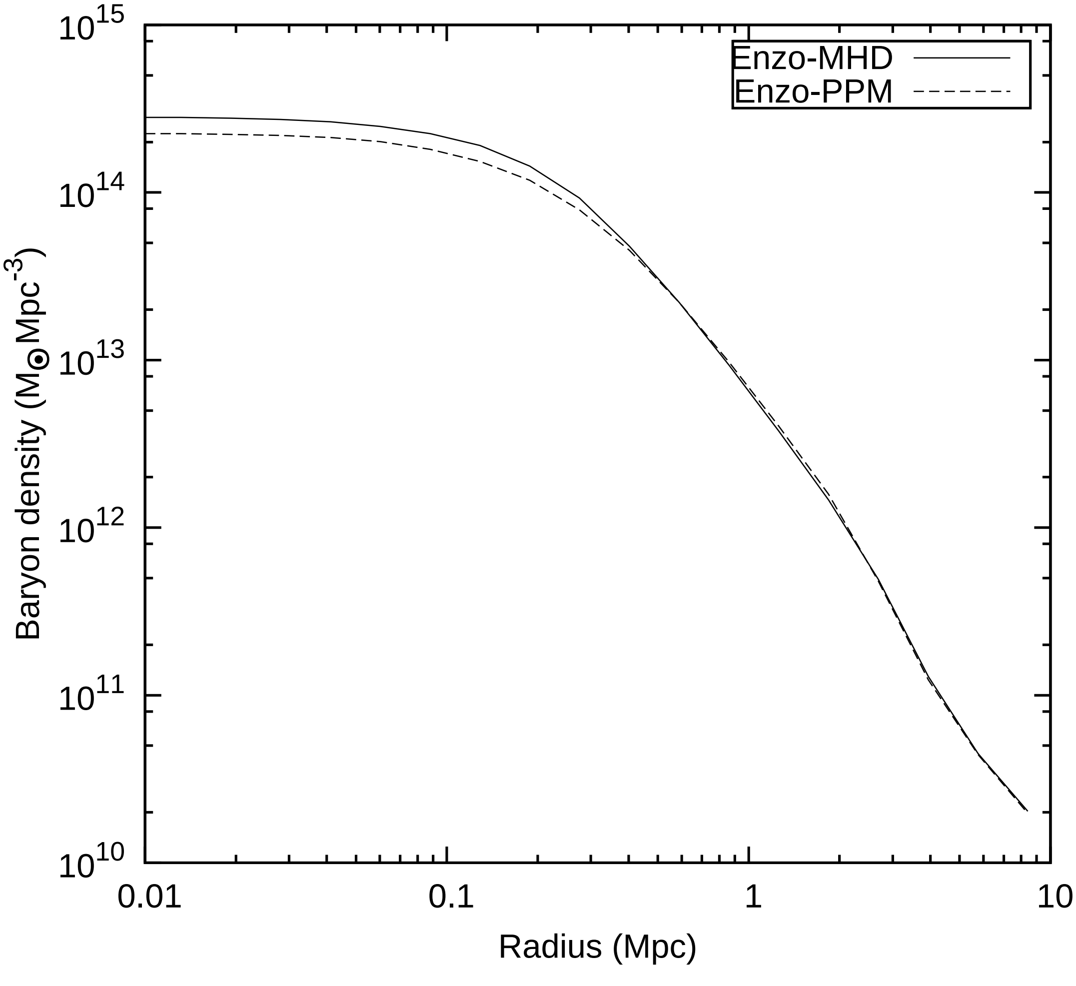

Figure 2.20: Spherically averaged gas density radial profiles at $z = 0$ from MHD solver and PPM solver.

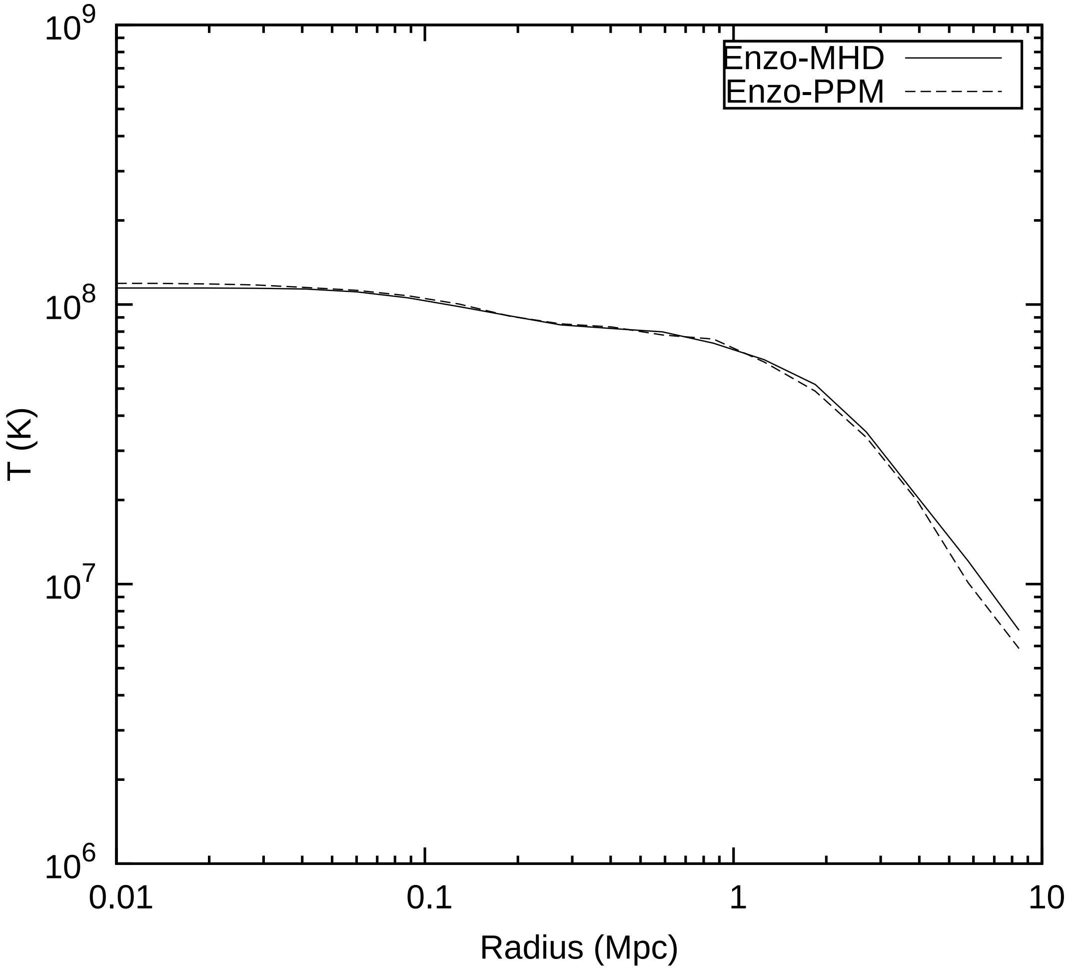

Figure 2.21: Spherically averaged temperature radial profiles at $z = 0$ from MHD solver and PPM solver..

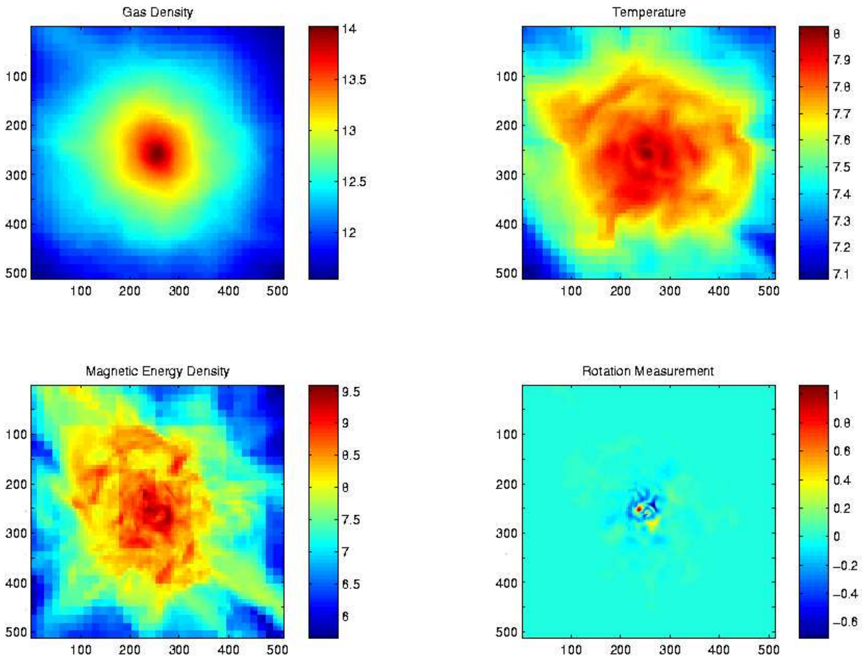

Figure 2.22: Images of gas density ($M_\odot\ Mpc^{-2}$), temperature (K), magnetic energy density ($erg\ cm^{-2}$) and rotation measure ($rad\ m^{-2}$) of the galaxy cluster simulation with an initial magnetic field $B_y = 9.72753 \times 10^{-10}$ G. Projections are of the inner 4 Mpc/h of cluster center at $z = 0$.

As expected, the magnetic energy is concentrated in the cluster core. The maximum magnetic fields is 1.0630270×10^{-8} G. The RM is about 2-3 $rad\ m^{-2}$ at the cluster core. Figure 2.23 shows comparison of the radial profiles of the simulations with and without initial magnetic fields, while Figure 2.24 depicts the volume weighted averaged radial profiles of the magnetic field strength and plasma β. Since β is quite large, these small magnetic fields acts as a passive tracer of the plasma and has little effects on dark matter and gas dynamics.

To further test our code, we also ran a simulation with a relatively large initial magnetic fields. We also included radiative cooling, star formation, and stellar feedback. The radiative cooling models X-ray line and bremsstrahlung emission in a 0.3 solar metallicity plasma. The star formation model turns cold gas into collisionless star particles at a rate $\dot{\rho_{SF}} = \eta_{SF} \frac{\rho_b}{max(\tau_{cool}, \tau_{dyn})}$, where η_{SF} is the star formation ef-

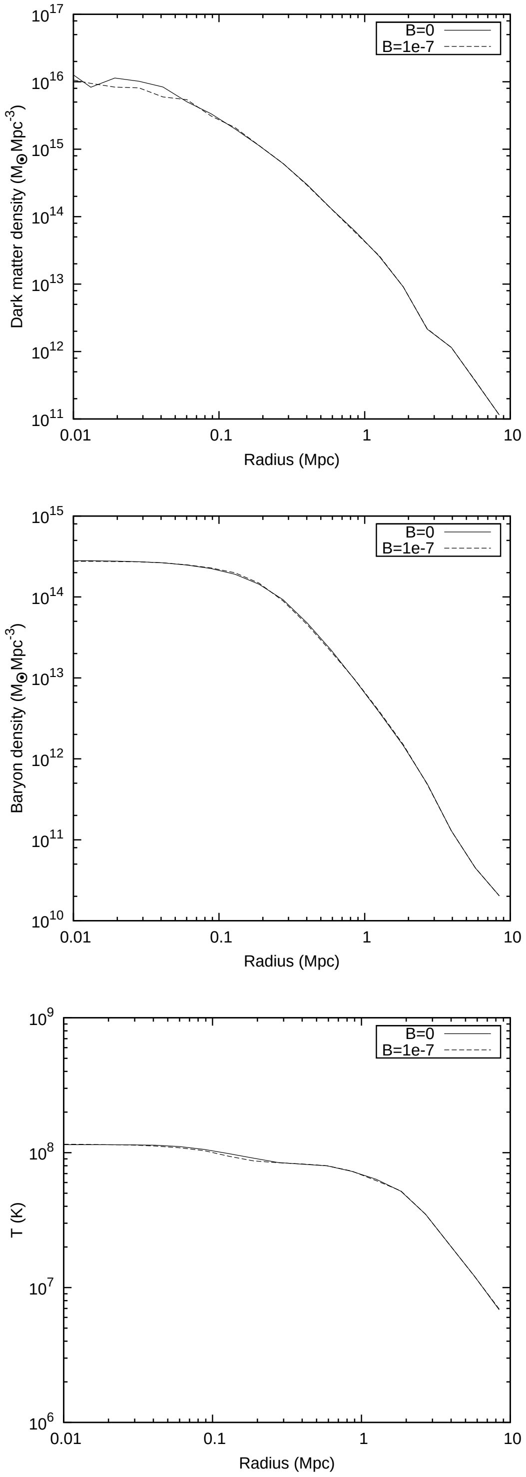

Figure 2.23: Specially averaged radial profiles of dark matter density, baryon density and temperature of MHD simulations with zero and $B_y = 9.72753 \times 10^{-10}$ G initial magnetic fields.

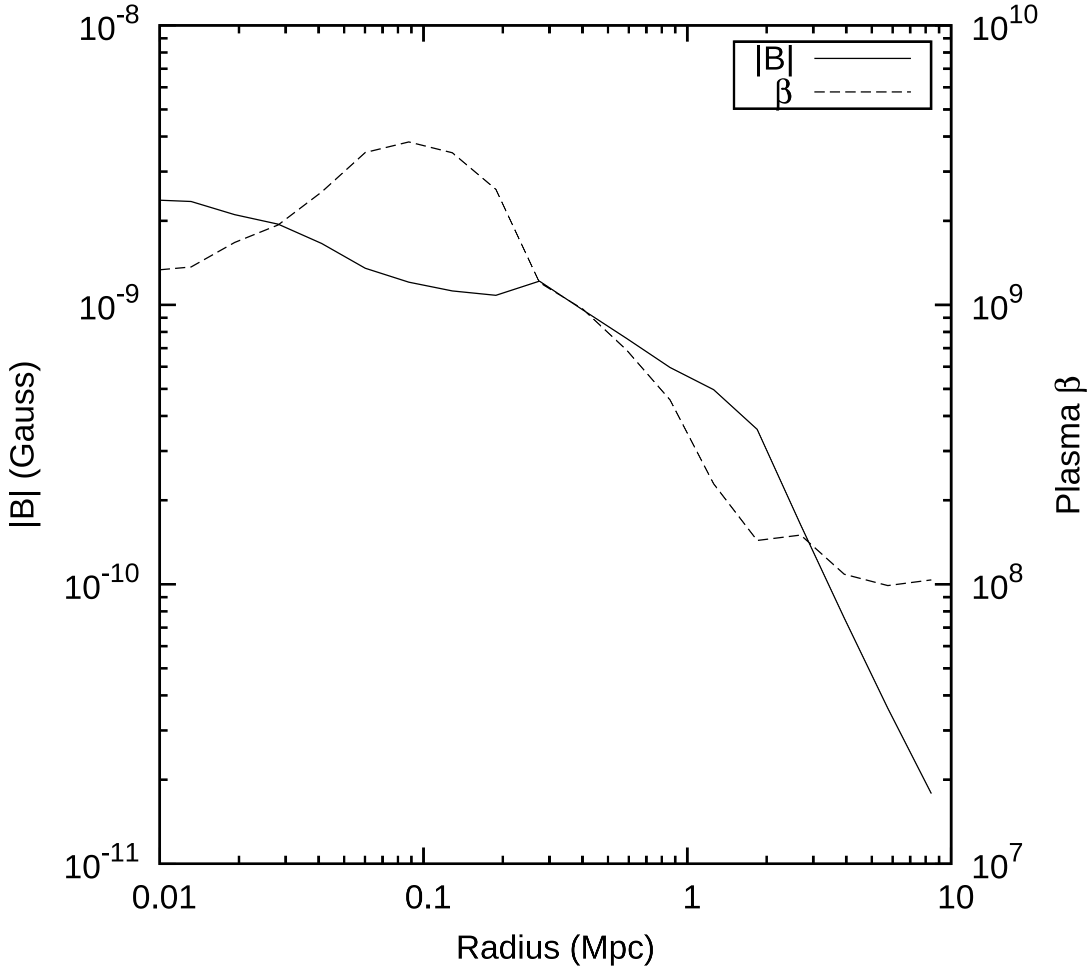

Figure 2.24: Spherically averaged radial profiles of magnetic field strength and plasma β of MHD simulation with $B_y = 9.72753 \times 10^{10}$ G initial magnetic fields.

ficiency factor 0.1, and τ_{cool} and τ_{dyn} are the local cooling time and free fall time, respectively. Stellar feedback returns a fraction of stars' rest energy as thermal energy at a rate $\Gamma_{SF} = \eta_{SN}\dot{\rho}_{SF}c^2$ to the gas. We did two runs, one without initial magnetic fields and the other is with a large initial magnetic fields of $B_y = 1.0 \times 10^{-4}$ in the code unit (9.72753×10^{-7} Gauss). Figure 2.25 shows the radial profiles of gas density and temperature of both runs and the magnetic field strength and the plasma β of the run with magnetic fields.

The magnetic fields reach 20 μG in the core region, a few times larger than the observations (Carilli & Taylor, 2002). In the center where β reaches a minimum, the kinetic energy is a few percent of the thermal energy, as expected from Iapichino & Niemeyer (2008). The magnetic field has become dynamically important in the cluster center. The effect is not significant in the density, as seen in the upper right plot in Figure 2.25, but definitely noticeable in the temperature field, as some of the thermal pressure that was balancing the collapse is replaced by magnetic pressure. In this way, magnetic fields may help to cool cluster cores, giving a better match to observations. Detailed analysis of the magnetic field structure and their influence on the cluster will be presented in forthcoming paper.

2.4 Conclusions

In this chapter, we have introduce EnzoMHD, the MHD version of the AMR cosmology code Enzo before presenting my research done by this code. . EnzoMHD is capable of multi-resolution cosmological and non-cosmological astrophysical simulations using ideal MHD. Enzo uses block structured AMR, which solves they hydrodynamic (and now magnetohydrodynamic) PDEs on fixed resolution patches, and communicates the finest resolution information between coarse and fine patches in way that is conservative in the volume-averaged quantities. This entails 4 basic components: the PDE patch solver, creation of fine grids (interpolation), communication of fine data back to coarse data (projection) and correction of the interface between coarse and fine grids (flux correction). MHD has the additional constraint that the divergence of the magnetic field, $\nabla \cdot \mathbf{B}$, must be zero at all times, which requires

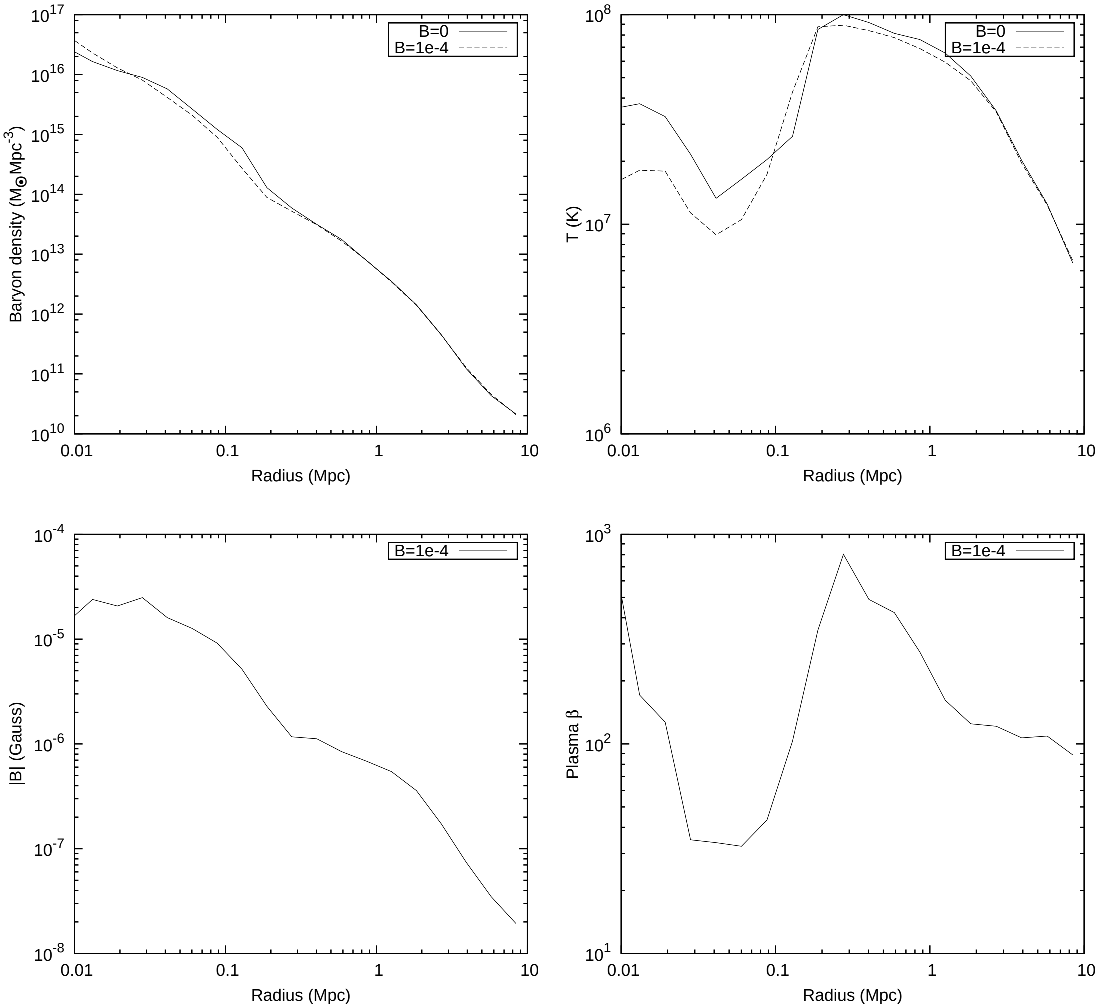

Figure 2.25: Radial profiles of MHD simulations with zero and $B_y = 9.72753 \times 10^{-7}$ G initial magnetic fields with radiative cooling, star formation and stellar feedback.

additional machinery to advance the PDEs (Constrained Transport) and some modifications to the projection and flux correction steps. In addition to multi-resolution hydrodynamics, EnzoMHD includes the effects of gravitational acceleration and cosmological expansion, and a modification to the base PDE solver to account for flows with large disparity between kinetic and thermal energies (dual energy formalism). In EnzoMHD, we use the PDE solver of Li et al. (2008) to solve the ideal MHD equations (Section 2.2.6) for the patch solver, which is second order accurate in both time and space. We use a slightly modified version of the AMR algorithm procedure of Balsara (2001) to create interpolate fine grids and project the more accurate fine grid data to the cheaper coarse grid data (Section 2.2.11 and Appendix A.1). We have used the CT methods of Balsara & Spicer (1999) and Gardiner & Stone (2005) to advance the induction equation while maintaining the constraint $\nabla \cdot \mathbf{B} = 0$(Section 2.2.7). We have operator split the gravitational (Section 2.2.8) and cosmological expansion (Section 2.2.9) terms; and included the entropy-energy technique of Ryu et al. (1993) and the dual energy technique of Bryan et al. (1995).

In Section 2.3, we present the results of a broad array of tests to demonstrate the accuracy of the chosen methods. These include the shock tube of Brio and Wu, on dimensional MHD Caustics, the famous Zel'Dovich Pancake, the Vortex problem of Orzag-Tang, an adiabatic expanding universe. Some of these were additionally run with AMR, and the results compared to the unigrid case. The results of these overall agree with both what's been present in the literature before and comparisons with our existing PPM solver. As an example of the capability and application area of this code, we present some preliminary results from a calculation of galaxy cluster formation with magnetic fields.

In this chapter, we already show the efficiency and accuracy of our AMR MHD cosmology code. In Chapter 3-5, we will discuss simulations performed by EnzoMHD to study the origin and evolution of cluster magnetic fields.

Acknowledgments: This chapter, in part, has been submitted for publication of the material as it may appear in the Astrophysical Journal Supplement Series, 2009. Collins, David C.; Xu, Hao; Norman, Michael L.; Li, Hui; Li, Shengtai, "Cosmological

AMR MHD with Enzo", IOP Publishing, 2009. The dissertation author was the primary investigator and author of this paper.

Chapter 3

The Biermann Battery Effect in Large Scale Structure Formation

3.1 The Biermann Battery Effect

The problem of generating magnetic fields from zero field is intertesting. The induction equation in the idea MHD approximation is,

$$\frac{\partial \mathbf{B}}{\partial t} = \nabla \times (\mathbf{v} \times \mathbf{B}) \tag{3.1}$$

so no magnetic fields can be created if the initial fields are zero. But this MHD approximation breaks down once considering the charge separation effect due to the difference in mobility between electrons and ions. In this section, we will first discuss magnetic field creation by so-called Biermann Battery effect based on the charge separation.

The induction equation is derived from Ohm's law, keeping the electron pressure term in the general form of Ohm's law (Kulsrud, 2005):

$$\mathbf{E} + \frac{\mathbf{v} \times \mathbf{B}}{c} = -\frac{\nabla p_e}{n_e e} \tag{3.2}$$

p_e is electron pressure and n_e is electron number density. Take the curl of this equation and get the modified induction equation:

$$\begin{aligned}\frac{\partial \mathbf{B}}{\partial t} &= \nabla \times (\mathbf{v} \times \mathbf{B}) + \nabla \times (\frac{c\nabla p_e}{n_e e}) \\ &= \nabla \times (\mathbf{v} \times \mathbf{B}) - c\frac{\nabla n_e \times \nabla p_e}{n_e^2 e} \qquad (3.3)\end{aligned}$$

The second term on the right hand side is called the Biermann Battery term. Once this term is not equal to zero, magnetic fields will be created.

To rewrite this equation in terms of total pressure p and density ρ, we set $n_e = n_i = \chi(n_e + n_n)$, where n_i and n_n are the ion number density and neutral number density, respectively. χ is ionization fraction and is assumed to be constant in space. In the case temperature of the ions and electrons is the same as the temperature of the neutrals,

$$p_e = \frac{n_e}{n_e + n_i + n_n} p = \frac{\chi}{(1+\chi)} p \qquad (3.4)$$

$$n_e = \chi(n_i + n_n) = \frac{\chi \rho}{M} \qquad (3.5)$$

where M is the average mass per neutral and also assumed unchanged in space. Substituting into Equation 3.3, we get,

$$\begin{aligned}\frac{\partial \mathbf{B}}{\partial t} &= \nabla \times (\mathbf{v} \times \mathbf{B}) + \frac{cM}{e(1+\chi)} \nabla \times (\frac{\nabla p}{\rho}) \\ &= \nabla \times (\mathbf{v} \times \mathbf{B}) - \frac{cM}{e(1+\chi)} \frac{\nabla \rho \times \nabla p}{\rho^2} \qquad (3.6)\end{aligned}$$

This is the modified induction equation we will use in the simulations. This equation maintains the divergence free constraint of magnetic fields since the source term is a curl of a function.

It is interesting to compare this equation with the fluid vorticity ($\boldsymbol{\omega} = \nabla \times \mathbf{v}$) equation (Kulsrud et al., 1997):

$$\frac{\partial \boldsymbol{\omega}}{\partial t} = \nabla \times (\mathbf{v} \times \boldsymbol{\omega}) + \frac{\nabla \rho \times \nabla p}{\rho^2} \qquad (3.7)$$

here the viscous term is neglected. The source terms of magnetic fields and vorticities are identical except for a factor, so the magnetic fields are generated at the same places where vorticity is generated.

For a barotropic flow, the Biermann Battery term is always zero. That is because the pressure is only dependent on the density, then the gradients of density and pressure are parallel to each other and their cross product is zero. But it is generally nonzero in regions where shocks are present, so magnetic fields will be created within shocks during large-scale structure formation.

Kulsrud et al. (1997) performed cosmology simulations to study magnetic field generations from Biermann Battery effect. They evolved magnetic fields passively in their hydrodynamics code (Ryu et al., 1993) with an additional induction equation (Equation 3.6). They simulated a standard CDM model of a box of (32 h^{-1} Mpc)^3, using 128^3 cells and 64^3 particles for dark matter, from z=20 to z=0. Magnetic fields of strength of order 10^{-21} G were found in their simulations at z∼2-3. However, their spatial resolution was too large for the scale of interest.

We present two simulations in this chapter both with Biermann Battery effect. One is the Population III star formation and the other is the galaxy cluster formation. Higher resolutions in our simulations may help to better understand the magnetic field generations from the battery effect and their subsequent evolution.

3.2 The Biermann Battery Effect in the Population III Star Formation

3.2.1 Introduction

In this section, we study the magnetic fields created by Biermann Battery effect in the first generation of stars. The magnetic fields originating from Biermann Battery effect are the minimum possible fields in existence during Population III star formation, and may be the seed fields for stellar dynamo or for the magnetorotational instability in accretion disks around the first stars.

The nature of the first generation of stars, as well as their influence on later structure formation, is a fundamental problem in cosmology. A great deal of theoretical progress has been made (see recent reviews by Bromm & Larson, 2004; Glover, 2005; Ciardi & Ferrara, 2005). In the past decade, cosmological hydrodynamic simulations of Population III star formation have achieved great success, and significantly different numerical methods have produced results that agree quite well (Abel et al., 2002; Bromm et al., 2002; Yoshida et al., 2003; O'Shea & Norman, 2007). These calculations have given a reasonably clear picture of the formation process of Population III stars, and have provided some constraints on many of their important properties.

These calculations, while useful, largely ignore an important issue: the relevance of magnetic fields in Population III star formation. Magnetic fields are widely observed in our galaxy, in other galaxies, and in galaxy clusters, and the origin of these fields is one of the most fundamental and challenging problems in astrophysics (Carilli & Taylor, 2002; Widrow, 2002). One possibility is that magnetic fields are created and amplified in the first generation of stars and are spread throughout the IGM when these stars explode, providing seed fields for later generations of stars and for further amplification by dynamo effects. If some seed magnetic fields exist before Population III stars form, they may help to remove angular momentum from the star-forming clouds, significantly changing the ultimate mass range of these stars (Pudritz & Silk, 1989; Davies & Widrow, 2000).

Several groups have examined the importance of magnetic fields on the evolution of Population III protostellar disks using analytic or semi-analytic models. These include Silk & Langer (2006), Tan & McKee (2004) and Tan & Blackman (2004), who model (among other aspects of primordial star formation and evolution) dynamos in primordial accretion disks. Other authors, including Flower & Pineau des Forêts (2003) and Maki & Susa (2007), use one-dimensional calculations to examine the collapse of the primordial star-forming cloud and the assumptions of flux-freezing. More recent work (Machida et al., 2006, 2008) follows the 3-D evolution of an idealized primordial cloud core. Although useful, none of these models self-consistently include the effects of both magnetic fields and cosmological structure formation.

Here, We present the results of the first self-consistent three-dimensional adaptive mesh refinement magnetohydrodynamic simulations of Population III star formation including the Biermann Battery effect within the context of cosmological structure formation.

3.2.2 Methodology

The simulation setup is similar to that described in O'Shea & Norman (2007). We use a N-body plus hydrodynamics simulation with a comoving box size of 0.3 h^{-1} Mpc, initialized at $z = 99$ with an Eisenstein & Hu power spectrum (Eisenstein & Hu, 1999), and with cosmological parameters $\Omega_b = 0.04$, $\Omega_m = 0.3$, $\Omega_\Lambda = 0.7$, $h = 0.7$, $\sigma_8 = 0.9$, and $n_s = 1.0$. The simulation was first run with a 128^3 root grid and three levels of AMR to $z = 15$, where the most massive halo in the volume was found. The simulation was then re-centered on this halo, using a 128^3 root grid and three levels of static nested grids, giving a dark matter and baryon resolution of 1.81 h^{-1} $M_\odot$ and 0.28 h^{-1} $M_\odot$, respectively, and an initial comoving spatial resolution of 293 h^{-1} pc. The simulation was started at $z = 99$, initialized with zero magnetic fields throughout, and allowed to run with a maximum of 22 levels of adaptive mesh refinement until the collapse of the most massive halo, at $z \simeq 17.55$, using the nine-species molecular chemistry of Abel et al. (1997) and Anninos et al. (1997), but modified for high densities as described in Abel et al. (2002). Further details of the simulation setup and physics can be found in O'Shea & Norman (2007).

The electron fraction is always small during PopIII star formation. But as pointed out by Kulsrud et al. (1997) (See Equation 3.6), the ionization fraction enters into the induction equation through $1 + \chi$, so even a very small ionization fraction is enough to generate magnetic fields. In our simulation, we took $m = 1.2\ m_H$, where m_H is the mass of a neutral hydrogen atom. The electron fraction is $\ll 1$ at all times in this star formation scenario, so we set $\chi = 0$ rather than calculating the electron fraction in every cell. Given the approximation above, this introduces negligible error. The battery term is added to the simulation through the EMF term in the constrained transport algorithm, ensuring that no divergence of magnetic fields is introduced to the system.

Since the electron fraction declines rapidly at the halo core, ambipolar diffusion may be important in star formation simulation (Abel et al., 2002). To address this issue, we compared the ambipolar diffusion timescale with the dynamic timescale in our simulation, as in O'Shea & Norman (2007). The ratio is always larger than 10 over the density range of interest, suggesting that ambipolar diffusion does not play a significant role up to the densities that we study.

3.2.3 Results

Over the course of the simulation, magnetic fields are produced at various physical scales by the Biermann Battery process. We first plot the distributions of gas density and magnetic fields in z direction in a slice through the halo core at z=20 and z=17.55 (the last output) to show the magnetic field distribution at the star forming-halo in Figure 3.1. At z=20, the core of radius about 10 pc contains several hundred $M_{\odot}$ baryon with number density of about 10 cm^{-3}. The magnetic fields inside the core at the level of $10^{-15}G$ with scale length about ten pc. At z=17.55, the core density increases to $10^{10}cm^{-3}$ in the central 0.01pc region through rapid collapse. Then the magnetic fields "frozen-in" the gas increase to 10^{-10} G level.

Figure 3.2 shows the evolution of spherically-averaged radial profiles of the baryon number density and magnetic field strength of the primordial star-forming halo at several times during the halo evolution. Since the magnetic fields are very small ($\beta \equiv P_{thermal}/P_{magnetic}$ is greater than 10^{15} at all times), the gas collapse at the halo core is almost the same as the hydrodynamic ($B = 0$) case described by O'Shea & Norman (2007). The profiles start at $z = 40$, where the magnetic fields generated by the Biermann Battery are of order 10^{-18} G, which is consistent with theoretical predictions (Pudritz & Silk, 1989; Davies & Widrow, 2000). In plasmas with a large beta ($\gg 1$) and large mass-to-flux ratio, magnetic fields follow the gas falling into the core passively, so after being generated at low densities, the magnetic fields are primarily amplified by being carried along with collapsing baryons. This is shown more clearly in Figure 3.3, and will be discussed in more detail later. At low density (up to $\mathrm{n}_b \simeq 2$ cm^{-3}, corresponding to the evolution of the gas up to $z \sim 20$), the Biermann Battery is effective at creating magnetic fields. The central magnetic field scales with density as $|B| \propto \rho$, suggesting that the magnetic field is enhanced by both the Biermann Battery effect and by gas collapse. At higher densities (after $z \simeq 20$), the magnetic field at the center of the halo is amplified as $|B| \propto \rho^{2/3}$, as expected in spherical collapse. At later times, when the gas in the center of the halo collapses, the magnetic field in the center of the halo rises to $\sim 10^{-9}$ G as the central

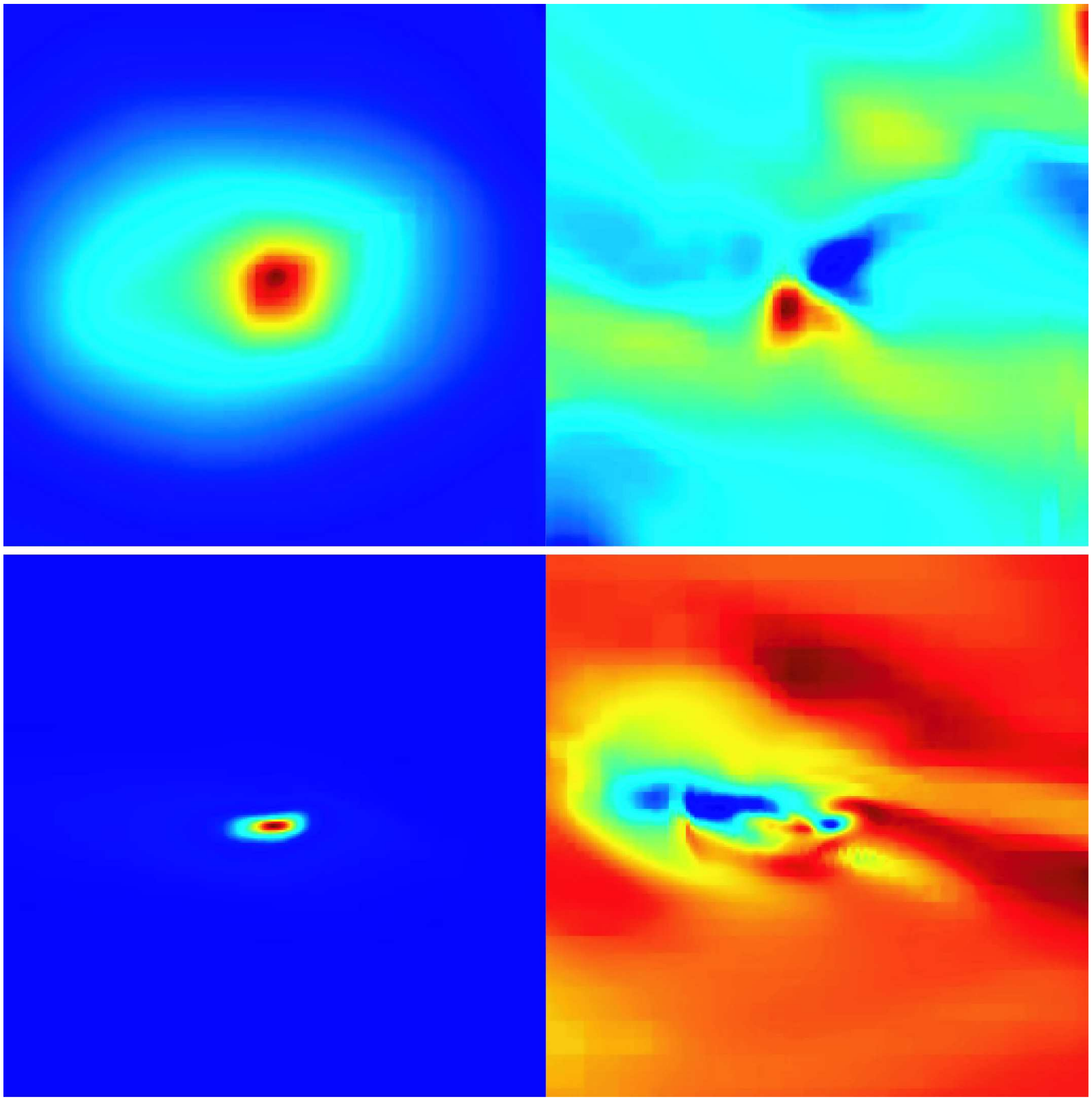

Figure 3.1: Images of gas density (left) and magnetic fields in z-direction (right) at a slice cutting the halo core at $z = 20$ (top) and $z = 17.55$ (bottom). The view is 40 pc for z=20 and 0.044 pc for z=17.55. For z=20, The density is from 1.1 to 12.7 cm^{-3}. The range of B_z is -1.3×10^{-15} to 2.1×10^{-15} G. For z=17.55, the density is from 4.7×10^6 to 1.2×10^{10} cm^{-3}. The range of B_z is -2.4×10^{-10} to 5.6×10^{-11} G. In all panels red represents high and blue represents low, with the color table relative in each plot.

number density grows to $n_b \simeq 10^{10}$ cm^{-3}.

It is useful to examine the history of magnetic field amplification inside the halo in more detail. This is shown in Figure 3.3, which shows the mass- and volume-weighted magnetic fields inside the halo virial radius as a function of redshift (top panel), and also shows the mass-weighted mean magnetic field strength in the inner 100 $M_\odot$ of gas as a function of the mass-weighted baryon number density of gas in the same Lagrangian region (bottom panel). From these two plots, the two stages of magnetic field amplification can be observed. From $z = 40$ to $z = 20$, the magnetic fields slowly increase to 10^{-15} G. At this stage, the mass-weighted and volume-weighted fields are quite similar, because the magnetic fields are created and amplified by the Biermann Battery at large spatial scales, and the fields are distributed uniformly by mergers and shear flows (see Roettiger et al. (1999)). During the second stage of evolution, after $z = 20$, the volume-weighted and mass-weighted fields evolve in very different ways, with the mass-weighted magnetic field growing rapidly along with the increasing baryon density in the halo cores.

The bottom panel of Figure 3.3 shows that at late times (high densities), the magnetic field in the core of the halo increases as $|B| \propto \rho^{2/3}$, or solely from field amplification due to magnetic fields frozen into spherically-contracting gas. The collapse timescale at the center of the halo is proportional to the cooling time, which is quite short at high densities, making any significant magnetic field creation by the Biermann Battery mechanism difficult in the halo center. The baryon density in the halo core grows about 9 orders of magnitude (from 1 to 10^{10} cm^{-3} between $z = 20$ and $z = 17.55$, when the simulation is terminated), and the magnetic fields in the core increase by about 5 orders of magnitude (from 10^{-15} to 10^{-9} G). Though the core region contains less than one percent of the halo gas, the mass-weighted magnetic field in the halo increases by approximately four orders of magnitude, from $\sim 10^{-15}$ to 10^{-11} G, between z=20 and z=17.55.

To show where magnetic field generation via the Biermann Battery takes place, and to provide a more quantitative understanding of its effect in different stages of halo evolution, we show in Figure 3.4 the two-dimensional distribution of the instantaneous magnetic field generation rate via the Biermann Battery versus baryon

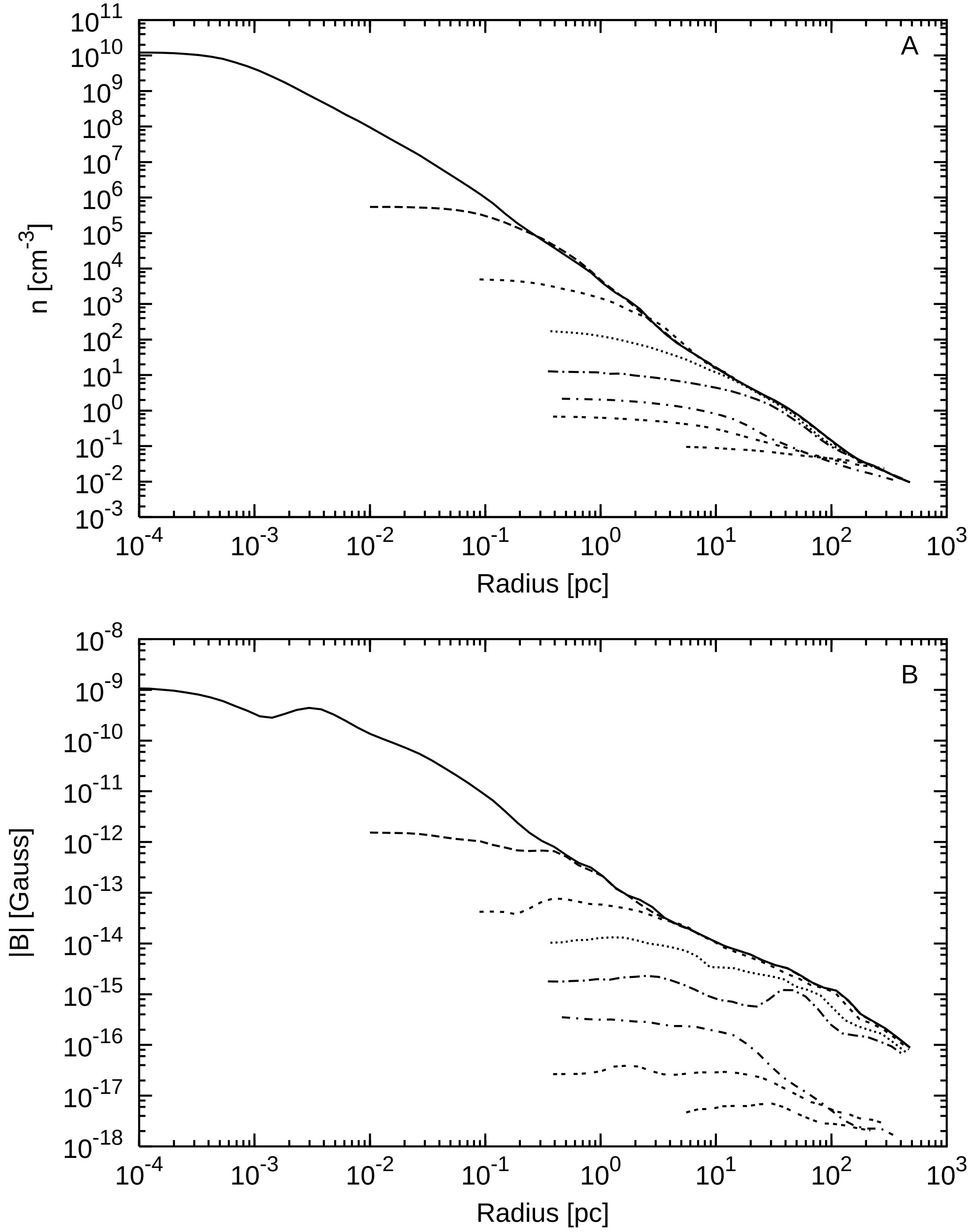

Figure 3.2: Evolution of spherically-averaged radial profiles of baryon number density (top) and magnetic field strength (bottom) of the Population III star-forming halo. Lines correspond to (from bottom to top in each panel) $z = 40, 30, 25, 20, 19, 18, 17.61, 17.55$.

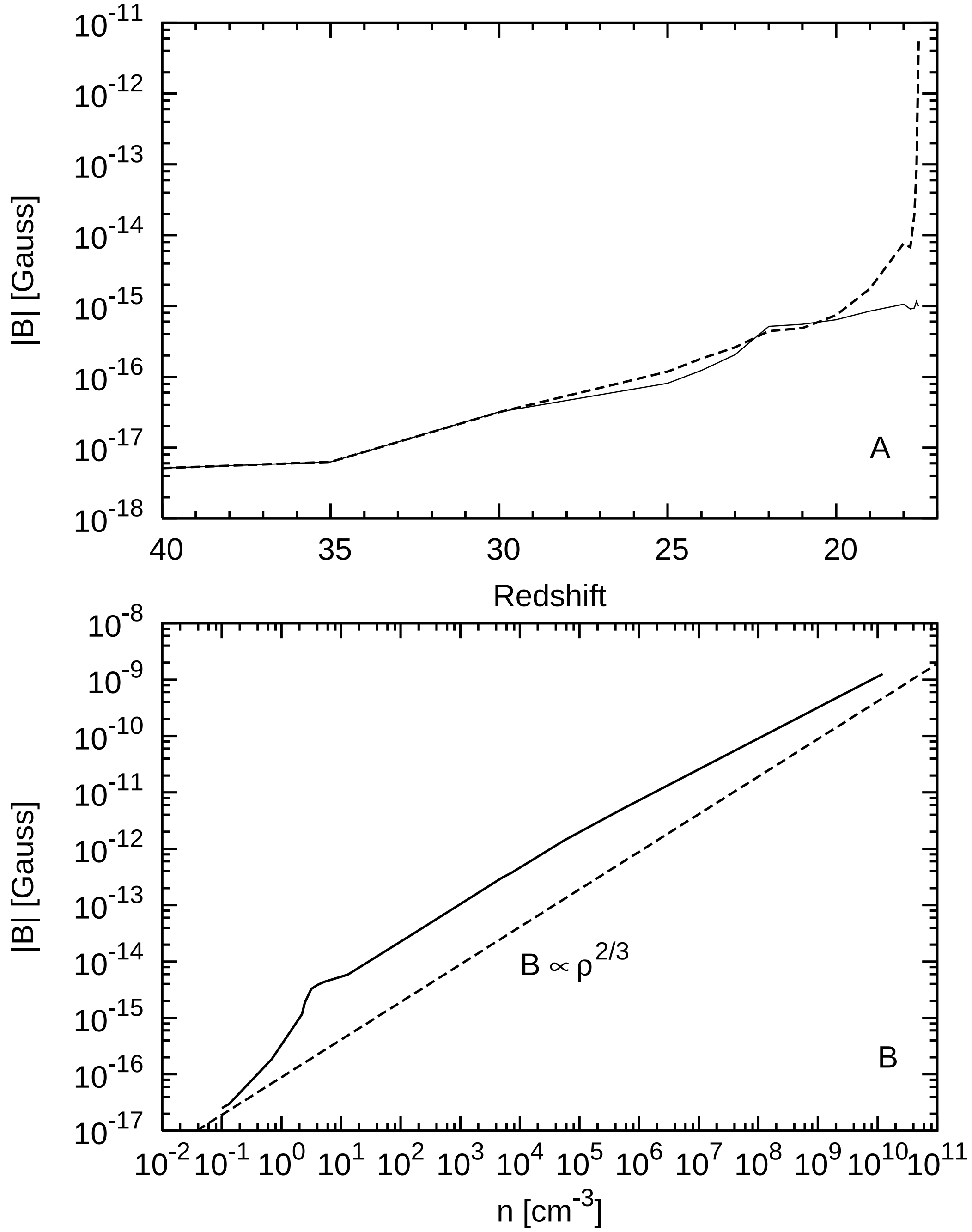

Figure 3.3: Top panel: mass-weighted (dashed line) and volume-weighted (solid line) mean magnetic field strength inside the virial radius of the collapsing halo as a function of redshift. Bottom panel: mass-weighted mean magnetic field strength as a function of baryon number density inside the core of the primordial star forming halo at the final simulation output (solid line; $M_{enc} \simeq 100\ M_{\odot}$). The dashed line shows $|B| \propto \rho^{2/3}$ (as expected by flux freezing and spherical collapse).

overdensity at four simulation outputs from $z = 40$ to $z = 17.55$. At early times, very little gas is at high overdensities, and the magnetic field generation rate is below 10^{-35} G/s. The total time taken during the simulation, from $z = 99$ to $z = 17.55$, is approximately 6.2×10^{15} seconds. If the magnetic fields are only created by the Biermann Battery without any amplification from shear flows or collapse, the magnetic fields would be at most 10^{-19} G at $z \sim 18$. By $z = 40$ ($\sim 1.5 \times 10^{15}$ seconds, or 5×10^7 years, after the beginning of the calculation), fields reach a strength of 10^{-18} G, suggesting that some amplification is taking place through gas collapse. While the rate of magnetic field generation via the Biermann Battery can actually be much higher at high overdensity (as seen in the bottom right panel, at $z = 17.55$), the rate never exceeds 10^{-25} G/s ($\sim 3 \times 10^{-18}$ G/yr). Given that the collapse of the core, from a peak baryon density of $\mathrm{n}_b \sim 1$ cm^{-3} to 10^{10} cm^{-3}, takes approximately 10^{14} seconds ($\simeq 3 \times 10^6$ years), magnetic fields larger than 10^{-12} G cannot be made with the Biermann Battery alone during this time, strongly suggesting that the battery effect makes little contribution to magnetic field amplification during the final collapse.

3.2.4 Discussion and Conclusions

In this section, we have shown results from the first cosmological magnetohydrodynamical simulation of Population III star formation including the Biermann Battery effect. This effect is one of the most robust methods of generating magnetic fields in the Universe (Biermann, 1950), and thus provides useful constraints on the minimum magnetic field expected in situations where Population III star formation will take place.

We find from our simulation that small magnetic fields are primarily generated via the Biermann Battery at relatively low overdensities, and are then amplified to values of nearly 10^{-9} G at the center of the cosmological halo via gravitational collapse. While significant, this magnetic field is still quite small – the plasma β is never smaller than 10^{15} at any point during the simulation. This suggests strongly that the magnetic fields do not play a significant dynamical role up to densities of $\mathrm{n}_B \sim 10^{10}$ cm^{-3}, when the simulation is terminated. As a result, up to that

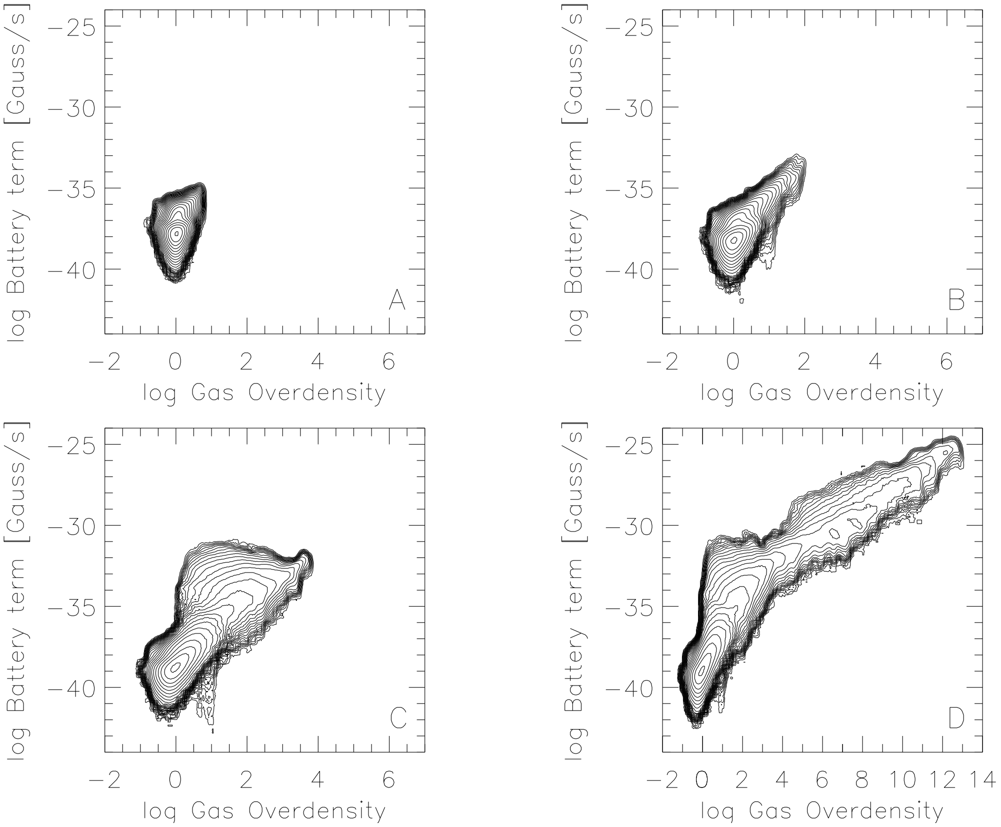

Figure 3.4: Mass-weighted two-dimensional distributions of the instantaneous rate of magnetic field generation via the Biermann Battery vs. baryon overdensity, at $z = 40$ (top left), $z = 30$ (top right), $z = 20$ (bottom left) and $z = 17.55$ (bottom right). Each panel includes all gas in the simulation volume at a given redshift. Contour lines are logarithmic, and show relative values between the highest and lowest non-zero values in each panel.

point the evolution of the primordial gas within the cosmological halo is very close to the hydrodynamic results obtained by O'Shea & Norman (2007). This result lends credibility to assumptions regarding the dynamical insignificance of magnetic fields made in previous cosmological calculations of Population III star formation. At higher densities than are explored in these types of calculations, however, the magnetic fields may be amplified to dynamically relevant values via a process such as the magnetorotational instability or a dynamo (Silk & Langer, 2006; Tan & McKee, 2004; Tan & Blackman, 2004).

Comparison to previous work is somewhat difficult, since we start out with no magnetic field and terminate our calculation at $n_B \sim 10^{10}$ cm^{-3}. The work done by Silk & Langer (2006), Tan & McKee (2004) and Tan & Blackman (2004) focus on disk physics at much higher densities than are explored in this simulation. Maki & Susa (2007) and Flower & Pineau des Forêts (2003) focus on ambipolar diffusion – physics not present in our calculations, which assume the equations of ideal MHD. Additionally, while their initial conditions start within the density regime probed by our calculations, both sets of models assume the presence of much stronger magnetic fields than are generated by our calculations. We can, however, directly compare our work to that of Machida et al. (2006, 2008), who study fragmentation and jets in magnetized, rotating primordial clouds. They find that protostellar jets are formed when their clouds have a magnetic field of $B_0 > 10^{-9}$ $(n_H/10^3 \text{ cm}^{-3})^{2/3}$ G and with rotational energy that is greater than the magnetic energy. These conditions are not both satisfied in the halo modeled in our calculation, suggesting that in the absence of a pre-existing magnetic field or a mechanism for generating larger fields at higher densities, strong protostellar jets may not exist in this halo. This does not preclude such jets being formed in halos of a significantly different mass or evolutionary history.

The simulation of the evolution of an evolving protostellar core within an accretion disk is currently beyond the capability of our numerical tools. However, there are multiple avenues that we can follow to more thoroughly explore the relevance of magnetic fields in Population III star formation. We can begin our calculation with seed fields having strengths based on limits from observation and theory (Widrow, 2002). We can also examine the effects of magnetic fields at higher densities by implementing more chemical and cooling processes (as discussed by Turk et al., 2008). Both of these projects are underway, and we will report on the results in an upcoming paper.

To summarize, we have performed the first calculations that incorporate the Biermann Battery in cosmological magnetohydrodynamic simulations of Population III star formation. Our key results are as follows:

1. From an initial state with no magnetic fields, a combination of the Biermann Battery and compressional amplification can result in fields with strengths of $|B| \simeq 10^{-9}$ G at $\mathrm{n}_B \simeq 10^{10}$ cm^{-3} at the center of a cosmological halo where a Population III star will form.

2. The Biermann Battery creates fields predominantly at low density ($\mathrm{n}_B \leq 10$ cm^{-3}) and large spatial scales in Population III star-forming halos.

3. The magnetic fields created by the Biermann Battery are dynamically unimportant at all densities below $\mathrm{n}_B \simeq 10^{10}$ cm^{-3} – $\beta \equiv P_{th}/P_B \geq 10^{15}$ at all times during the evolution of the halo.

3.3 The Biermann Battery Effect in the Formation of Galaxy Cluster

3.3.1 Introduction

In this section, we present simulation of magnetic field creations and amplifications in galaxy cluster formation with Biermann Battery effect. The nature of the simulation is similar to the pioneering study by (Kulsrud et al., 1997), but now we have much better spatial resolution with AMR. It isn't expected that the tiny magnetic fields from battery effect will be amplified to the level of being important in any physical processes. But it is interesting to study how magnetic fields are generated, and more importantly, are amplified in sub-cluster scale. This simulation is a supplement to the study in the Chapter 5. Here, the magnetic fields are so weak that they will never be dynamically important and never be saturated in sense of energy equipartition between magnetic energy and kinetic energy in any regions. We will describe the simulation and major results in this chapter with a concise discussion, most of discussions about magnetic field evolution in galaxy cluster will be left to the Chapter 5.

3.3.2 Methodology

The simulation uses a ΛCDM model with parameters $h = 0.73$, $\Omega_m = 0.27$, $\Omega_b = 0.044$, $\Omega_\Lambda = 0.73$, and $\sigma_8 = 0.77$, the values are from WMAP III results (Spergel et al., 2007). For simplicity, the simulation is adiabatic without the additional physics such as radiative cooling, star formation and supernova feedback, while these processes are not essential for the purpose of this study. The survey volume is 256 h^{-1} Mpc on a side. The simulation is computed from cosmological initial conditions sampled onto a 128^3 root grid and 2 level nested static grids in the Lagrangian region where the cluster forms which gives an effective root grid resolution of 512^3 cells (0.5 Mpc) and dark matter particles of mass $1.07 \times 10^{10} M_\odot$. AMR is used only in the region (about (50 Mpc)^3) where the galaxy cluster forms, with a total of 8 levels of refinement beyond the root grid allowed, for a maximum spatial resolution of 7.8125 h^{-1} kpc. While the baryons are resolved at higher and higher spatial and mass resolution at higher levels, the dark matter particles remain constant in mass so as not to add any additional noise. The simulation is evolved from redshift $z = 30$ to $z = 0$ with the Biermann Battery term is always turn on. In this run, M is 1.0 m_H, and χ equals 1. This latter assumption is justified because the intergalactic medium out of which the cluster forms is highly ionized.

The Biermann Battery term is added to the simulation the same way as the run of Population III star formation. But a new refinement criteria was used in this simulation. To maintain a high resolution in a relative large region in the cluster, all the regions with density 200 times larger than critical density are refined to the highest level. So for z<1, while the cluster is well formed, roughly, a sphere with radius of 1.5 Mpc comoving, or 150 cells in highest resolution, is refined to the highest level.

3.3.3 Results

During the simulation, the magnetic fields are first created by the Biermann Battery effect at a large range of scales. Figure 3.5 shows the slice cuts perpendicular to y axis across the center of cluster at z=3 of gas density, temperature, magnetic energy density and strength of the Biermann Battery term. Each plot covers an area of 40 × 40 Mpc comoving (or 10 × 10 Mpc proper). This frame is at $\sim$ 900 Myr after simulation start. At this time, a proto-cluster of radius of about 0.20 Mpc is already formed, while the gas is heated to 10^7 K by the shocks. The magnetic fields are about 10^{-20} G within the proto-cluster and about 2 order of magnitude smaller in the filaments. It is a clear trend that the magnetic fields from the Biermann Battery mechanism is larger in hotter regions, which usually have larger vorticity generated by accretion shocks (Ryu et al., 2008). The magnetic field generation rate is $\sim 10^{-36}$ G s^{-1} at most. So the magnetic fields from battery effect shouldn't be larger than 10^{-22} G without any amplifications. The proper density of baryon in the cluster center increases about 1000 from simulation start, so the magnetic fields there may increase another 100 times to 10^{-20} G by collapse since $|B| \propto \rho^{2/3}$. The magnetic fields in the core region are bigger than that, so it means that some process (likely to be stretching by shear flows) other than collase also amplifies the magnetic fields. Figure 3.6 are the images of gas density and battery source term of cuts through cluster centers at z=2, 1, and 0. There is no obvious evolution in the generation rate of magnetic fields by the Biermann Battery effect. The created fields are distributed at large spatial scales and even at low density regions out of cluster. The source term of magnetic fields is hardly larger than 10^{-35} G s^{-1}. For the Hubble time 13 billion years (4×10^{17} s), the magnetic fields from battery effect only should be at most 10^{-18} G.

Figure 3.7 shows the evolution of magnetic fields by plotting the projections of gas density and magnetic energy density along y axis at different redshifts. The magnetic fields are frozen in the plasmas and concentrate at the cluster region during the hierarchy structure formation of cluster.

Figure 3.8 shows the total magnetic energy and the magnetic energy per unit mass inside half of the virial radius as function of time from z=3, while figure 3.9 plots the

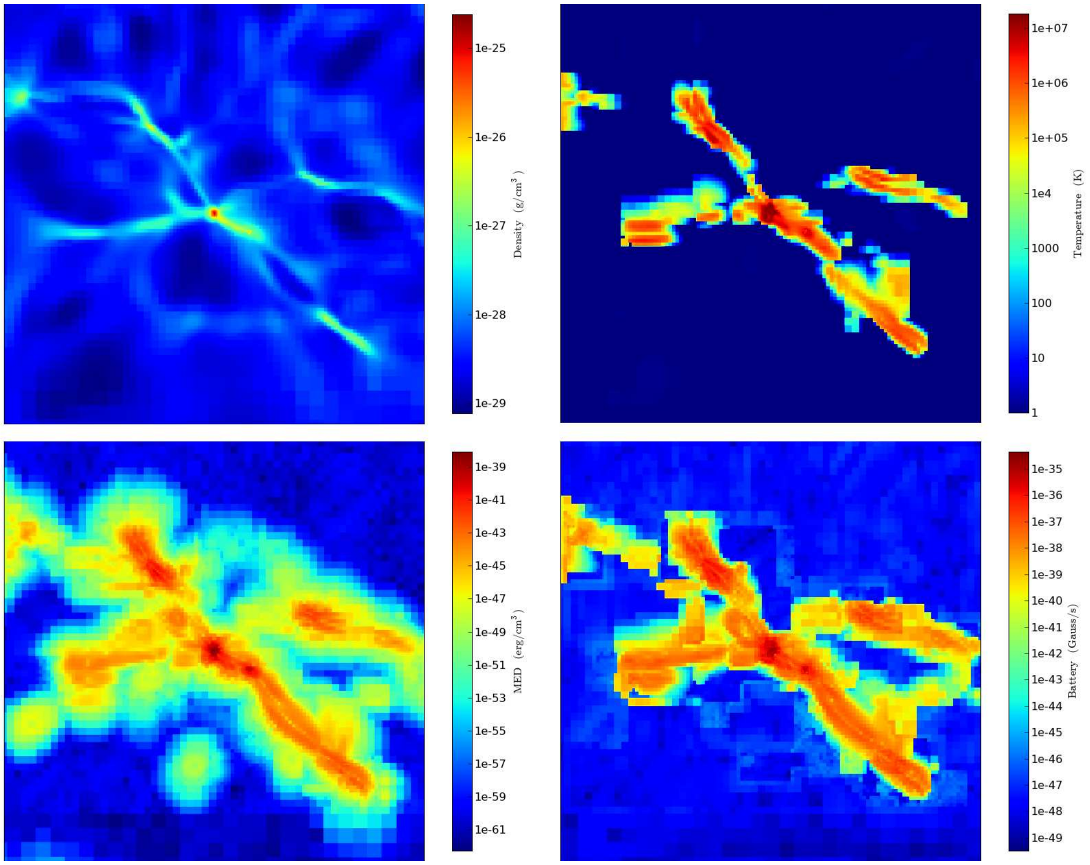

Figure 3.5: Images of gas density, temperature, magnetic energy density and strength of the Biermann Battery term at z=3. Size of each image is 40 × 40 Mpc comoving.

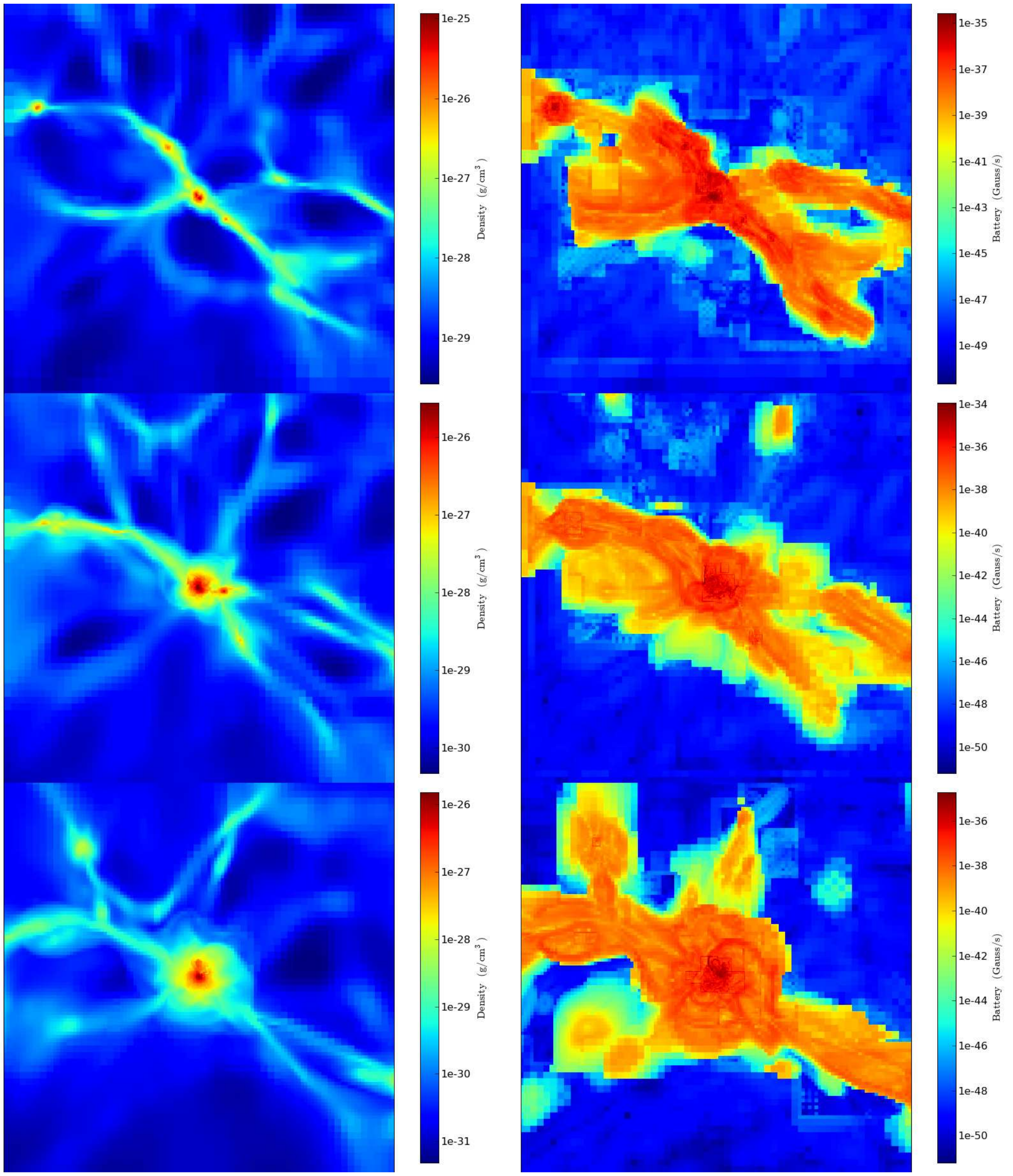

Figure 3.6: Images of gas density and strength of the Biermann Battery term at z=2, 1, 0. Each image covers 40 × 40 Mpc comoving.

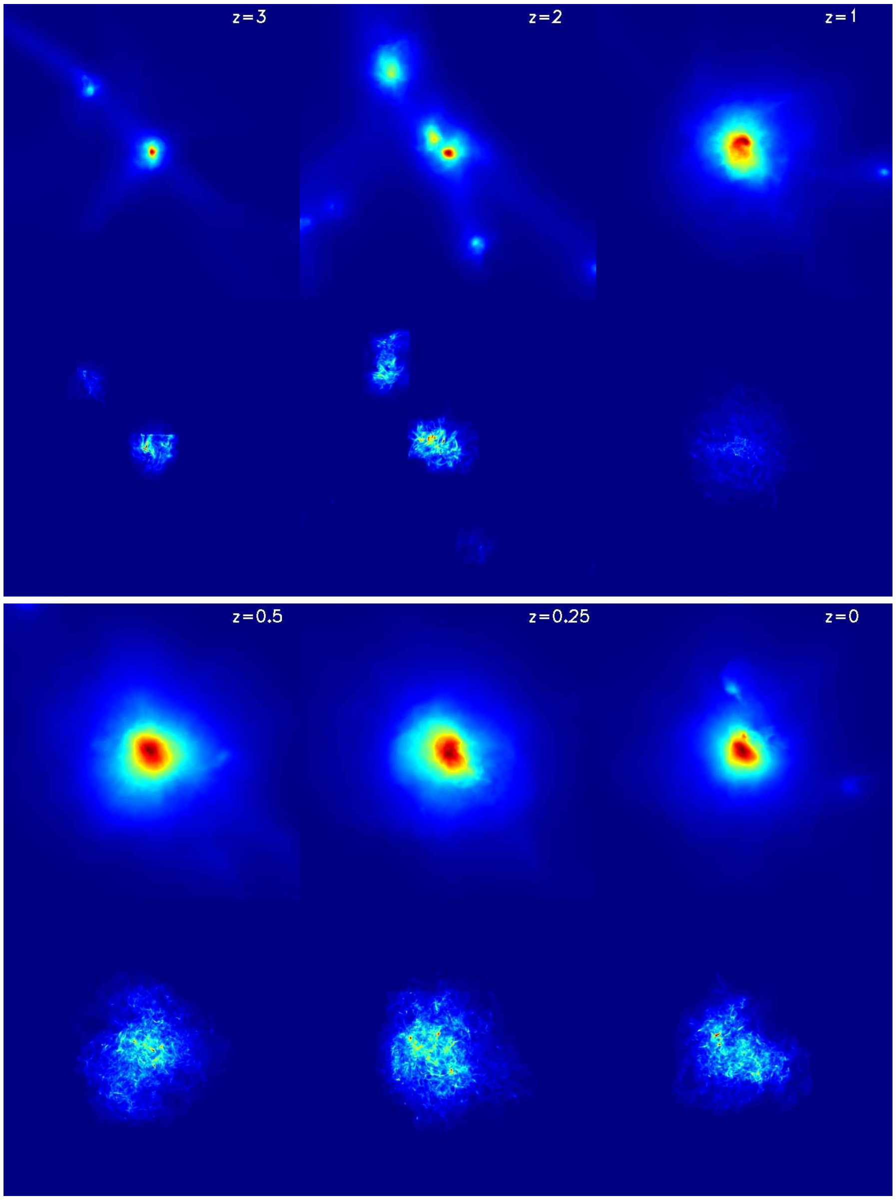

Figure 3.7: Snapshots of projected gas density and magnetic energy density at different redshifts. Each plot is 4 h^{-1} Mpc comoving on the size. Projection is alone the y-axis for 4 h^{-1} Mpc comoving. The ranges of projected gas density are, from high redshift to low redshift, 1.11×10^{-4} - 4.14×10^{-2} , 3.49×10^{-5} - 2.96×10^{-2}, 5.54×10^{-5} - 3.96×10^{-2}, 4.15×10^{-5} - 2.15×10^{-2}, 4.73×10^{-5} - 2.01×10^{-2}, and 5.43×10^{-5} - 2.22×10^{-2} g cm^{-2}, respectively. The ranges of magnetic energy density (averaged over projected distance) are 2.89×10^{-46} - 4.20×10^{-35}, 1.32×10^{-44} - 4.07×10^{-35}, 4.02×10^{-41} - 1.13×10^{-33}, 2.07×10^{-39} - 1.88×10^{-33}, 7.94×10^{-40} - 2.20×10^{-33}, and 1.13×10^{-39} - 3.88×10^{-33} ergs cm^{-3}, respectively.

evolution of baryon mass inside the same volumes. For the first 1 Gyr after z=3, the central proto-cluster is relatively relaxed until the merger happens around z=2, so all these quantities have little changes. During this period, some plasmas as well as magnetic fields flow into the proto-cluster but the magnetic fields inside the cluster aren't amplified much. From z=2 to 1, the cluster undergoes numerous mergers and continuous mass accretion (see Figures 3.7 and 3.9), so the cluster becomes much more active. Then both the magnetic energy and the magnetic energy density experience exponential growth with constant rates from t=1 Gyr (z $\sim$ 2) to t=6 Gyr (z $\sim$ 0.5), then continue to grow at slower rates until simulation end. It seems that the cluster motions are still vigorous enough to amplify magnetic fields after z=1 when the mass accretion process already slows down dramatically. Further research is needed to understand the relation of the magnetic field amplifications and the ICM motions. The magnetic energy and the magnetic energy per unit mass jump $\sim$ 40000 and $\sim$ 500 times from z=3 to 0, respectively, while the gas mass inside the sphere increases only $\sim$ 80 times.

The spherically averaged radial profiles of gas density and magnetic field strength at different redshifts are showed at Figure 3.10. The magnetic fields don't drop as fast as the gas density with increasing radius. Instead, the strength of magnetic fields declines very slowly outward till about half of the virial radius. It is unclear whether this sudden drop is caused by the properties of the ICM motions or by the change of the simulation resolutions. The strength of magnetic fields increases about 10 times with the decrease of gas density from z=3 to z=0. It seems that magnetic fields are amplified and substained by the shear flows of the ICM turbulence. ICM turbulence and magnetic field amplifications will be discussed in Chapter 5 in detail.

3.3.4 Conclusions

In this section, we present a simulation of cluster formation with Biermann Battery effect to show the generations of magnetic fields in cluster scale by battery effect and the further evolution and amplifications of these initial magnetic fields by collapse and shear flows.

Biermann Battery mechanism generates magnetic fields in the collapsing gas at

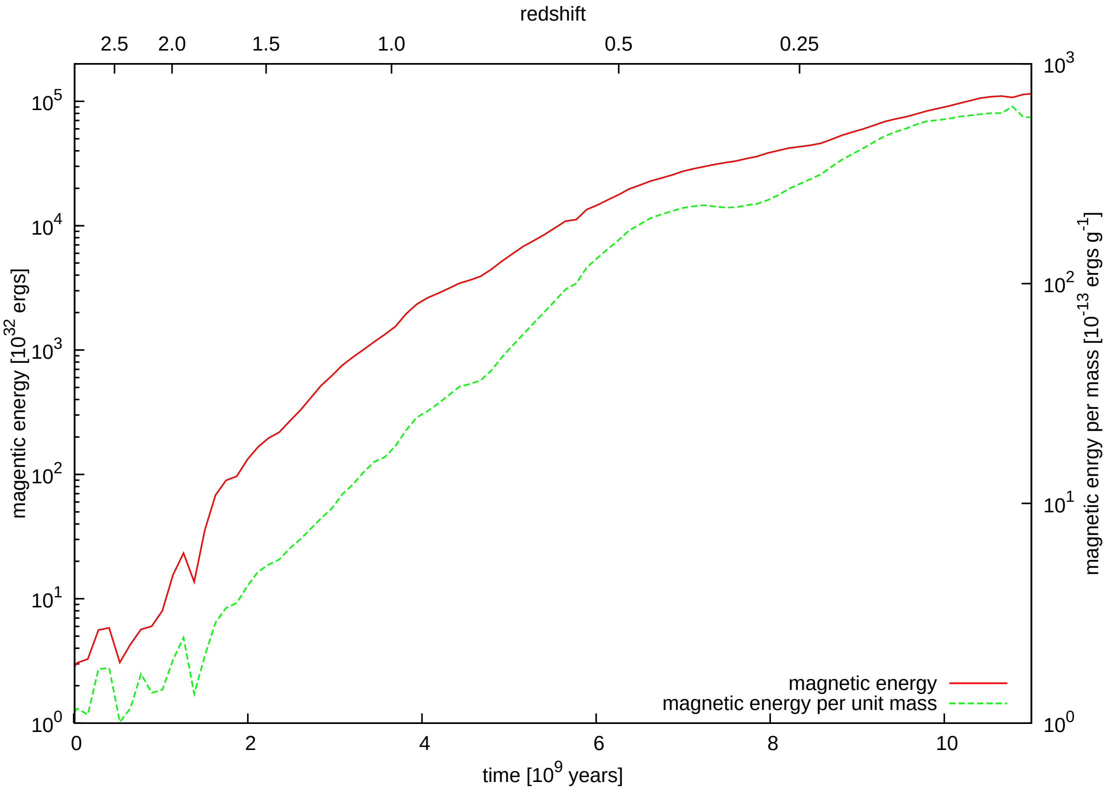

Figure 3.8: Evolution of magnetic energy and magnetic energy per unit mass inside half of the virial radius.

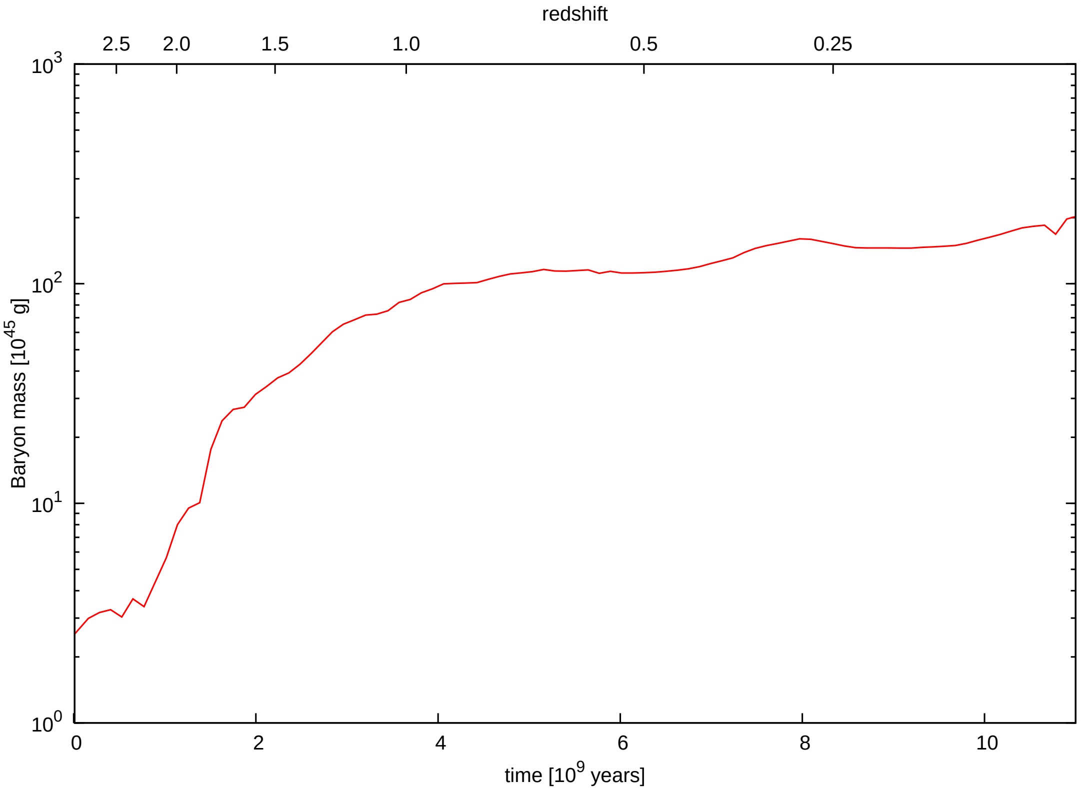

Figure 3.9: Gas mass inside sphere of half virial radius as function of time. The gas mass increases very slowly the first 1 Gyr without large merger, then very fast thereafter until z=1.

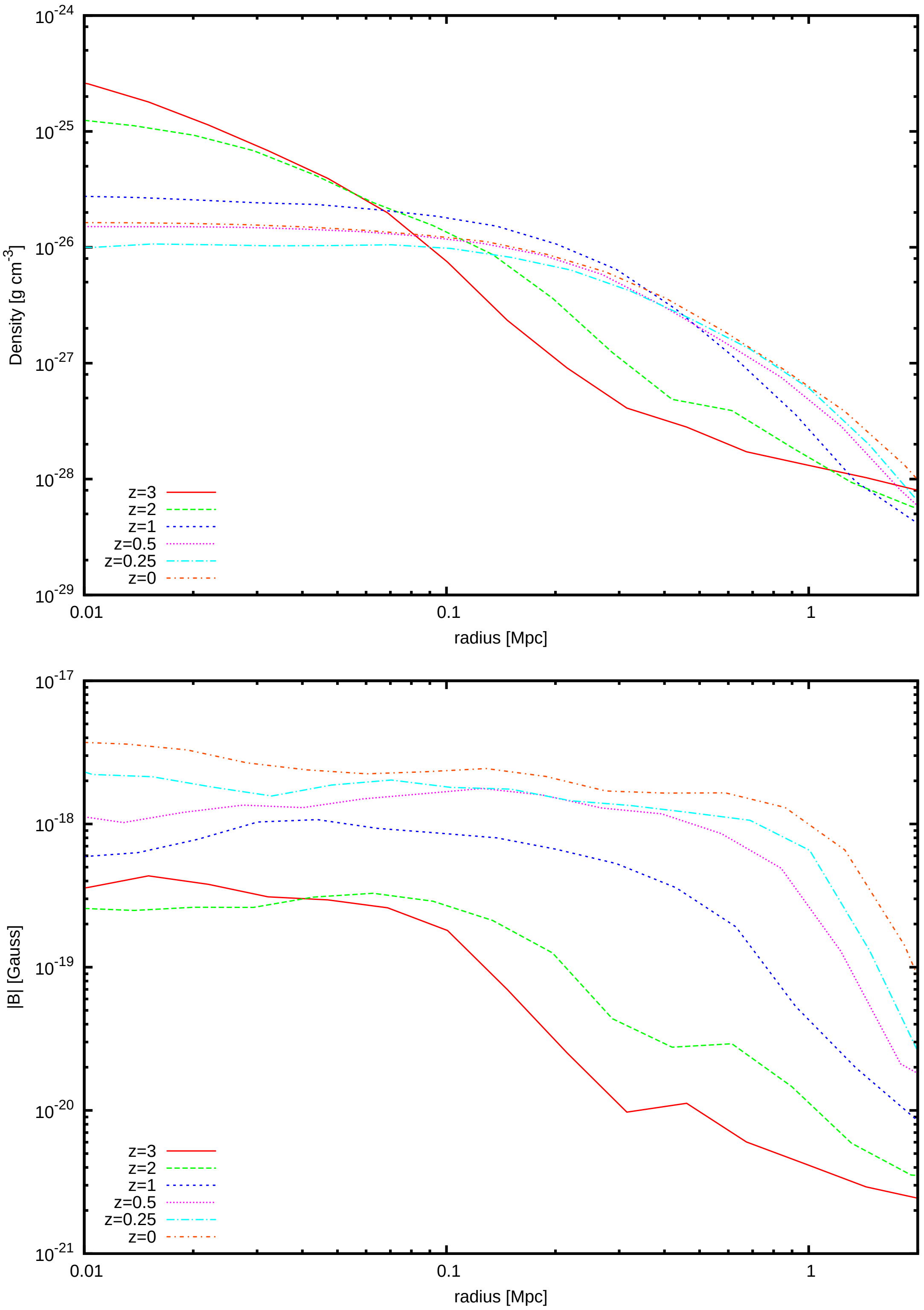

Figure 3.10: Spherically averaged radial profiles of gas density (top) and magnetic field strength (bottom) at different redshifts.

a very slow rate (generally not greater than 10^{-35} G s^{-1}). These magnetic fields are first amplified by the gravitational collapse. The magnetic fields are brought to the cluster while they are frozen-in the collapsing gas. The shear flows of turbulence in the cluster will further amplify and sustain the magnetic fields. The magnetic field strength profiles are flat extending to about half of the cluster, indicating that fields are amplified mainly by shear flows in the ICM instead of collapse.

The magnetic fields generated through this mechanism are much weaker than observed magnetic fields. So either another mechanism is required to further amplify magnetic fields in smaller scales (Kulsrud et al., 1997) or another source of magnetic fields is required to obtain the micro-Gauss fields in clusters. More discussions of origin and amplification of magnetic fields in cluster formation will be left to the Chapter 5.

Acknowledgments: This chapter, in part, is the material as it appears in the Astrophysical Journal, 688, L57-L60, 2008, Xu, Hao; O'Shea Brian W.; Collins, David C.; Norman, Michael L.; Li, Hui; Li, Shengtai, "The Biermann Battery in Cosmological MHD Simulations of Population III Star Formation", the University of Chicago Press, 2008. The dissertation author was the primary investigator and author of this paper.

Chapter 4

Formation of X-Ray Cavities by the Magnetically Dominated Jet-Lobe System in a Galaxy Cluster

4.1 Introduction

Active Galactic Nuclei (AGNs) are the most energetic eruptions in the universe. They may release as much as 10^{62} ergs of energy into ICM (McNamara et al., 2005). Recently observational and theoretical study of AGNs in galaxy clusters, especially about the giant X-ray cavities observed by high resolution X-ray observations of Chandra, suggests that large amounts of magnetic fields may be dominated components of AGN feedbacks (Diehl et al., 2008). In this chapter, I will discuss a model of magnetic fields injected from an AGN outburst into the ICM and the formation of X-ray cavities and weak shocks. This research also relates to the long time mystery of the source of non-gravitational heating the hot plasmas in the galaxy clusters.

The roles of AGNs in galaxy clusters have been seriously studied for the problem of heating hot atmosphere of galaxy clusters recently (see review by McNamara & Nulsen, 2007). The absence of spectral signatures of cooling plasmas at the galaxy cluster centers (Tamura et al., 2001; Peterson et al., 2003) has led to the suggestion that ICM in cluster centers must be heated. Powerful radio jet-lobes emanating from SMBHs in AGNs of clusters are considered to be the promising heating sources

(Binney & Tabor, 1995; Tucker & David, 1997). High resolution X-ray images of galaxy clusters by *Chandra* have revealed giant cavities and weak shock fronts in the hot gas (Fabian et al., 2000; McNamara et al., 2000, 2005), which are commonly associated with energetic radio lobes Blanton et al. (2001); Nulsen et al. (2002) and suggest that magnetic fields play an important role.

Large uncertainties concerning the nature of these cavities, their formation, evolution, and survivability in the ICM still remain. Numerical simulations of hot, underdense bubbles in galaxy clusters have been performed by a number of authors (e.g., Churazov et al., 2001; Reynolds et al., 2001; Brüggen & Kaiser, 2002; Omma et al., 2004). It is generally possible to inject a large amount of energy into the ICM via AGNs but it is not exactly clear how the AGN energy can be efficiently utilized (Vernaleo & Reynolds (2006), though see Heinz et al. (2006)). One of the most interesting characteristics of the radio bubbles is that they are intact, whereas most hydrodynamic simulations (Quilis et al., 2001; Brüggen & Kaiser, 2002; Dalla Vecchia et al., 2004) have shown that purely hydrodynamic bubbles will disintegrate in timescales much less than 10^8 yrs, markedly different from observations. (we will use X-ray cavities, bubbles, and radio bubbles interchangeably in this chapter). The stabilizing role of magnetic fields has been suggested and studied by a few authors (e.g., Jones & De Young, 2005).

A rather different class of models has been proposed and studied, in which the AGN energy output is modeled in the magnetically dominated limit (Li et al. (2006); Nakamura et al. (2006); see also the previous work of Blandford (1976); Lovelace (1976); Lynden-Bell (1996); Li et al. (2001)). The key feature of this model is to inject simultaneously both the poloidal and the (more dominant) toroidal magnetic fields in a small volume. This is to mimic the possible outcome of an accretion disk dynamo around an SMBH that shears and twists up the poloidal magnetic fields and generates large amounts of toroidal fields with an axial current (as high as 10^{19} amperes) flowing along the central axis of this magnetic structure. The injection of magnetic fields and their associated currents lasts a finite time (mimicking the lifetime of an AGN), after which the magnetic fields and their currents will no longer be injected but will continue to evolve and gradually dissipate away. This global current is essential to maintaining the magnetic structure throughout the lifetime of a magnetic field and its associated current. The system is not force-free initially, and so the fields will self-collimate and expand predominately axially, producing a collimated structure reminiscent of a "magnetic tower". Extensive 3-D magnetohydrodynamic (MHD) simulations based on this model in a static cluster-like background, have demonstrated that such magnetically dominated structures can reproduce some of the global features of the jet-lobe systems, especially in maintaining the integrity of the bubbles.

In this chapter, we present cosmological MHD simulations of a cluster formation with the feedback of an AGN, with the aim of understanding the X-ray cavity formation using the magnetically dominated models proposed by Li et al. (2006). This differs from all previous studies (Brüggen & Kaiser, 2002; Heinz et al., 2006) in that the formation of the X-ray cavity is studied in a realistic and self-consistent cosmological setting where the dark matter, baryon dynamics and magnetic fields are all evolved self-consistently. In Section 4.2, we describe our approach and the parameters of the simulations. In Section 5.3, we present the key results. Conclusions and discussions are given in Section 4.4.

4.2 Simulations

The galaxy cluster presented here is taken from the Simulated Cluster Archive of Laboratory of Computational Astrophysics at University of California, San Diego (http://lca.ucsd.edu/data/sca/). It uses a ΛCDM model with parameters $h = 0.7$, $\Omega_m = 0.3$, $\Omega_b = 0.026$, $\Omega_\Lambda = 0.7$, and $\sigma_8 = 0.928$. While these are not precisely the values determined by the latest observations (Spergel et al., 2007), the differences are unimportant for the conclusions of this study. For simplicity, the simulation is adiabatic without the additional physics such as radiative cooling and star formation feedback. (These effects are not essential for the purpose of this study but are required for the further research on the problem of heating ICM atmosphere.) The survey volume is 256 h^{-1} Mpc on a side. (For simplicity, all spatial scales in the rest of this chapter are normalized by the factor h^{-1} and are in comoving unit.)

The simulations were computed from cosmological initial conditions sampled onto a 128^3 root grid and 2 level nested static grids in the Lagrangian region where the cluster forms which gives an effective root grid resolution of 512^3 cells (0.5 Mpc) and dark matter particles of mass $1.49 \times 10^{10} M_{\odot}$. Adaptive mesh refinement (AMR) is used only in the region where the galaxy cluster forms, with a total of 8 levels of refinement beyond the root grid, for a maximum spatial resolution of 7.8125 kpc. At the center of the cluster when the AGN is "turned on" (see below), we further increased the resolution at the injection region to be ~ 1.95 kpc. While the baryons are resolved at higher and higher spatial and mass resolution at higher levels, the dark matter particles maintain constant in mass so as not to add any additional noise. The simulations were evolved from redshift $z = 30$ to $z = 0$.

The energy output from an SMBH is simulated by injecting magnetic energy in a small volume centered on a chosen massive galaxy that is at or near the center of the cluster. It is currently not possible to resolve both the galaxy cluster and the black hole environment simultaneously, so we have adopted an approach that mimics the possible magnetic energy injection by an SMBH (Li et al., 2006). The injected magnetic fields are determined by three key quantities: the length scale of the injection region r_0, the amount of poloidal flux Ψ_p, and the poloidal current I_z. In cylindrical coordinates, the injected poloidal flux Ψ_p (where $\Psi_p = rA_\phi$ and A_ϕ is the ϕ component of vector potential) is specified as:

$$\Psi_p(r, z) = r^2 \ exp(-r^2 - z^2) B_0 \tag{4.1}$$

where r is normalized by r_0.

Then the injected poloidal fields are

$$B_{inj,r} = -\frac{1}{r}\frac{\partial \Psi_p}{\partial z} = 2zr \ exp(-r^2 - z^2) B_0, \tag{4.2}$$

$$B_{inj,z} = \frac{1}{r}\frac{\partial \Psi_p}{\partial r} = z(1 - r^2) \ exp(-r^2 - z^2) B_0. \tag{4.3}$$

And the toroidal component is simply chosen as:

$$B_{inj,\phi} = \frac{\alpha \Psi_p}{r} = \alpha r \ exp(-r^2 - z^2) B_0 \tag{4.4}$$

here, the parameter α roughly specifies the flux ratio between toroidal and poloidal components. The magnetic fields are continuously injected into the system for a duration t_{inj}. So in the simulation, the injected magnetic fields are decided by r_0, B_0, α, and t_{inj}.

These initial magnetic fields are local since each component drops exponentially as a function of distance from the center. It is important that these fields are not in force equilibrium (Li et al., 2006). The radial force density alone the midplane (z=0), is:

$$F_r(z=0) = 2r(1-r^2)(10-\alpha^2-4r^2)exp(-2r^2) \tag{4.5}$$

and the vertical force density is,

$$f_z = 2zr^2(\alpha^2-10+4z^2+4r^2)exp(-2r^2-2z^2) \tag{4.6}$$

Figure 4.1 depicts the magnetic force with different α in some specific planes. For the case of $\alpha^2 > 10$, the magnetic force always drives the fields away from the midplane in the z direction.

We start the magnetic energy injection at redshift $z = 0.05$, at which the cluster has a virial radius $r_v \approx 1.5$ Mpc, a virial mass $m_v \approx 10^{15} M_\odot$, baryon to dark matter ratio 8.16%. In the cluster center where the chosen AGN is located, the gas density is 7.27×10^{-27} g cm^{-3}, pressure 1.49×10^{-10} dyn cm^{-2}, and temperature $1.45 \times 10^8 K$. The density profile of the ICM can be fitted as: $\rho = \rho_0[1 + (\frac{r}{r_c})^2]^{-3k/2}$ with $r_c = 100$ kpc and $k = 0.485$. Magnetic fields are injected for 36 Myr with $r_0 = 20kpc$, $B_0 = 80\mu G$, and $\alpha = 15$. After injection, a peak strength of magnetic energy is $\sim 200\mu G$. There are about 10^9 $M_\odot$ mass enclosed in the injection region. The evolution from $z = 0.05$ to $z = 0$ lasts about 670 Myr. So the cluster is still evolving while the magnetic fields from an AGN are injected and are piercing through the ICM. Many different simulations were performed with a range of injection parameters, but we present the results mostly using one simulation, while the conclusions drawn are general.

Note that after the first 36 Myr, magnetic fields and their associated currents are no longer injected. This, however, does not mean that the magnetic fields (and their currents) will disappear immediately. Instead, they will continue to evolve, gradually losing energy (especially in the early stages) by, say, doing work against the background ICM. Since the typical dynamic time is $\sim 10^8$ yrs and our simulation

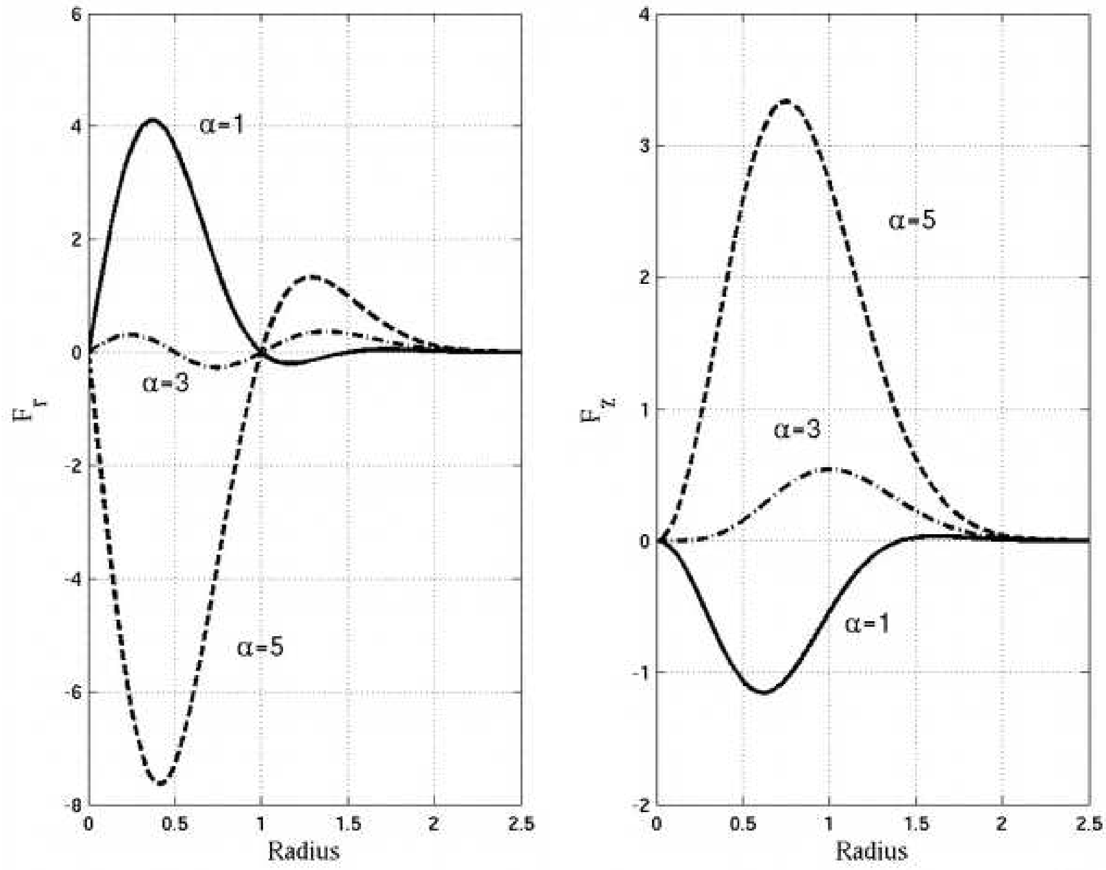

Figure 4.1: Magnetic force distribution of the magnetic injection model. Left panel: The radial component of the magnetic force as a function of radius r in the midplane with $\alpha = 1$, 3, and 5 for solid, dot-dashed, and dashed lines, respectively. Right panel: The vertical component of the magnetic force as function of radius r at the z=0.5 plane with $\alpha = 1$, 3, and 5 for solid, dot-dashed, and dashed lines, respectively. Image courtesy Hui Li, initially appeared in Li et al. (2006).

lasts 7×10^8 yrs, we do not expect the numerical dissipation of magnetic energy to play a major role. We have used high resolution on all the regions with magnetic fields (via AMR), so the numerical dissipation timescale should be much longer than the dynamic timescale.

4.3 Results

4.3.1 Stages of X-ray Cavity Formation

Images of the cluster at different epochs are given in Figure 4.2. The ranges of density are, from top to bottom, $3.70\times10^{-28}-8.77\times10^{-27}$, $9.41\times10^{-29}-6.24\times10^{-27}$, and $1.16 \times 10^{-28} - 5.67 \times 10^{-27}$ g cm^{-3}, respectively. A cutoff of 2×10^8 K is used in all temperature images. The minimum temperatures are 4.65×10^7, 6.78×10^7 and 6.9×10^7 K from top to bottom. The maximum magnetic energy density of each image is 4.16×10^{-11}, 1.67×10^{-11}, and 6.05×10^{-12} erg cm^{-3}. The ranges of path-integrated X-ray emission are $6.67\times10^{-7}-5.26\times10^{-5}$, $6.16\times10^{-7}-4.49\times10^{-5}$ and $4.25 \times 10^{-7} - 4.41 \times 10^{-5}$ erg cm^{-2} s^{-1}, from top to bottom, respectively. The integrated X-ray intensity is taken from the $0.5 - 7.5$ keV band with 0.3 solar metal abundance assumed. These projected results are obtained by integrating 336 kpc centered at the clsuter center along the line of sight.

A pair of cavities can be seen in the images at late times, which are created by the expansion of magnetic fields as they move out of the cluster core region. Note the relative motion between the cluster core and the injection location. The evolution of the total magnetic energy (integrated over the whole cluster) is given in Figure 4.3. We can see that the system first goes through an injection phase from $t = 0 - 36$ Myr, during which $\sim 6 \times 10^{60}$ ergs of magnetic energy is injected. This gives an average input power of 5.3×10^{45} ergs s^{-1}, which is comparable to the typical luminosity of a powerful AGN. At the end of the injection, only about 3.1×10^{60} ergs still remain in the magnetic form while the rest of the injected magnetic energy has all been transferred to the surrounding ICM. At $t = 48$ Myr, the poloidal current is $\sim 1.9 \times 10^{19}$ amperes along the central axis, whose corresponding toroidal magnetic fields self-collimate the outflow, which undergoes a supersonic expansion in

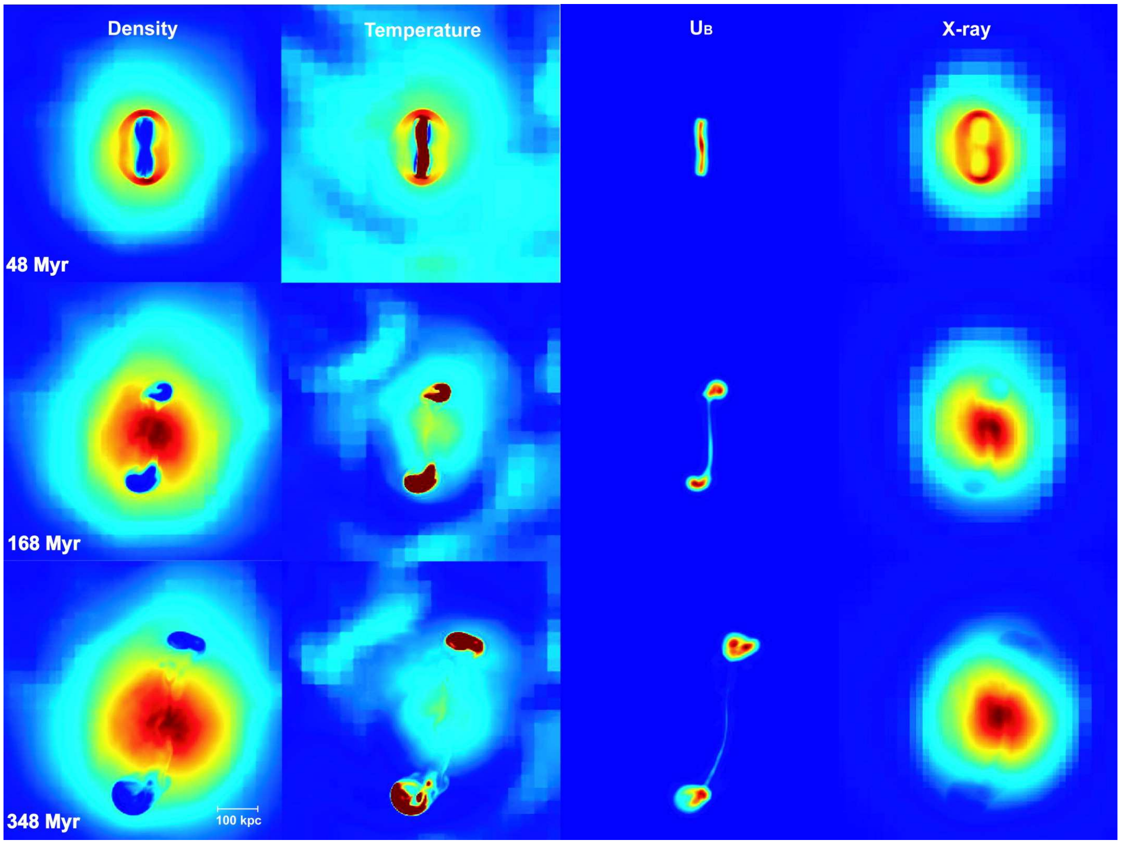

Figure 4.2: Snapshots of the jet-lobe evolution driven by the magnetic energy output of an AGN. Each image is 672 kpc on the side. Columns from left to right are slices of density, temperature, the averaged magnetic energy density and the integrated X-ray luminosity, respectively. The top row shows the cluster with the jet-lobe at the end of magnetic energy injection. The middle and bottom rows show the well-developed bubbles moving out of the cluster center. The bubbles are driven by magnetic forces at all stages, and might become buoyant only after $t > 500$ Myr. (Each image uses its own color map as described in text.)

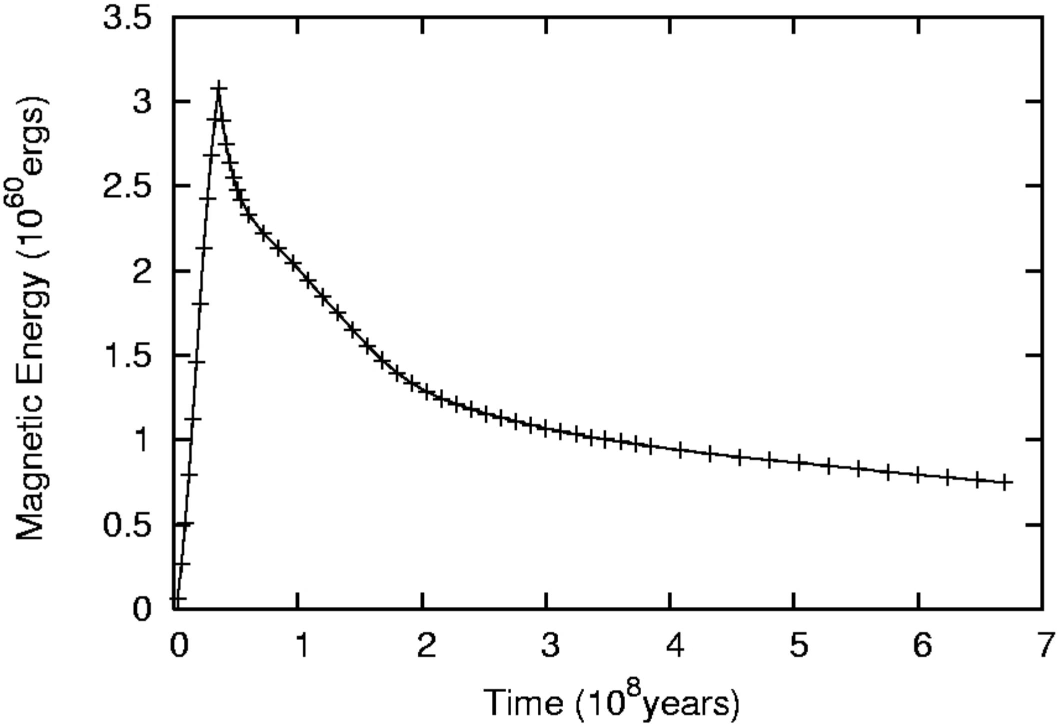

Figure 4.3: Evolution of the total magnetic field energy in the cluster from redshift $z = 0.05$ to $z = 0$. The initial increase comes from the injection (which ends at 36 Myr), followed by a continual decline as the jet-lobe system converts magnetic energy to thermal, kinetic and gravitational energies of the background ICM.

the cluster core region (Li et al., 2006; Nakamura et al., 2006) and forms a "tower-like" structure.

Once the injection ceases, the magnetic energy in the cluster starts to decrease, first at a fast rate ($\sim 10^{52}$ ergs yr^{-1}) from $t \sim 40 - 200$ Myr, followed by a much slower rate ($\sim 10^{51}$ ergs yr^{-1}) from $t \sim 200 - 670$ Myr. This transition coincides with the time when the magnetic lobes leave the cluster core region ($\sim$ 100 kpc, the middle row of Figure 4.2). The plasma density and pressure of the ICM drop rapidly beyond the core, hence the slower rate of magnetic energy dissipation. The poloidal current is $\sim 5 \times 10^{18}$ ampere at $t = 348$ Myr. Once the magnetic lobes leave the cluster core, they experience additional expansion, forming the round or flattened shapes, depending on the surrounding cluster environment (the bottom row of Figure 4.2, more details in the next subsection). The final total magnetic energy in the cluster is about 7.5×10^{59} ergs, roughly $\sim 10\%$ of the total injected magnetic energy. This implies that $\sim 90\%$ of the injected magnetic energy has been transferred to the ICM: their thermal energy (heating via compression and shocks), their kinetic energy (driving the bulk flows), and their potential energy (being lifted in the cluster potential well).

4.3.2 Shock Fronts and Cavity Properties

Chandra observations have revealed that shocks around the radio lobes are weak (Fabian et al., 2003; Nulsen et al., 2005; McNamara et al., 2005). In our simulations, a global shock front enclosing the whole magnetic structure is generated early by the injection of magnetic fields. At $t = 48$ Myr, the shock's Mach number is about 1.55 at a distance roughly 92 kpc away from the central galaxy. This shock, which is hydrodynamic in nature, gradually weakens as it moves ahead of and away from the magnetic structure. By $t = 168$ Myr, the shock is about 261 kpc away and barely visible (the middle row of Figure 4.2), with a Mach number just above 1. After this time, the shock is dissipated into the background ICM.

The Lorentz forces from the magnetic fields expand the magnetic structure and push the ICM away. In the nearly ideal MHD limit, the plasma is "frozen in" with the magnetic fields, and the mixing between the magnetized jet-lobe system and the background ICM is inhibited. So the plasma density associated with the magnetic structure decreases as the jet expands, creating the density cavities. The magnetic fields undergo significant lateral expansion as they leave the central core region (the middle and bottom rows of Figure 4.2). The formation of such large, relatively "round" lobes is jointly determined by the ambient ICM pressure and an axial electric current which flows along the "spine" of the magnetic structure and returns around the outer boundary of the lobes and jets. The central poloidal current generates toroidal magnetic fields whose strength behaves as $1/r$ where r is the cylindrical distance from the jet axis. Such a decreasing magnetic pressure ($\propto 1/r^2$) is eventually balanced by the background ICM pressure, thus determining the size of the X-ray cavity. More detailed comparisons with a large set of bubble observations show that such a magnetically dominated model agrees quite well with bubbles' size and distance distributions (Diehl et al., 2008).

To illustrate the internal property of the lobes, we take a horizontal "cut" through the southern lobe at $t = 168$ and 348 Myr (Figure 4.2) and plot its properties along the line in Figure 4.4. At $t = 168$ Myr, the cavity is clearly dominated by magnetic energy. The peak magnetic field strength is probably higher than the inferred typical field value from observations. At $t = 368$ Myr, it has a comparable amount of total magnetic energy ($\sim 2.4 \times 10^{59}$ ergs) and thermal energy ($\sim 2.2 \times 10^{59}$ ergs). The total kinetic energy is much smaller, $\sim 3.6 \times 10^{58}$ ergs. The implied enthalpy upper limit of this lobe is $4pV \approx 8.8 \times 10^{59}$ ergs. Assuming that the northern lobe has a similar energetics as the southern lobe, the total enthalpy in the lobes is $\sim 1.8 \times 10^{60}$ ergs, which is much smaller than the amount of magnetic energy that has been transferred, $\sim 5.2 \times 10^{60}$ ergs. So the enthalpy could be a serious under-estimate of the injected magnetic energy.

To demonstrate the influence of background motions on the bubbles, we plot the slices of gas density overlaid with the velocity fields at 48 and 348 Myr after injection start in Figure 4.5. It clearly shows how the shapes and positions of the bubbles are affected by the background flows around the cluster center. On the upper part, the flows are downward near the center and rightward further away. So the upper bubble is flattened by the compression between the downward flows and the upward motion of the bubble driven by the magnetic pressure and the buoyant force, and it moves a lot to the right with the motion of cluster center. The background flows below the cluster center is majorly downward. So the lower bubble moves basically straight downward and is much farther away from the cluster center thnn the upper bubble. Without compression, it keeps round shape pretty well.

Figure 4.6 shows the bubbles at $z = 0$ ($t = 672 Myr$) when the simulation ends. The north and south bubbles are already out of the core region and at about 270 kpc and 300 kpc, respectively, away from the cluster center. The semimajor and semiminor axes of the north bubble are 65 kpc and 35 kpc, respectively. The radius of the south bubble is about 60 kpc. The two bubbles are still intact and interconnected by magnetic fields.

It has often been suggested that the evolution of the X-ray bubbles is driven by

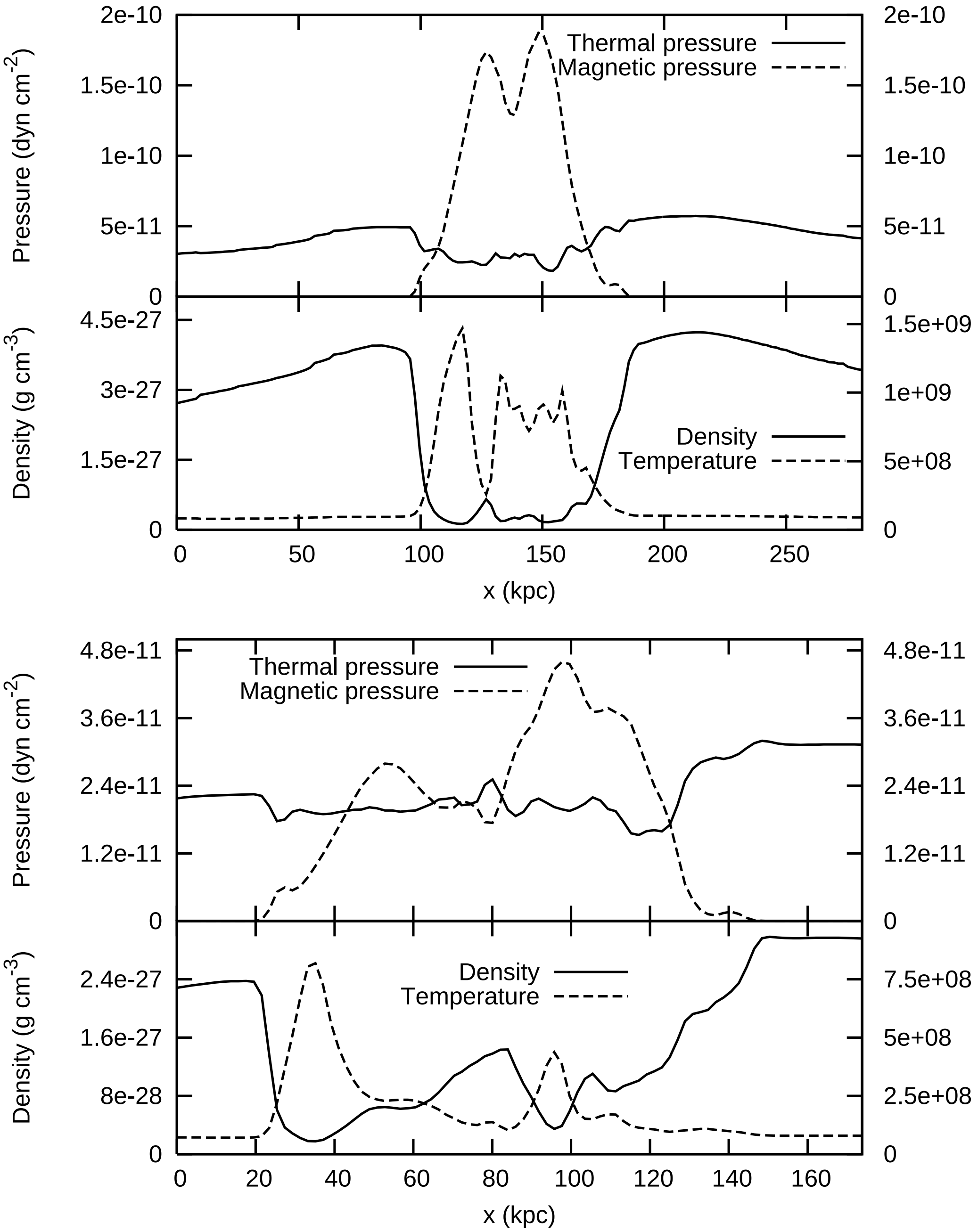

Figure 4.4: Spatial distribution of magnetic pressure, thermal pressure, density, and temperature along a horizontal line through the southern lobe at $t = 168$ Myr (*top*) and $t = 348$ Myr (*bottom*). The lobe is dominated by the magnetic pressure.

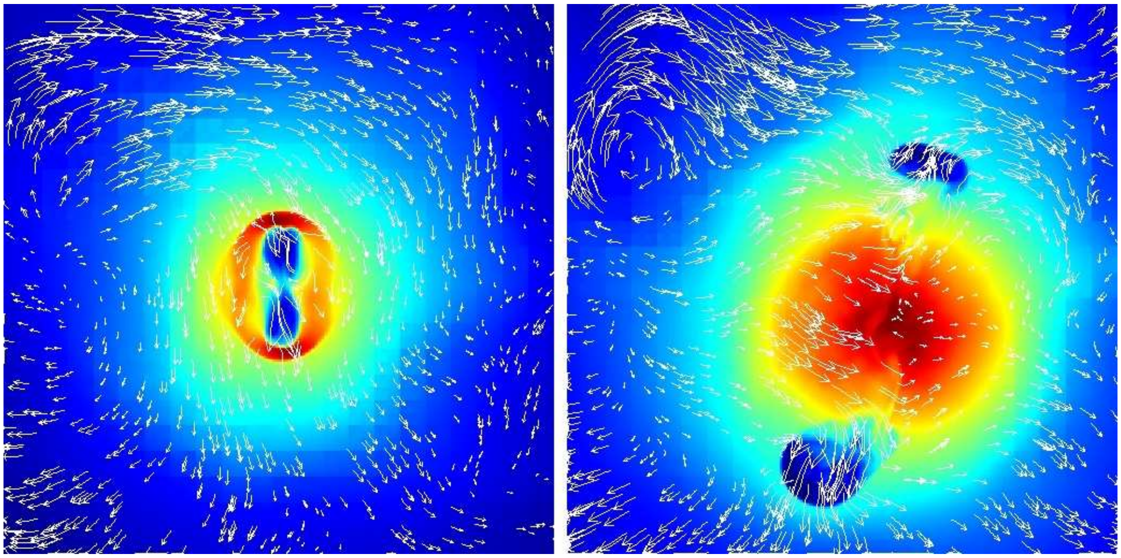

Figure 4.5: Slices of gas density overlaid with velocity fields. Each plot covers an area of 672 kpc × 672 kpc. The left panel is at $t = 48$ Myr and the right panel is at t=348 Myr.

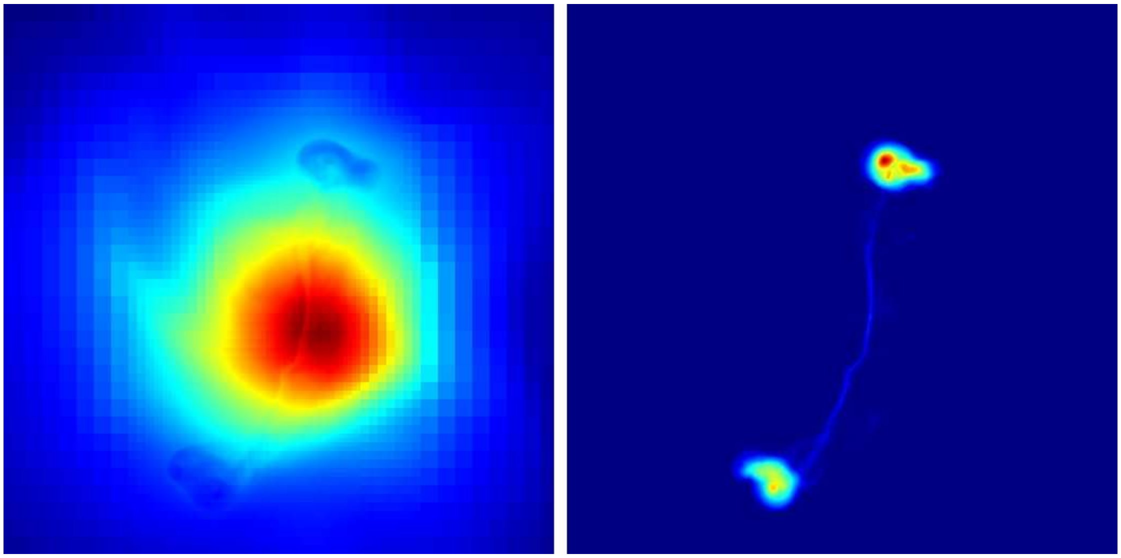

Figure 4.6: Projected gas density (left panel) and magnetic energy density (right panel) at $z = 0$ ($t = 672$ Myr). Each plot is 1 Mpc on a side. Two intact bubbles are still interconnected by magnetic fields.

buoyancy. Using lobe's size, distance from the galaxy and cluster gravity, we have computed the implied buoyancy time by pretending they were buoyant. We found that the calculated buoyancy times are ~ 236 and 437 Myr, whereas the actual evolution times are 168 and 348 Myr, respectively. The difference does get smaller at late times (> 500 Myr).

4.4 Conclusions and Discussions

With our cosmological AMR MHD simulations, we find that, in the realistic cluster environment where the ICM plasma interacts dynamically with the magnetic jet-lobe, X-ray cavities can naturally form using the magnetically dominated model proposed by Li et al. (2006). The magnetic fields inside the bubbles stabilize the interface instabilities so that bubbles can remain intact. The lifetime of these bubbles can be quite long and these bubbles only become truly buoyant probably after ~ 500 Myr.

We have performed additional cosmological MHD simulations with radiative cooling and star formation feedback and found that our conclusions for the X-ray cavity formation mechanism do not change. While we have demonstrated the formation of X-ray cavities, much more studies are needed in order to address comprehensively the cooling flow problem at the cluster cores. The present simulation, with just one AGN, already has important implications for understanding the ICM heating problem. Up to $80\% - 90\%$ of the injected energy has been dissipated in the surrounding ICM. Further studies are underway with AGNs at different redshifts that have different cluster environments so that we can gain a comprehensive understanding of the overall heating of the ICM by AGNs. The morphology of the jet-lobe is dependent on the background density radial profile, which is different for massive clusters (such as the one presented here) and groups or poor clusters. Future work will address this issue.

The research presented in this chapter further supports the idea that large amounts of magnetic energy are injected into the ICM by AGNs in galaxy clusters. This makes AGN feedback a promising origin of magnetic fields in galaxy clusters. Observations have already found quasars at high redshifts up to ~ 6 (Fan et al., 2001). Magnetic fields from them may be important sources of large sclae cluster magnetic fields. We will discuss long term evolution of magnetic fields from high redshift AGN in galaxy cluster in the next chapter.

Acknowledgments: This chapter, in part, is the material as it appears in the Astrophysical Journal, 681, L61-L64, 2008, Xu, Hao; Li, Hui; Collins, David C.; Li, Shengtai; Norman, Michael L., “Formation of X-Ray Cavities by the Magnetically Dominated Jet-Lobe System in a Galaxy Cluster”, the University of Chicago Press, 2008. The dissertation author was the primary investigator and author of this paper.

Chapter 5

Magnetizing the ICM by Magnetic Field Injection from High Redshift AGN

5.1 Introduction

There is growing evidence that the ICM is permeated with magnetic fields, as indicated by the detection of large-scale, diffused radio emission called radio halos and relics (see recent reviews by Ferrari et al., 2008; Carilli & Taylor, 2002). The radio emissions are extended over ≥ 1 Mpc, covering the whole cluster. By assuming that the total energy in relativistic electrons is comparable to the magnetic energy, one often deduces that the magnetic fields in the cluster halos can reach $0.1-1.0\ \mu$G and the total magnetic energy can be as high as 10^{61} ergs (Feretti, 1999). The Faraday rotation measurement (FRM), combined with the ICM density measurements, often yields cluster magnetic fields of a few to ten μG level (mostly in the cluster core region). More interestingly, it reveals that magnetic fields can have a Kolmogorov-like turbulent spectrum in the cores of clusters (Vogt & Enßlin, 2003) with a peak at several kpc. Other studies have suggested that the coherence scales of magnetic fields can range from a few kpc to a few hundred kpc (Eilek & Owen, 2002; Taylor & Perley, 1993; Colgate et al., 2001), implying large amounts of magnetic energy and fluxes. Understanding the origin and effects of magnetic fields in clusters is important because they play a crucial role in determining the structure of clusters through processes such as heat transport, which consequently affect the applicability of clusters as sensitive probes for cosmological parameters (Voit, 2005).

Although the existence of cluster-wide magnetic fields is clear, their origin is still poorly understood. Two scenarios have received most attention: a) magnetic fields are initially from the outflows of normal or active galaxies (Donnert et al., 2009; Furlanetto & Loeb, 2001; Kronberg et al., 2001), and such fields can be further amplified by cluster merger (Roettiger et al., 1999) and turbulence (Dolag et al., 2002; Dubois & Teyssier, 2008); and b) very small proto-galactic seed fields are amplified by dynamo processes in clusters (Kulsrud et al., 1997; Ryu et al., 2008), though the exact mechanism for dynamo is still being debated (Bernet et al., 2008).

Large scale radio jets from AGNs serve as one of the most intriguing candidates in the first scenario because they could carry large amount of magnetic energy and flux (Burbidge, 1959; Kronberg et al., 2001; Croston et al., 2005; McNamara & Nulsen, 2007). The idea that AGN is the origin of cluster magnetic fields has a long history (Hoyle, 1969; Rees, 1987; Daly & Loeb, 1990). The central supermassive black hole releases gravitational energy during mass accretion to power the AGN. The magnetic fields, either existed with collapsing gas or generated by Biermann battery effect, will be amplified rapidly by an $\alpha - \Omega$ dynamo in the rotating disk (Colgate et al., 2001). The magnetization of the ICM and the wider inter-galactic medium (IGM) by AGNs has also been suggested on the energetic grounds (Colgate et al., 2001; Furlanetto & Loeb, 2001; Kronberg et al., 2001), though the exact physical processes of how magnetic fields will be transported and amplified remain sketchy. Some of the key physics questions in these models include: what is the volume filling process of AGN magnetic fields in the ICM/IGM? Is the ICM turbulent and what are its properties? Is there a dynamo in the ICM that can amplify fields?

In the previous chapter, we already discussed that the jets generated by AGNs are likely to be magnetic-dominated and the jets/lobe systems and then the magnetic bubbles bring magnetic fields into the intracluster medium. In this chapter, we present self-consistent cosmological MHD simulations of further evolution of magnetic fields injected into the ICM by the AGN at high redshift showing how the ICM are magnetized by these local injected magnetic fields and the motions of the plasmas of the galaxy cluster.

5.2 Basic Model and Simulations

We used the same cluster formation simulation as in the previous chapter. The simulations were evolved from redshift $z = 30$ to $z = 0$ adiabatically. Initially, the cluster has no magnetic field. We "turn on" the AGN magnetic injection at redshift $z = 3$, centered at a massive galaxy in a proto-cluster which has a virial radius $r_v \approx 0.15$ Mpc, a baryon virial mass $m_b \approx 3.2 \times 10^{11}\ M_\odot$, and a virial total mass $m_v \approx 7.6 \times 10^{12}\ M_\odot$. The cluster eventually grows to $r_v \approx 2.15$ Mpc, $m_b \approx 9.0 \times 10^{13}\ M_\odot$, and $m_v \approx 1.1 \times 10^{15}\ M_\odot$ by $z = 0$. The total injected magnetic energy by AGN is about 2×10^{60} ergs, with an average input power of 1.75×10^{45} ergs s^{-1} for a duration of 36 Myr. The magnetic energy is injected inside $0.2\ r_v$. Because it is currently not possible to resolve both the galaxy cluster and the AGN environment simultaneously, we use the approach described in the previous chapter that mimics the possible magnetic energy injection by an AGN (Li et al., 2006). The size of the injection region and the associated field strength are not realistic when compared to the real AGN jets, but on global scales, the previous studies by Nakamura et al. (2006) and Xu et al. (2008a) (or Chapter 4) showed that this approach can reproduce the observed X-ray bubbles and shock fronts (McNamara et al., 2005).

AMR is allowed only in a region of (50 Mpc)^3 where the galaxy cluster forms. During the cluster formation, the refinement is controlled by baryon and dark matter overdensity. In addition, all the region where magnetic field strength is higher than 10^{-7} G will be refined to the highest level. There are a total of 8 levels of refinement beyond the root grid, for a maximum spatial resolution of 11.2 kpc. Consequently, our simulations are equivalent to $\sim 600^3$ uniform grid MHD runs in the cluster region with full cosmology. Figure 5.1 shows cumulative magnetic energy distribution at different redshift. More than 99% magnetic energy is inside the regions refined to the highest resolution at any redshifts. The simulation was performed on the linux cluster Coyote at LANL with about 300,000 CPU hours consumed.

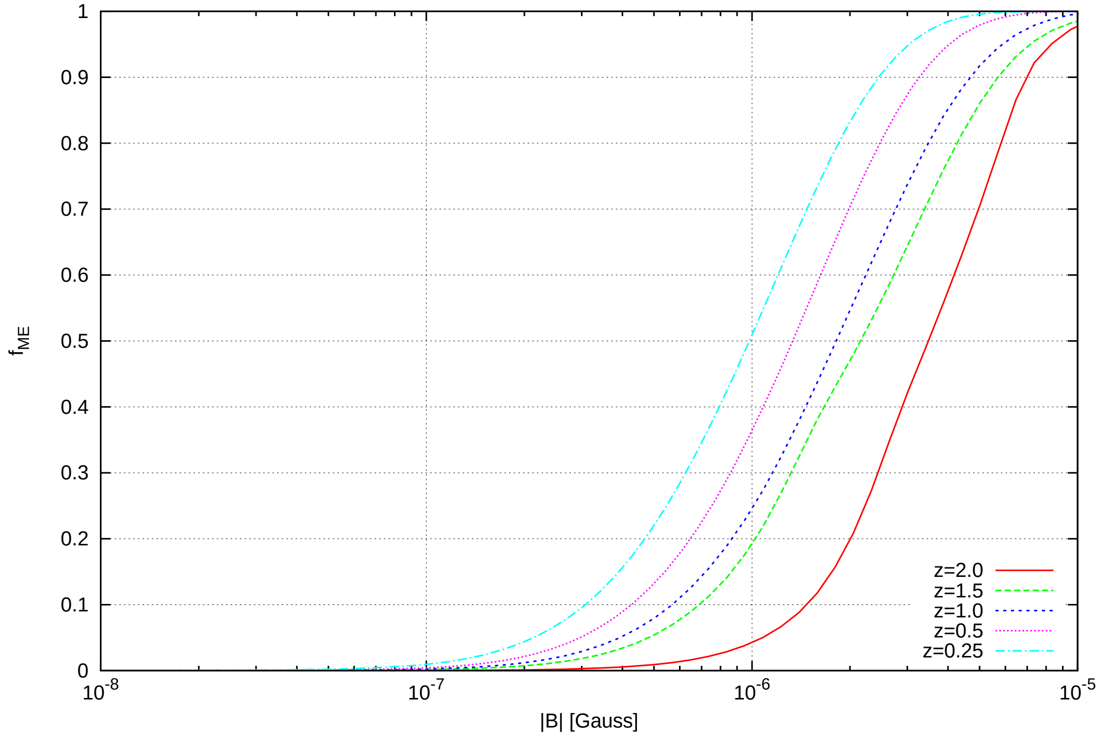

Figure 5.1: Cumulative magnetic energy distributions at different redshifts. At any time, the energy of magnetic fields with strength smaller than 10^{-7} G is less than 1% of the total magnetic energy. So most of the regions with significant magnetic fields are refined to the highest level.

5.3 Results

5.3.1 Global Morphology

To illustrate the formation and evolution of the cluster along with the evolution of magnetic fields from the AGN, we present images of the projected gas density and magnetic energy density at different stages of cluster formation in Figure 5.2. At $z = 3$ ($t = 0$), an AGN is "turned on" in a sub-cluster (which eventually merges with another sub-cluster about 400 Myr after the AGN injection has finished). The AGN is "turned off" at $t = 36$ Myr ($z = 2.95$). At $t = 180$ Myr, we see the density cavities produced by the AGN magnetic fields, reminiscent of the jet-lobe structure of radio galaxies (Xu et al., 2008a). At a later time $t = 468$ Myr, the jet-lobe structure is destroyed by the cluster mergers. When two sub-clusters just finish merging at $t = 1.1$ Gyr (z=2.0), a large part of magnetic fields is carried out of the cluster center region by the ejected flow from mergers. As the evolution progresses, magnetic fields, which follow the plasma motion, are being sheared, twisted, and spread throughout the whole cluster. Judging by the images from $t = 1.1$ to $t = 6.28$ Gyr, this volume-filling process is quite efficient. By $z = 0.5$ ($t = 6.28$ Gyr), magnetic fields are well mixed with the ICM and are distributed quasi-uniformly throughout the whole cluster, except some high magnetic fields regions obviously from compression by shocks. At $z = 0.0$, while the cluster is relaxed, the magnetic fields are quite uniform disturbed.

5.3.2 Energy Evolution and Magnetic Field Radial Profile

The evolution of the total thermal, kinetic, and magnetic energy inside the cluster's virial volume is shown in the top panel of Figure 5.3. The kinetic energy is calculated as the turbulent component by subtracting the bulk flow motion. By the AGN injection, $\sim 2 \times 10^{60}$ ergs of magnetic energy is input into a sub-cluster. A significant fraction ($\sim 80\%$) of this energy is deposited into the ICM due to expansion and heating (Xu et al., 2008a). When the two big sub-clusters merge at $t = 400$ Myr, the total thermal and kinetic energies of the cluster increase by ten-fold by $t \sim 600$ Myr. During this major merger, the magnetic fields are still very local,

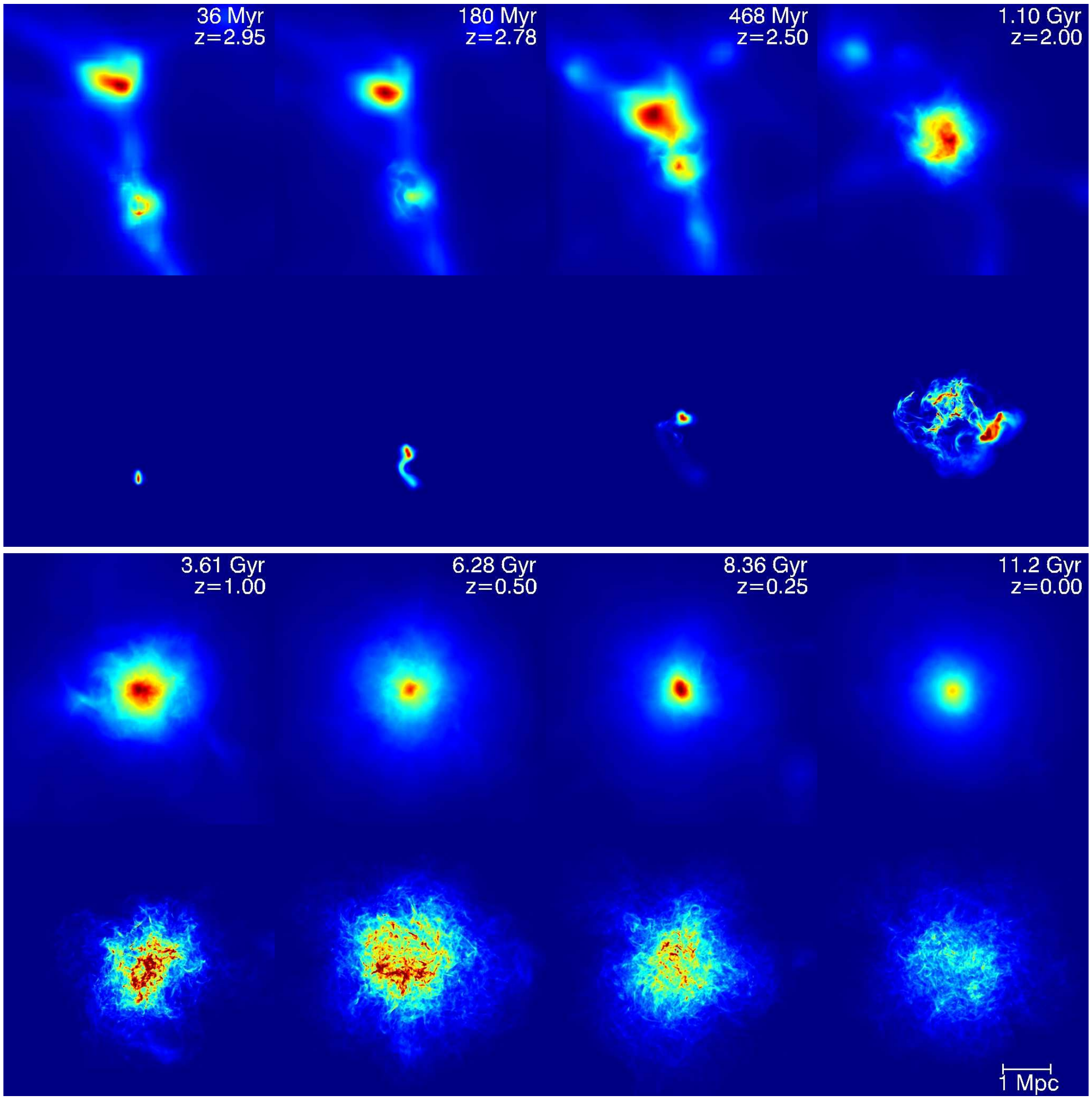

Figure 5.2: Snap shots of the projected baryon density (upper rows) and magnetic energy density (lower rows) for different epochs of cluster formation and evolution. Each image covers a region of 5.71 Mpc × 5.71 Mpc (comoving). The projection results are obtained by integrating along 5.71 Mpc comoving centered at the cluster along lines perpendicular to the observed plane. The eight columns are marked with the time t since the AGN injection and the respective redshift z. The top panel uses diffrent color scale for each plot to have the best visual effect. The color ranges of bottom panel are from 4.2×10^{19} to 1.3×10^{22} cm^{-3} for the baryon particle number density and from 0 to 5×10^{11} ergs cm^{-2} for the integrated magnetic energy density.

largely in magnetic bubbles. So the merger event itself did not significantly change the magnetic field energy. The thermal and kinetic energies of the cluster continue to increase as the cluster grows in mass via accretion and mergers as indicated by the variations in the energy evolution curves. At $t \sim 2$ Gyr, the magnetic fields from the AGN have been spread throughout a significant volume of the cluster (see Figure 5.2). Starting from this time, the magnetic energy experiences an exponential increase by a factor of 20 until $t \sim 6$ Gyr, at which time the growth has slowed. After $t \sim 6$ Gyr, the cluster grows slowly in its total energy and becomes relaxed, and the magnetic energy increases slowly with the growth of the cluster. By $z = 0$, the total magnetic energy has reached $\sim 10^{61}$ ergs inside the cluster.

In the bottom panel of Figure 5.3, we present the spherically averaged magnetic field strength radial profiles. At $z = 0.0$, the magnetic field strength is ~ 1.5 μG at the core, decreasing slowly to ~ 0.7 μG at $\sim$ Mpc radius. These radial profiles are different from what is shown by other simulations which often exhibit faster radial decline (Dolag et al., 2002; Dubois & Teyssier, 2008; Donnert et al., 2009). It is presently unclear whether this difference is caused by the different origin of the "seed" magnetic fields or by the effects of numerical resolution. These radial profiles are consistent with observations of Govoni et al. (2006); Guidetti et al. (2008), of which the average magnetic field strength calculated over 1 Mpc^3 is about 1 μG.

5.3.3 Small-scale Dynamo and MHD Turbulence

The physical origin for the exponential amplification of the magnetic energy is due to a cluster-wide turbulent dynamo process. In Fig. 5.4 we present the power spectra of the ICM plasma's kinetic energy density and magnetic energy density in a comoving cube with 5.71 Mpc on the side. The scales are shown in the comoving units so that they are not affected by the universe expansion and the power changes are from the dynamics of cluster evolution alone. Here, $k = 0.003$ kpc^{-1} corresponds to the maximum radius of the central region 2.86 Mpc where a high spatial refinement is adopted. Since the cluster's total thermal energy is a factor of $\sim 3 - 5$ larger than its kinetic energy, the ICM can be thought as nearly incompressible plasmas overall, though shocks generated by mergers are very frequent and important. In

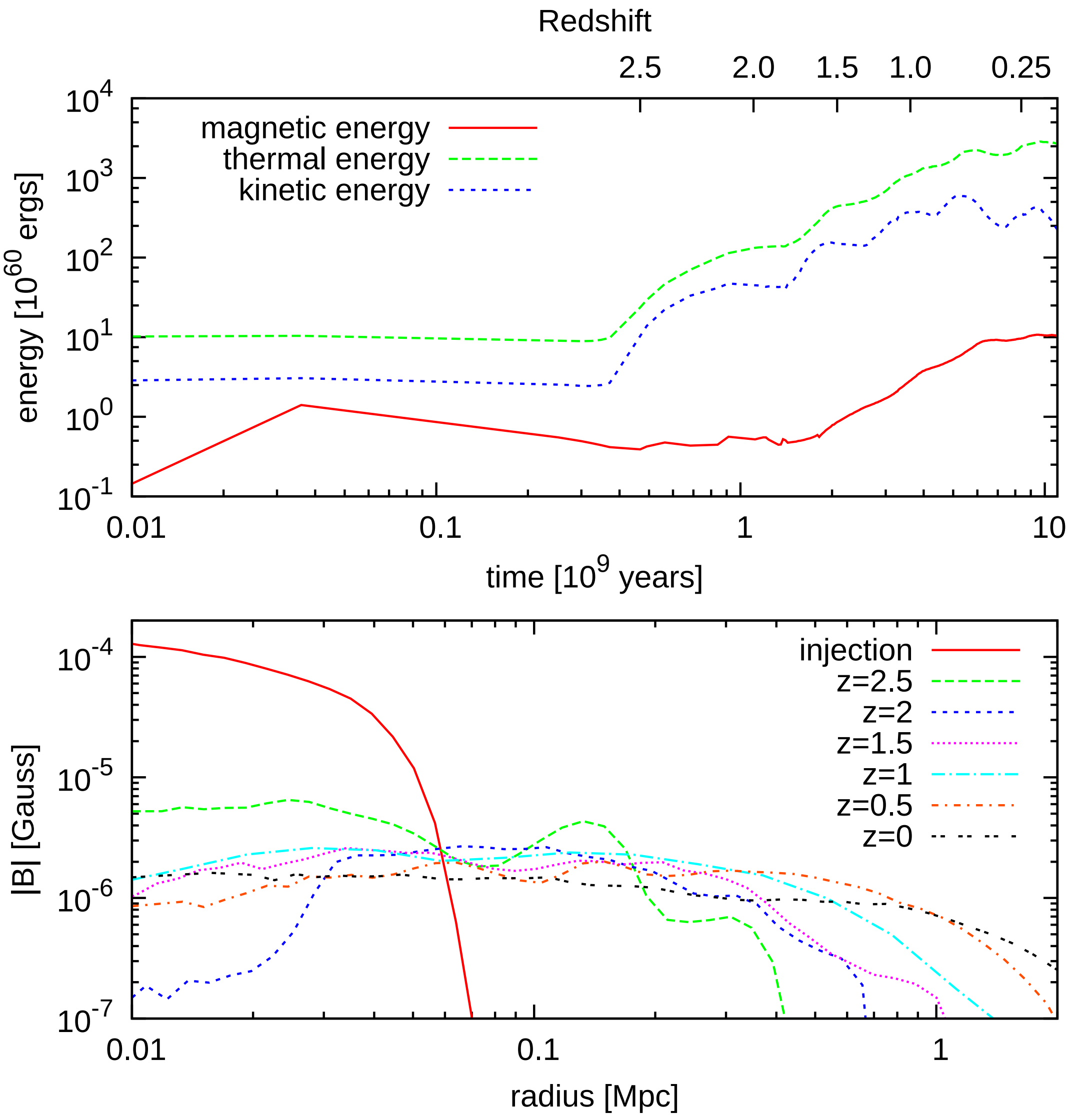

Figure 5.3: Top panel: Temporal evolution of different componets of energy inside the virial radius of the cluster. The variations in the thermal and kinetic energies are due to mergers. Bottom panel: The spherically averaged radial profile of magnetic field strength at different epochs of the cluster formation. The radius is measured in the proper frame. They show the turbulent diffusion of magnetic fields throughout the cluster, yet maintaining its strength via the dynamo process.

fact, the flows and shocks from mergers tend to be global and propagate through the whole cluster (see also the earlier work by Roettiger et al., 1999). We can divide the full kinetic spectrum approximately into three regions: the "injection" region for $k \sim 0.003 - 0.01$ kpc^{-1} where the large scale flows and shocks from the mergers "stir" the whole cluster; the "cascade" region for $k \sim 0.01 - 0.1$ where the spectrum shows a smooth power law similar to a Kolmogorov-like incompressible turbulence; the "dissipation" region for $k > 0.1$ where the spectrum steepens gradually. We attribute this steepening to both the dissipation by shocks (which has a physical origin) and the limited spatial resolution (which has a numerical origin). These features in the kinetic energy density spectrum lead us to conclude that the ICM is turbulent and our simulations have captured the essence of this turbulence. This ICM turbulence is in a driven-dissipative state where frequent mergers will drive the turbulence over relatively short time scales (a few Myr) but the turbulence is decaying in-between mergers on timescales of $\sim$ Gyr (which is approximately the dynamic timescale for the whole cluster).

The magnetic energy density spectrum also has three regions in the $k-$space corresponding to the kinetic energy spectrum. From $t = 2$ to $t = 10$ Gyr ($z = 1.5$ to $z = 0.1$), the magnetic spectrum for $k \sim 0.01 - 0.6$ retains an "invariable" shape but the energy density undergoes exponential amplification then goes into saturation. This is a strong signature for the so-called small-scale turbulent dynamo (Brandenburg & Subramanian, 2005). Furthermore, the magnetic energy density peaks at $k \sim 0.2$ with $\sim 3 \times 10^{-16}$ ergs cm^{-3}. The corresponding kinetic energy density is $\sim 8 \times\ 10^{-16}$ ergs cm^{-3}. So, the magnetic energy for $k > 0.1$ has saturated at a sub-equipartition level (by a factor of ~ 3). The drop-off at high k should be due to the numerical dissipation. For $k < 0.01$, neither kinetic or magnetic energy seems to have saturated. It is interesting to note that the dynamo process starts vigorously only at $t \sim 2$ Gyr ($z = 1.5$), when the magnetic fields have been spread through a significant fraction of the whole cluster (see Fig. 5.2). Putting Figs. 5.2 - 5.4 together, we see that the ICM turbulence both amplifies the magnetic energy and diffuses the fields throughout the cluster. The magnetic energy density saturation occurred at $t \sim 6$ Gyr but magnetic fields continue to "grow" in their spatial extent through turbulent diffusion. Furthermore, the un-signed magnetic flux through the mid-plane of the cluster has exponentially grown from 7.6×10^{41} to 1.23×10^{43} G cm^2 from $z = 2$ to $z = 0.5$, which is another clear indication of the turbulent dynamo that is responsible for both amplifying the field energy and diffusing the field through the cluster.

5.3.4 Distribution of Plasma β

Thermal and kinetic energies dominate the magnetic energy in the cluster level. To show the relative importance of magnetic fields locally, we plot the volume histograms of plasma β (ratios of thermal and kinetic energy densities to magnetic energy density) inside a sphere of 1 Mpc proper centered at the cluster center at different redshifts in Figure 5.5. At early time, the magnetic fields only occupy a very small volume. Then the magnetic fields fill a larger and larger volume with the spreading of magnetic fields in the ICM and the expansion of the universe. At z=0.25, The thermal β peaks at about 300 and the kinetic β peaks at about 25. The thermal energy density is always larger than the mangetic energy density in the whole region, and the magnetic energy density is only greater than or similar to kinetic energy density in a small fraction of the volume, where magnetic fields are dynamically important. Further research is needed to understand why the magnetic energy density in most regions keeps much smaller than the kinetic energy density.

5.3.5 Faraday Rotation Measurement

We have also computed the synthetic FRM by integrating to the mid-plane of the cluster. Fig. 5.6 shows the spatial distribution of FRM at $z = 0.1$. The typical value of FRM is ±200 rad m^{-2}, with high values concentrated in the cluster core region. Interestingly, the FRM map not only shows the small scale variations reminiscent of the ICM MHD turbulence, but also displays long, narrow filaments with dimensions of 300 kpc × 90 kpc. The FRM magnitudes and spatial distributions from simulations are quite consistent with observations of radio galaxies in clusters (Taylor & Perley, 1993; Eilek & Owen, 2002; Guidetti et al., 2008).

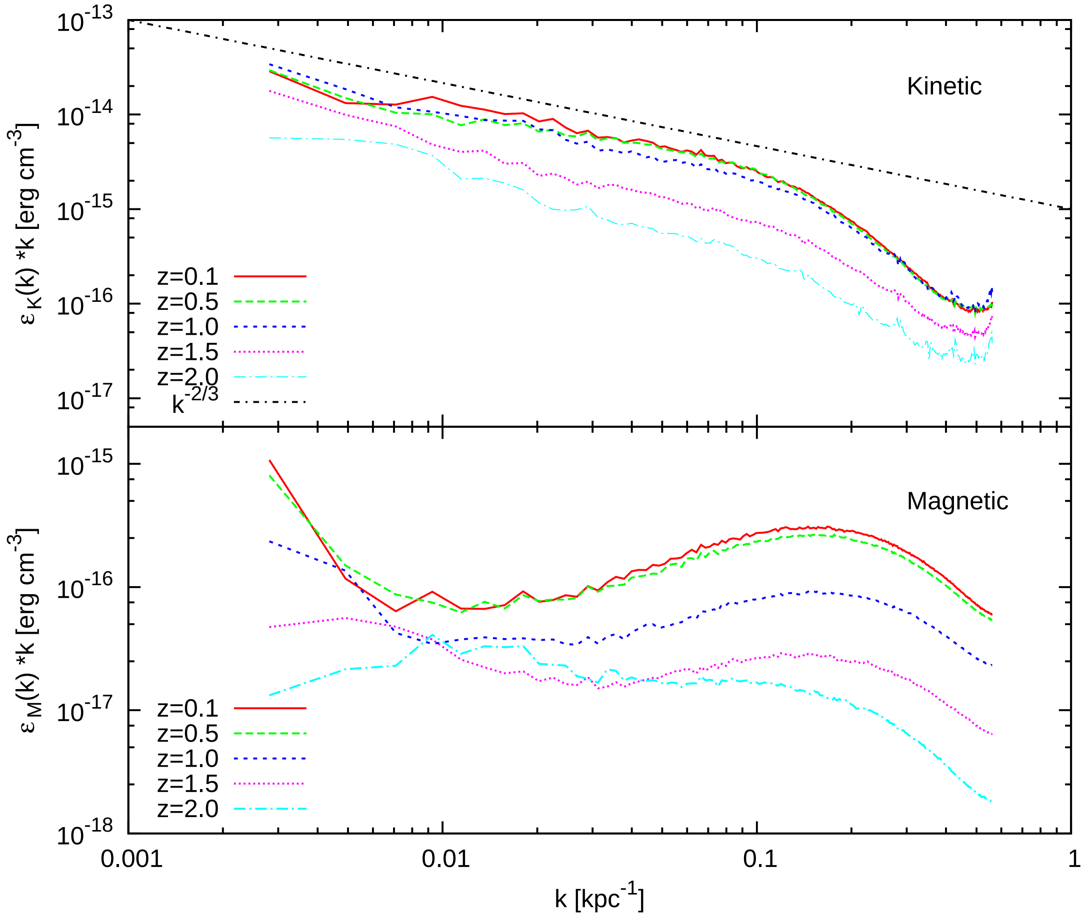

Figure 5.4: Power spectra of the kinetic energy density and magnetic energy density of the ICM at different epochs. The ICM turbulence is represented by the Kolmogorov-like spectra in kinetic energy. The magnetic energy is amplified via a dynamo process.

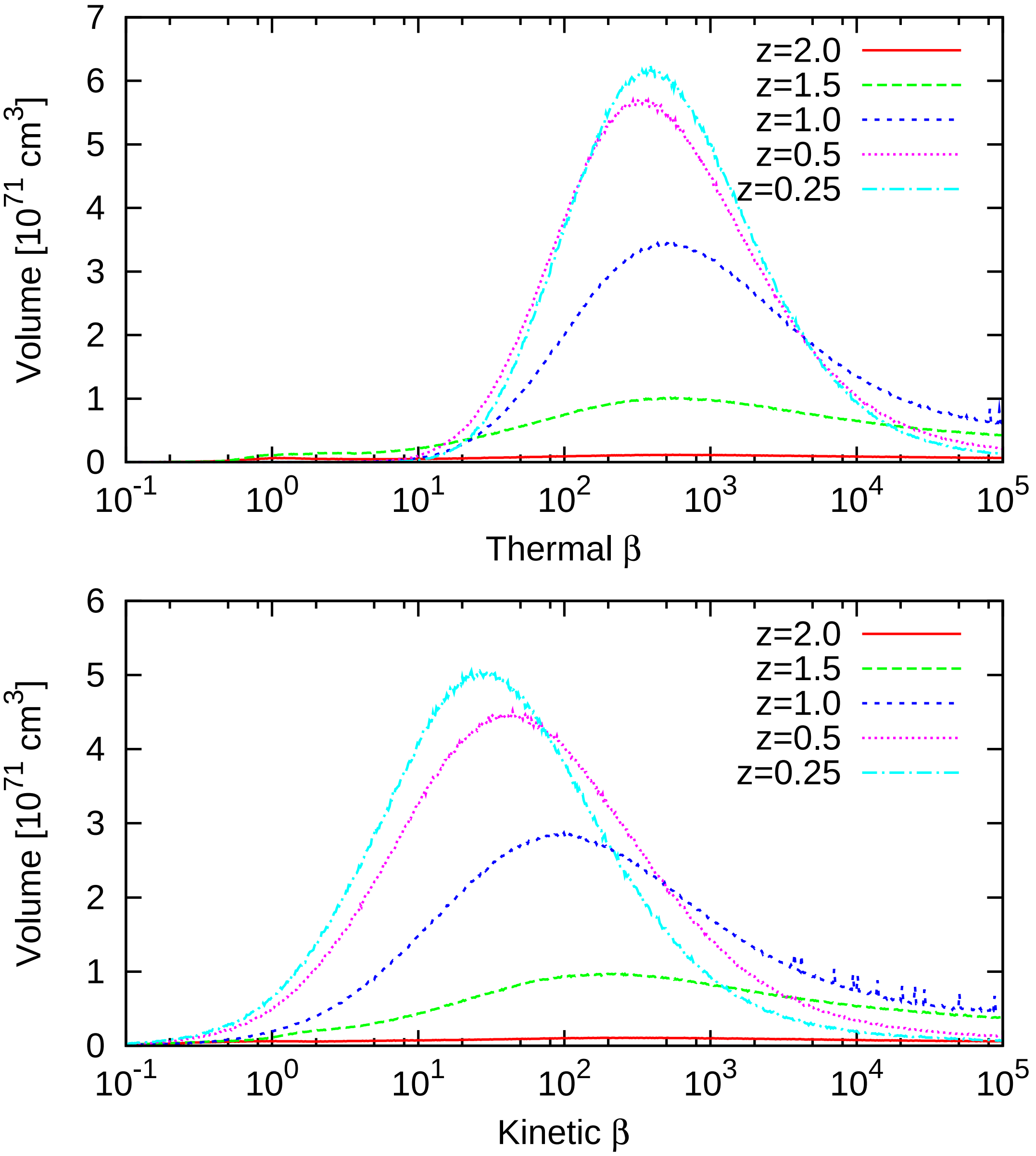

Figure 5.5: Thermal and kinetic β volume distributions at different redshifts. Thermal $\beta \equiv$ thermal energy density/magnetic energy density, and kinetic $\beta \equiv$ kinetic energy density/magnetic energy density. They are computed over cluster central sphere of 1 Mpc proper radius.

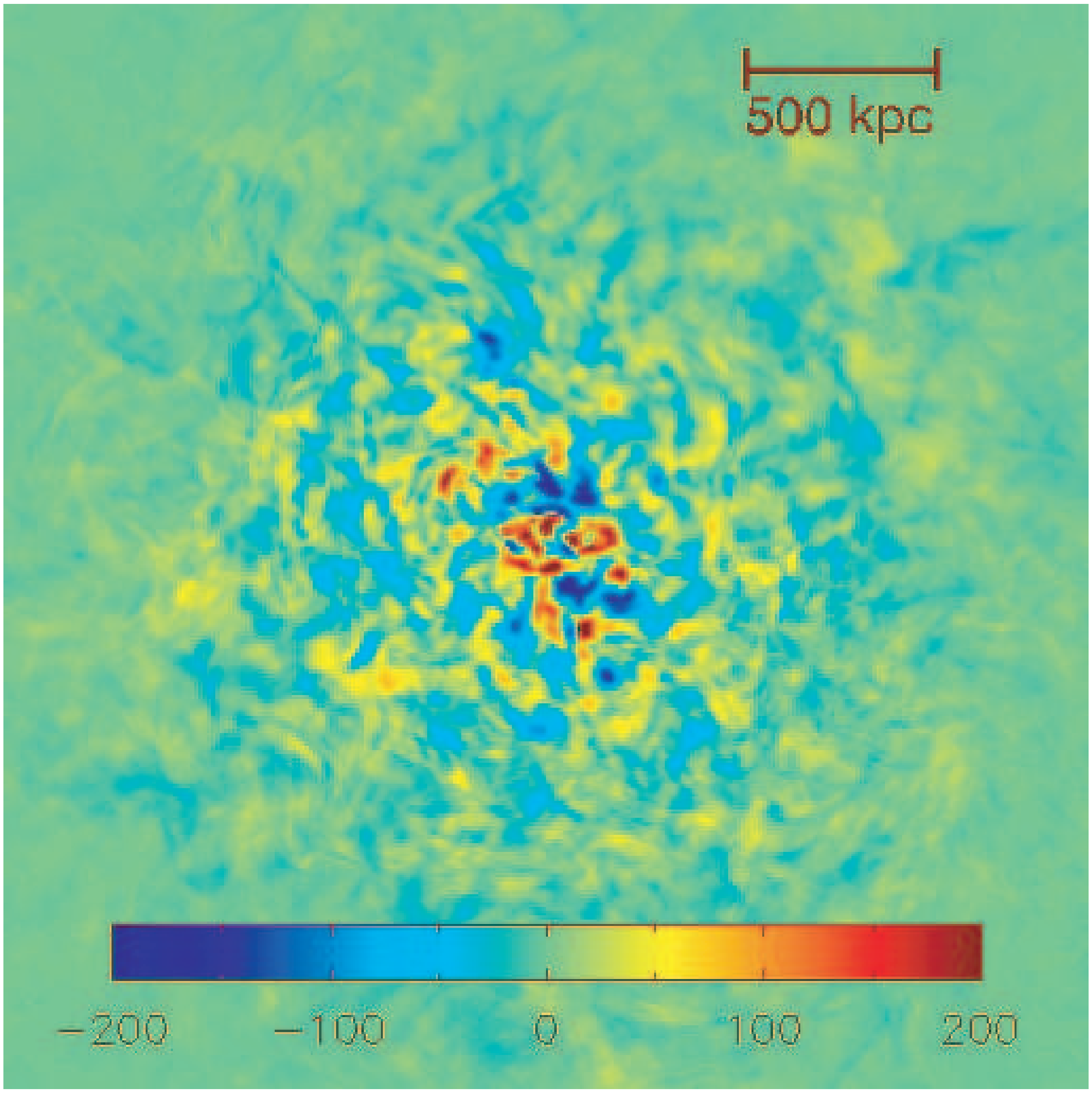

Figure 5.6: Faraday rotation measurement of the ICM by integrating to the mid-plane of the cluster. It covers a region of 2.86 Mpc × 2.86 Mpc (comoving) at z=0. The color range shown is from −200 (blue) to 200 (red) rad m^{-2}. The peak value of rotation measurement is about ±400 rad m^{-2}. Filamentary structures are quite common.

Table 5.1: Comparison of properties of clusters from simulations with and without magnetic field injection at z=0.

Parameter	No AGN	with AGN
$R_{vir}(Mpc)$	2.147	2.155
$M_{vir}(M_\odot)$	1.129e+15	1.143e+15
$M_{dm}(M_\odot)$	1.038e+15	1.051e+15
$M_{gas}(M_\odot)$	9.125e+13	9.166e+14
$T_{vir}(K)$	8.053e+07	8.116e+07

5.3.6 Impact of Magnetic Fields on Cluster Formation

At last, we would like to see how the cluster formation is affected in whole by the magnetic field injection. Table 5.1 compares the basic properties of simulated clusters with and without magnetic field injection. The cluster is almost unchanged by the additional magnetic fields as expected, since the magnetic energy is always very small comparing to the kinetic and thermal energy in the whole cluster (see Figure 5.5). Although the injected magnetic fields have big impact on the ambient of the AGN by forming bubbles and shocks in the early stage, the magnetic fields have little influence on the evolution of the whole cluster in the long term, which is dominated by dark matter dynamics. The magnetic fields should be more important in the cluster core regions, especially for the cool core clusters. We will not discuss this here because we don't include some necessary physical processes, such as radiative cooling, in our simulation.

5.4 Discussion

In this chapter, we present cluster formation simulation with magnetic energy injected in a local region to mimic magnetic feedback from AGN. We find that the injected magnetic fields are spread throughout the whole cluster by the cluster mergers. The magnetic fields are then amplified and maintained at small scale by the turbulence generated by the mergers and accretion shocks and at large scale by the bulk motions of mergers. The magnetic energy increases about 25 times. The final magnetic field strength is about 1-2 μG at the cluster core and drops slowly outward to just below 1 μG at half virial radius. These magnetic fields well resemble magnetic fields observed from RM. Since AGNs are commonly observed in galaxy clusters, one important implication of our studies is that the magnetic fields from AGNs alone are perhaps enough to "seed" the cluster and the ICM turbulence generated and maintained by mergers will amply and spread the AGN fields via a dynamo process. This is consistent with observations that clusters with large scale radio emissions are often correlated with cluster mergers (Feretti, 2005).

The magnetic energy is almost flat after ~ 6 Gyr. This could be because either the cluster become too relaxed to further amplify the magnetic fields or the magnetic fields are already strong enough to saturate with the turbulent motions. In the case with Biermann Battery effect in Chapter 3, the "tiny" magnetic energy keeps increasing till the end of the simulation. It implies that the cluster motions can still amplified small magnetic fields. Though these two simulations are from different initial conditions, the two clusters are relaxed similarly in the later time. We have another simulation also shows that the mangetic energy grows very slowly in the cluster studied in Chapter 3 for the final 5 Gyr when the magnetic fields are already at μG level. So, it is more likely that, in this simulation, the magnetic fields is already saturated with the ICM motions, and the saturated magnetic energy is about one twentieth of the kinetic energy.

Note that even though we have solved the ideal MHD equations, there is clearly numerical diffusion that has allowed the magnetic fields to diffuse in the ICM. The rate of diffusion is often related to the numerical Reynolds number and magnetic Reynolds number. We estimated that these numbers in our simulations are on the order of a few hundred (this is especially true in the cluster core region where most of the magnetic field energy resides). The small scale dynamo theory and simulations (Boldyrev & Cattaneo, 2004) have shown that the dynamo will grow under such conditions, which is consistent with our findings. The real ICM could have Reynolds number as low as ten (Reynolds et al., 2005), but its magnetic Reynolds number is less well determined, especially in a magnetized turbulent medium.

The results presented in this chapter need to be taken as an initial step in better understanding the evolution of AGN magnetic fields over the lifetime of a cluster.

The fact that the AGN magnetic fields are injected very early in the history of the cluster formation (i.e., z=3), before the major merger events, could be important. For AGN fields injected relatively late in the cluster formation as the case in the previous chapter. the magnetic fields may not experience extensive stretching and transport so that they could survive in a bubble morphology without undergoing significant mixing with the background ICM.

It is worth to perform the same cluster formation simulations with different injected magnetic energy to see whether the smaller initial magnetic fields will be amplified to the saturated level. Studying the impacts of different structures of injected magnetic fields and injections at different redshifts on the magnetic field evolution is also interesting. And it is very like that more than one AGNs happen during the course of cluster formation. We will study the multiple AGN injections in the near future. We will make synthetic observations (RM and Synchrotron) from our simulations and compare them to the observations, especially with the forthcoming results from EVLA.

Acknowledgments: This chapter, in part, is the material as it appears in the Astrophysical Journal, 2009. Xu, Hao; Li Hui; Collins, David C.; Li, Shengtai; Norman, Michael L., “Turbulence and Dynamo in Galaxy Cluster Medium : Implications on the Origin of Cluster Magnetic Fields”, IOP Publishing, 2009. The dissertation author was the primary investigator and author of this material.

Chapter 6

Summary and Future Work

6.1 Summary

Magnetic fields are important components of galaxy clusters. Even though intense research has been performed , fundamental questions concerning the origin and evolution of cluster magnetic fields remain unanswered. In this dissertation, we have used the adaptive mesh refinement cosmology magnetohydrodynamics code EnzoMHD to study the origin and evolution of magnetic fields in galaxy clusters, especially the case of seed fields from feedbacks of active galaxies.

Chapter 2 describes the EnzoMHD numerical method in detail and presents verifications of the code. Developed from Enzo, EnzoMHD keeps the basic hydro data structure, gravitational solver, cosmology expansion and other physical packages used in Enzo. In EnzoMHD, we use the PDE solver of Li et al. (2006) to solve the ideal MHD equations, which is second order accurate in both time and space. We use a slightly modified version of the AMR algorithm of Balsara (2001) to create interpolated fine grids and project the more accurate fine grid data to the cheaper coarse grid data. We have used the CT methods of Balsara & Spicer (1999) and Gardiner & Stone (2005) to advance the induction equation while maintaining the constraint $\nabla \cdot \mathbf{B} = 0$. The results of a broad array of tests are presented to demonstrate the accuracy of the code. It shows that EnzoMHD can handle the magnetic fields quite well while hydro variables are computed at an accuracy close to the original Enzo.

In chapter 3, we discuss magnetic fields generated from the Biermann battery mechanism in the large scale structure formation. We perform simulations of the formation of Population III stars and galaxy clusters including the Biermann battery effect. We show that in both cases very small magnetic fields will be created by the battery effect. In Population III star formation, we find that the tiny magnetic fields are amplified by both compression of magnetic fields falling into the star-forming halo with collapsing gas and stretching magnetic fields by the shear flows, and reach as large as 10^{-9} G in the center of the star-forming halo. In the case of galaxy cluster formation, we find that the magnetic field energy per unit mass increases by a factor of 10^3 in the cluster core region from z=3 to z=0. But the final fields are still much smaller ($\sim 10^{-18}$ G) than observations. The fields from Biermann battery effect are too small to be seed fields of galaxy cluster at the scale we studied.

Chapter 4 presents a study of the formation of X-ray cavities in galaxy cluster by Poynting-dominated jet/lobe injected by AGN. We simulated the injection of 6×10^{60} ergs of magnetic energy from an AGN into a galaxy cluster. We show the expansion of magnetic fields produce the bubbles as well as the shocks surrounding the bubbles, both of which resemble observations. We also show that about 80-90% of injected magnetic energy converts into potential and kinetic energy and in turn, heats the cluster core.

In chapter 5, we demonstrate how the magnetic fields from AGN feedback at high redshift can be used to magnetize the whole cluster to the observed level. We simulate cluster formation with AGN magnetic fields injected at z=3 with a new way to control the mesh refinement by magnetic field strength. We find that the local magnetic fields spread throughout the cluster by large scale flows induced by mergers and accretion. We also find that magnetic fields are further amplified and maintained by the stretching of turbulent flows driven by the continuous mergers and accretion shocks at smaller scales, and by bulk flows at large scales. At z=0, the strength of the magnetic field is a couple μG in the cluster core and dropping slowly outward to just below 1 μG at 1 Mpc away from the center, while the total magnetic energy increases by about 25 times. The radial profile of magnetic field strength from our simulation is similar to observations(Govoni et al., 2006; Guidetti et al., 2008).

The work presented in this thesis, as summarized in the previous paragraphs, contributes directly to a better understanding of the origin and evolution of magnetic fields in galaxy clusters. This work studied the magnetic fields from two proposed origins of magnetic fields in clusters, Biermann battery effect and AGN, and showed that AGN feedback may provide enough seed fields for the cluster magnetic fields. Since AGNs inject large amount of energy into the ICM and may regulate the cluster evolution, understanding interaction between AGN and ICM, in which magnetic fields may be important, is significant to the reseach on the formation of galaxy clusters. This work helps to understand magnetic field distribution and amplification in cluster environment. Magnetic fields are an important component of galaxy cluster evolution and observations, so understanding the evolution of cluster magnetic fields and their impact on cluster formation will help to better constrain cluster properties and, in turn, cosmological parameters in the effort to realize "precision cosmology".

6.2 Future Work

While the research presented in this dissertation has provided insights to the origin and evolution of magnetic fields in galaxy clusters, there is still work left to do. This entails improving our code in many respects, and futher enhancing its capability in handling more physical processes. The Population III star formation with Biermann battery effects (chapter 3) is limited by the lack of a proper treatment of radiation and chemistry at densities larger than 10^{10} cm^{-3}. In previous enzo simulations with pure hydrodynamics, higher density is achieved by implementing more chemical and cooling processes (Turk et al., 2008). We can also study magnetic fields at this higher density by installing those packages. But with higher density and lower temperature, the ionization factor should be even smaller and the ambipolar diffusion may become important, so properly handling ambipolar diffusion is also required. For the simulation of the Biermann battery in clusters, higher spatial resolution is essential to lower numerical resistivity. This will be discussed more later.

The study of magnetic bubble formation and evolution in chapter 4 is concentrated on the morphology of the bubbles and the energy evolution in general. Further research should study the distribution of injected energy in the ICM and the details of heating processes in the cluster core. To do this, a cluster with a cool core better resembling observations is required. This implies that more heating and/or cooling processes should be included in the simulations with better spatial resolution. These will be discussed in details in the next paragraph with AGN injected at high redshift.

Much work is needed to improve the study of evolution of magnetic fields from high redshift AGN presented in chapter 5. Better spatial resolution is very important. Observationally, the magnetic turbulence spectrum as well as other observation results are obtained through RMs at sub-kpc scale (Vogt & Enßlin, 2003; Govoni et al., 2006; Guidetti et al., 2008). To compare with them directly, we need to increase resolution in our simulations at lease one order of magnitude. In addition, the spatial resolution is important to study the amplification and saturation of magnetic fields. From the current simulations, we expect to observe energy equipartition between magnetic energy and kinetic energy at smaller scale if the resolution increase 10-fold. The energy equipartition may set the magnetic field saturation level.

In this research, we only injected magnetic fields from one AGN. Although the distribution of AGNs in clusters is still poorly understood (McNamara & Nulsen, 2007), we expect ~ 10 AGNs happened over a cluster lifetime based on the AGN luminosity function. Multiple AGN injections at different redshifts are interesting and will be studied in the future. This work is also related to the problem of heating the cool cores of galaxy clusters. Energetic AGNs are believed to be important sources of heating in the cluster. One possible reason that current simulations can't produce cool cores properly is because the AGN feedbacks are not included in the simulations correctly. The heating history is believed critical to the formation of cool core clusters (Voit, 2005). Both preheating the ICM by AGNs at high redshifts and heating cluster cores by recent AGNs should be important to reproduce the observations with simulations. So, in addition to the study of magnetic field evolution, we will study the details of the cooling and heating processes in our AGN feedback simulations.

Both viscosity and resistivity are important to this research, especially for the study of turbulence and dynamo processes. In current simulations, only the numerical viscosity and resistivity are involved in the computation, so the viscosity and resistivity are at the same level (magnetic Prandtl number is 1). In galaxy clusters, the magnetic Prandtl number may be quite large with large magnetic Reynold's number (Carilli & Taylor, 2002) but small Reynold's number (Reynolds et al., 2005). High magnetic Prandtl number may make the magnetic field evolution very different (Brandenburg & Subramanian, 2005). Simulations explicitly including viscosity and resistivity will be performed to study the influence of different viscosities and resistivites.

As mentioned many times in this section, higher resolution is essential for the further reseach, though we already used AMR to achieve pretty good resolutions with the computing resources we current have. Higher resolution is computationally very costly, needs much more computing cores and distributed memory. This will be made possible when next generation petaflop supercomputers, like Blue Water scheduled to be built at the NCSA, become available and provide much stronger computational ability in the coming several years. But our code is still not suited for the petaflop computering yet, which requires better parallelization and faster I/O of our code. In addition, it may also have difficulties on the data analysis and visualization. Further development of the code to make it more efficient and petaflop capable will start soon. Additionally, the possibility of porting our code to the newly developing hybrid supercomputers, like Roadrunner, will be studied.

Appendix A

Some Numerical Scheme and Procedures of EnzoMHD

A.1 AMR MHD Reconstruction

A.1.1 MHD Reconstruction

For completeness, we will briefly outline the AMR reconstruction used in EnzoMHD. The reader is encouraged to see the details in the original paper by Balsara (2001).

In this appendix, we have dropped the subscript f from the face centered fields, as the face centered field is the only one in question.

Balsara's reconstruction method for the magnetic field is a 3 dimensional, quadratic reconstruction of all 3 vector fields simultaneously. If we let $\mathbf{b}$ be the polynomial fit to the discrete face centered field field B, the general reconstruction is

$$b_x(x,y,z) = a_0 + a_x x + a_y y + a_z z + a_{xx} x^2 + a_{xy} xy + a_{xz} xz \tag{A.1}$$

$$b_y(x,y,z) = b_0 + b_x x + b_y y + b_z z + b_{xy} xy + b_{yy} y^2 + b_{yz} yz \tag{A.2}$$

$$b_z(x,y,z) = c_0 + c_x x + c_y y + c_z z + c_{xz} xz + c_{yz} yz + c_{zz} z^2 \tag{A.3}$$

The coefficients are found by the following constraints:

1. The analytic reconstruction should be divergence free.

2. At the faces of the parent cell, the reconstruction should reduce to a bilinear reconstruction, where the slopes are monotonized with the minmod slope limiter. For instance,

   $$b_x(x=\frac{\Delta x}{2},y)=B_{x,i+\frac{1}{2},j,k}+\frac{\Delta_y B_{x,i+\frac{1}{2}}}{\Delta y}y+\frac{\Delta_z B_{x,i+\frac{1}{2}}}{\Delta z}z \tag{A.4}$$

   where

   $$\Delta_y B_{x,i+\frac{1}{2}}=minmod(B_{x,i+\frac{1}{2},j+1}-B_{x,i+\frac{1}{2},j},B_{x,i+\frac{1}{2},j}-B_{x,i+\frac{1}{2},j-1}) \tag{A.5}$$

   $$minmod(x,y)=\begin{cases} x, & |x|<|y| \text{ and } xy>0 \\ y, & |y|<|x| \text{ and } xy>0 \\ 0, & xy<0 \end{cases} \tag{A.6}$$

The *minmod* slope is used in order to minimize oscillations. Area weighted averages over these polynomials are then used to assign the fine grid values.

Often, a fine grid patch will encroach on unrefined territory. This results in the refinement of coarse zones that a.) share a face with fine grids but b.) don't have corresponding fine grids of their own. Balsara refers to this as "Prolongation" of the fine grid. To avoid generating any divergence at the boundary of the face, the interpolation polynomials need to match the old fine data. The interpolation equations above (eqns A.1 - A.3) do not have enough degrees of freedom to accommodate that many data points. In this case, Balsara describes a new polynomial that DOES have enough degrees of freedom, by adding 3^{rd} order cross terms to equations A.1 - A.3:

$$\begin{aligned} b_x(x,y,z)=&a_0+a_xx+a_yy+a_zz+a_{xx}x^2+a_{xy}xy+a_{xz}xz \\ &+a_{yz}yz+a_{xyz}xyz+a_{xxz}x^2z+a_{xxy}x^2y \end{aligned} \tag{A.7}$$

$$\begin{aligned} b_y(x,y,z)=&b_0+b_xx+b_yy+b_zz+b_{xy}xy+b_{yy}y^2+b_{yz}yz \\ &+b_{xz}xz+b_{yyz}y^2z+b_{xyz}xyz+b_{xyy}xy^2 \end{aligned} \tag{A.8}$$

$$\begin{aligned} b_z(x,y,z)=&c_0+c_xx+c_yy+c_zz+c_{xz}xz+c_{yz}yz+c_{zz}z^2 \\ &+c_{xy}xy+c_{yzz}yz^2++c_{xzz}xz^2+c_{xyz}xyz \end{aligned} \tag{A.9}$$

The yet undetermined coefficients are found by matching the polynomial to a bilinear fit on the face:

$$b(x = \frac{\Delta x}{2}, y, z) = B_{x,i+\frac{1}{2},j,k} + \frac{\Delta_y B_{x,i+\frac{1}{2}}}{\Delta y} y + \frac{\Delta_z B_{x,i+\frac{1}{2}}}{\Delta z} z + \frac{\Delta_{yz} B_{x,i+\frac{1}{2}}}{\Delta y \Delta z} yzp \tag{A.10}$$

and now the finite differences are taken from the finest grid:

$$\begin{aligned} \Delta_{yz} B_{x,i+\frac{1}{2}} = 4((&B_{x,i+\frac{1}{2},j+\frac{1}{2},k+\frac{1}{2}} - B_{x,i+\frac{1}{2},j-\frac{1}{2},k+\frac{1}{2}}) - \\ &(B_{x,i+\frac{1}{2},j+\frac{1}{2},k-\frac{1}{2}} - B_{x,i+\frac{1}{2},j-\frac{1}{2},k-\frac{1}{2}})) \end{aligned} \tag{A.11}$$

$$\begin{aligned} \Delta_{y} B_{x,i+\frac{1}{2}} = ((&B_{x,i+\frac{1}{2},j+\frac{1}{2},k+\frac{1}{2}} - B_{x,i+\frac{1}{2},j-\frac{1}{2},k+\frac{1}{2}}) + \\ &(B_{x,i+\frac{1}{2},j+\frac{1}{2},k-\frac{1}{2}} - B_{x,i+\frac{1}{2},j-\frac{1}{2},k-\frac{1}{2}})) \end{aligned} \tag{A.12}$$

where B is the field on the fine grid. Note that since this is now a centered difference, the minmod slope limiter is not used.

A.1.2 Implementation in Enzo

In order to avoid complicated book keeping routines to determine which cells are being prolonged into, and from which direction, we formulate only one interpolation polynomial, given by equations A.7-A.9. The necessary finite differences for a given refinement region are taken from the finest data available, as in equations A.11 and A.12. The last four terms in each reconstruction polynomial are there exclusively to ensure consistency of Old Fine Grid Data, so for faces that have no Fine Data before the reconstruction, these are set to zero. Since the reconstruction polynomial exactly matches the old fine grid data, this also eliminates the need to copy the old fine grid data to the newly refined patch.

A.2 Flux Correction

At any given time in an AMR simulation, there are points in space that are described by more than one data structure. In a finite volume hydro calculation, with cell centered data fields, this occurs at the boundary between coarse and fine grids in the Flux fields, $\vec{F}$. In an AMR MHD calculation, with face centered magnetic fields, this occurs at the same boundary, in the face centered magnetic field, and the edge centered electric field. Ensuring consistency between data is vital for the conservation of quantities like mass, energy, momentum, and $\nabla \cdot \mathbf{B}$. Flux Correction is essential for this consistency.

A.2.1 Conservation Form

It is useful to briefly describe the basic formulation of the methods used in Enzo and EnzoMHD before moving on to the flux correction mechanism.

Any conservative system, such as ideal MHD, can be written in a differential form as

$$\frac{\partial V}{\partial t} + \nabla \cdot F = 0 \tag{A.13}$$

where V and F are suitably defined, in our case by 2.24 and 2.25. Here we ignore any source terms.

In finite volume methods, we store average quantities of V and F, and re-write the conservation law in Conservation Form, using the Fundamental Theorem and Stokes Theorem. Starting with eqn A.13, and integrating, we get:

$$\int_t^{t+\Delta t} \int_V \frac{\partial V}{\partial t} dV dt = -\int_t^{t+\Delta t} \int_A F \cdot dA dt \tag{A.14}$$

where the volume V is taken from the point (x, y, z) to $(x + \Delta x, y + \Delta y, z + \Delta z)$. Now let

$$\hat{V}^n = \frac{1}{\Delta V} \int_V V(x, y, z, t^n) dV \tag{A.15}$$

$$\tilde{F}_{x,I+\frac{1}{2},J,K} = \frac{1}{\Delta y \Delta x} \int_{\Delta y, \Delta z} F(x = I + \frac{1}{2}, y, z) \cdot \hat{x} dy dz \tag{A.16}$$

where $\hat{x}$ is the unit vector in the x direction. Similar definitions apply $\tilde{F}_y$ and $\tilde{F}_z$, and

$$\hat{F}_x = \frac{1}{\Delta t} \int_{\Delta t} \tilde{F}_x dt \tag{A.17}$$

The averaging here was taken explicitly in two steps to emphasize that Δx,Δy and Δz are possibly functions of t, as the are in cosmological hydrodynamics. Putting this all together, we get the equations in their final analytical form before discretization (also the last form we'll be using here)

$$\begin{aligned}\hat{V}^{n+1}_{I,J,K} = \hat{V}^{n}_{I,J,K} - \Delta t(&\frac{1}{\Delta x}(\hat{F}_{x,I+\frac{1}{2},J,K} - \hat{F}_{x,I-\frac{1}{2},J,K})+ \\ &\frac{1}{\Delta y}(\hat{F}_{y,I,J+\frac{1}{2},K} - \hat{F}_{y,I,J-\frac{1}{2},K})+ \\ &\frac{1}{\Delta z}(\hat{F}_{z,I,J,K+\frac{1}{2}} - \hat{F}_{z,I,J,K-\frac{1}{2}}))\end{aligned} \tag{A.18}$$

Note that equation A.18 is an exact equation, since only averages and the fundamental theorem of calculus have been used up to this point. The trick in finite volume methods such as our MHD is finding appropriate approximations to $\hat{F}$ that are both accurate and stable.

A.2.2 Conservation Form and AMR: Enter Flux Correction

As mentioned at the beginning of the section, an AMR simulation has multiple data structures representing a single point in space. In entirely cell centered codes such as PPM, the only such instance is at the surface of a fine grid boundary, where both the fine grid and coarse grid represent the flux at that point. Moreover, after the fine grid field is projected into the coarse, there's a mismatch on the coarse grid itself as to the value of the flux at the surface. The value of that discrepancy can be easily found. After the projection, a coarse grid at a point (I, J) has the value (restricting to 2d, for clarity)

$$\hat{V}^{n+1}_{I,J} = \sum_{\substack{i=I\pm\frac{1}{4}\\ j=J\pm\frac{1}{4}}} \hat{q}^{n+1}_{i,j} \tag{A.19}$$

where lower case quantities denote the value of the fine grid data. Expanding the time update for $\hat{q}^{n+1}$ in space and time, we find that

$$\hat{V}^{n+1}_{I,J} = \sum_{\substack{i=I\pm\frac{1}{4}\\ j=J\pm\frac{1}{4}}} \hat{q}^{n}_{i,j} - (\sum_{m=n}^{n+1} \sum_{x,j=J\pm\frac{1}{4}} \frac{\Delta t^m}{\Delta V^m} \hat{f}^m_{I+\frac{1}{2},j} + \quad - \sum_{m=n}^{n+1} \sum_{x,j=J\pm\frac{1}{4}} \frac{\Delta t^m}{\Delta V^m} \hat{f}^m_{I-\frac{1}{2},j}) \tag{A.20}$$

$$-(y \text{ and } z \text{ terms})$$

By construction of the interpolation polynomial (and projection at the last timesteps) the first term is just equal to $\hat{V}^n_{I,J}$, which means that, by equation A.18 $\hat{V}_{I,J}$ effectively sees, at the point $I + \frac{1}{2}$,

$$\frac{\Delta t}{\Delta V}\hat{F}_x = \sum_{m=n}^{n+1} \sum_{x,j=J\pm\frac{1}{4}} \frac{\Delta t^m}{\Delta V^m} \hat{f}^m_{I+\frac{1}{2},j} :=< f_x > \tag{A.21}$$

However, for the cell $(I-1, J)$, which has no corresponding fine grid flux, $\hat{F}_{I+\frac{1}{2}}$ come from the discretization method on the coarse grid. There is absolutely no reason for the two to match, so we have a discrepancy in the descriptions of the data. This can be solved by simply replacing the less refined data that $\hat{V}_{I+1,J}$ used with the more refined average, given by equation A.21:

$$\hat{V}_{I+1,J,_{fc}} = \hat{V}_{I+1,J} + \frac{\Delta t}{\Delta V}\hat{F}_{x,I+\frac{1}{2},J} - \sum_m \sum_j \frac{\Delta t^m}{\Delta V^m} \hat{f}^m_{x,I+\frac{1}{2},j} \tag{A.22}$$

Now every place $\hat{F}_{x,I,J}$ show up in our method, the exact same approximation is used.

A.2.3 Flux Correction and MHD

A similar formalism to that described in A.2.1 is used for to advance the magnetic fields in EnzoMHD, but instead of using volume averages, we use area averages. The magnetic evolution is given by the induction equation:

$$\frac{\partial \vec{B}}{\partial t} = -\nabla \times \vec{E} \tag{A.23}$$

When discretized, equation A.23 yields the equation

$$\begin{aligned}\hat{B}^{n+1}_{x,I+\frac{1}{2},J} = \hat{B}^{n}_{x,I+\frac{1}{2},J} - \frac{\Delta t}{\Delta y \Delta z}(\Delta z(\hat{E}_{z,I+\frac{1}{2},J+\frac{1}{2},K} - \hat{E}_{z,I+\frac{1}{2},J-\frac{1}{2},K}) +& \\ \Delta y(\hat{E}_{y,I+\frac{1}{2},J,K+\frac{1}{2}} - \hat{E}_{y,I+\frac{1}{2},J,K-\frac{1}{2}}))&\end{aligned} \tag{A.24}$$

where

$$\hat{B}^n_{x,I+\frac{1}{2},J,K} = \frac{1}{\Delta y \Delta z}\int_A \vec{B}(x = I + \frac{1}{2}, y, z, t^n) \cdot \hat{x} dy dz \tag{A.25}$$

$$\hat{E}^n = \frac{1}{\Delta t}\int_t^{t+\Delta t} \frac{1}{\Delta x}\int_x \vec{E} \cdot dl dt \tag{A.26}$$

which is also exact, and the main problem is finding a suitable approximation for $\hat{E}$.

Again, after the area-weighted projection of the fine grid field $\hat{b}_x$ into the coarse grid $\hat{B}_x$, there's a discrepancy between the electric field at a refined point on the surface of a refined grid, as it's seen by both grids that have subgrids and grids that don't. In Balsara (2001), he suggests a similar flux correction mechanism to that of the standard hydro, described in A.2.2. However, due to an issue with the initial implementation of flux correction in Enzo (which has since been fixed) and ease of computational logic, we chose a different route. In EnzoMHD, instead of projecting fine grid magnetic fields into coarse magnetic fields and then correcting zones in the coarse grid, we project the electric field and then take the curl of the entire coarse grid. Thus, all coarse grid magnetic fields see the most accurate data at the same time, and no a-posteriori correction needs to be done. Where there are no subgrids, the coarse grid sees an electric field that comes from the CT module in section 2.2.7, and where there are subgrids it sees

$$\begin{aligned}\hat{E}^n_{z,i-\frac{1}{2},j-\frac{1}{2},k} = &\frac{\Delta t^n}{\Delta t}(e^{n+\frac{1}{2}}_{z,i-\frac{1}{2},j-\frac{1}{2},k-\frac{1}{4}} + e^{n+\frac{1}{2}}_{z,i-\frac{1}{2},j-\frac{1}{2},k+\frac{1}{4}}) + \\ &\frac{\Delta t^{n+\frac{1}{2}}}{\Delta t}(e^{n+\frac{3}{4}}_{z,i-\frac{1}{2},j-\frac{1}{2},k-\frac{1}{4}} + e^{n+\frac{3}{4}}_{z,i-\frac{1}{2},j-\frac{1}{2},k+\frac{1}{4}})\end{aligned} \tag{A.27}$$

While a complete flux correction treatment would potentially save on memory and flops, in practice the extra memory is negligible compared to the total memory and time used by the rest of Enzo, and the extra floating point operations done here are offset by increase cache utilization of the data, as the entire grid is done in a single stride one sweep instead of an essentially random access pattern.

As described in section 2.2.5, some of the subgrids get their boundary conditions updated from the parent zones. Because of this, the curl of the magnetic field is actually taken twice. The first time is done immediately after the hyperbolic update, in order to ensure that the parent zones are up to date for the interpolation of the ghost zones of the subgrids that need it. The second time is after the subgrids project their electric field to the parent, to ensure maximal accuracy of the parent grids. This additional call takes negligible time, as the curl has relatively few operations. See appendix A.3 for the details of this order of operations.

A.3 Schematic for the Cosmological MHD Code

In this appendix, we present a schematic of the MHD code, for clarity and easy reference.

Step 0.– We start with conserved quantities density, total energy, and momentum ($\rho^n_{BM}, E^n_{total}, \mathbf{p}^n_{BM}$), and primitive quantities velocity and gas pressure (v^n_{BM}, P^n_{gas}) for the baryonic matter; face and cell centered magnetic fields (B^n_c, B^n_f); and Lagrangian dark matter mass, position, and velocity ($\rho^n_{DM}, \mathbf{x}^n, \mathbf{v}^n_{DM}$). These are all at time t^n. Where needed, primitive quantities will be described by $U = (\rho_{BM}, P_{gas}, \mathbf{v}_{BM}, \mathbf{B})$, and conserved quantities by $V = (\rho_{BM}, E_{total}, \mathbf{p}_{BM}, \mathbf{B})$. Conversion between the two is done as needed.

Step 1. Solve Poisson's equation for the acceleration field at $t^{n+\frac{1}{2}}$

$$\phi^n \Longleftarrow \rho^n_{BM} + \rho^n_{DM} \tag{A.28}$$

$$\phi^{n+1/2} = \phi^n\left(1 + \frac{\Delta t^n}{2\Delta t^{n-1}}\right) - \phi^{n-1}\frac{\Delta t^n}{2\Delta t^{n-1}} \tag{A.29}$$

$$g_i^{n+1/2} = \frac{1}{2a^{n+1/2}\delta x_i}\left(\phi_{i+1}^{n+1/2} - \phi_{i-1}^{n+1/2}\right) \tag{A.30}$$

Step 2.– Update particle positions and velocities. (Strictly speaking, this happens after the Expansion step, but the narrative works better if it's here.)

$$\mathbf{v}_{DM}^{n+1/2} = \mathbf{v}^n_{DM} - \frac{\Delta t^n}{2}\frac{\dot{a}^{n+1/2}}{a^{n+1/2}}\mathbf{v}^n_{DM} - \frac{\Delta t^n}{2}\mathbf{g}^{n+1/2} \tag{A.31}$$

$$\mathbf{x}^{n+1}_{DM} = \mathbf{x}^n_{DM} + \Delta t^n\left(\mathbf{v}^{n+1/2}_{i,DM}/a^{n+1/2}\right) \tag{A.32}$$

$$v^{n+1}_{i,DM} = v^{n+1/2}_{i,DM} - -\frac{\Delta t^n}{2}\frac{\dot{a}^{n+1/2}}{a^{n+1/2}}v^{n+1/2}_{i,DM} - \frac{\Delta t^n}{2}g_i^{n+1/2} \tag{A.33}$$

Step 3.– Apply half of the gravitational and expansion update to the fields that require it, to obtain the temporary state $\tilde{U} = (\rho, \tilde{P}^n_{total}, \tilde{\mathbf{v}}^n_{BM}, \tilde{B}^n_c)$

$$\tilde{\mathbf{v}}^n_{BM} = \mathbf{v}^n_{BM} - \frac{\Delta t^n}{2}\frac{\dot{a}^n}{a^n}\mathbf{v}^n_{BM} - \frac{\Delta t^n}{2}\frac{1}{a^n}\mathbf{g}^{n+1/2} \tag{A.34}$$

$$\tilde{p}^n = p^n - \frac{\Delta t^n}{2}\frac{2\dot{a}^n}{a^n}p^n \tag{A.35}$$

$$\tilde{\mathbf{B}}^n_c = \mathbf{B}^n_c - \frac{\delta t^n}{4}\frac{\dot{a}^n}{a^n}\mathbf{B}_c \tag{A.36}$$

$$\tilde{U} = (\rho, \tilde{P}^n_{total}, \tilde{\mathbf{v}}^n_{BM}, \tilde{B}^n_c) \tag{A.37}$$

Step 4. Compute interface states at $i \pm \frac{1}{2}, n + \frac{1}{2}$ using linear spatial reconstruction and second order time integration:

$$U^{n+\frac{1}{2}}_{i+\frac{1}{2},L}, U^{n+\frac{1}{2}}_{i+\frac{1}{2},R} \Longleftarrow \tilde{U}_{i-1}, \tilde{U}_i, \tilde{U}_{i+1}, \tilde{U}_{i+2} \tag{A.38}$$

Step 5. Compute approximation of the flux in equation 2.25 at the interface $i + \frac{1}{2}$. This is done by solving the Riemann problem using one of the solvers mentioned in section 2.2.6

$$\hat{F}^{n\frac{1}{2}}_{i+\frac{1}{2}} = Riemann(U^{n+\frac{1}{2}}_{i+\frac{1}{2},L}, U^{n+\frac{1}{2}}_{i+\frac{1}{2},R}) \tag{A.39}$$

Step 6. Update the conserved quantities with the new fluxes:

$$(V_i^{n+1})_{MHD} = V_i^n - \frac{\Delta t}{\Delta x}[\hat{F}_{i+\frac{1}{2}} - \hat{F}_{i-\frac{1}{2}}] \tag{A.40}$$

Step 7. Compute Electric field from Fluxes

$$E^{n+\frac{1}{2}}_{i+\frac{1}{2},j+\frac{1}{2}} \Longleftarrow \hat{F}_{i+\frac{1}{2}} \tag{A.41}$$

Step 9. Update magnetic fields from electric fields for the first time.

$$B_f^{n+1} = B_f^n - \frac{\Delta t}{a} \nabla \times E^{n+\frac{1}{2}}_{i+\frac{1}{2},j+\frac{1}{2}} \tag{A.42}$$

Step 8.–Gravitational step for the baryonic matter, with time centered density

$$(\mathbf{p}^{n+1}_{i,BM})_{MHD,Grav} = (\mathbf{p}^{n+1}_{i,BM})_{MHD} - \Delta t^n \frac{(\rho^n + \rho^{n+1}_{MHD})}{2} g_i^{n+1/2} \tag{A.43}$$

Step 9.–Expansion step for the baryonic matter,

$$(\mathbf{v}^{n+1}_{BM})_{MHD,Grav,exp} = \frac{1 - (\Delta t^n/2)(\dot{a}^{n+1/2}/a^{n+1/2})}{1 + (\Delta t^n/2)(\dot{a}^{n+1/2}/a^{n+1/2})} (\mathbf{v}^{n+1}_{BM})_{MHDGrav} \tag{A.44}$$

$$p^{n+1} = \frac{1 - (\Delta t^n)(\dot{a}^{n+1/2}/a^{n+1/2})}{1 + (\Delta t^n)(\dot{a}^{n+1/2}/a^{n+1/2})} (p^{n+1})_{MHD} \tag{A.45}$$

Step 10. Recurse to finer grids. Integrate fine grids from t^n to t^{n+1}

$$V^{n+1}_{FineGrids} \Longleftarrow V^n_{FineGrids} \tag{A.46}$$

Step 11.–Flux correction step for conserved baryon field quantities

$$V^{n+1}_{MHD,Grav,exp,fc} \Longleftarrow (\hat{F}^{n+1/2}), (\hat{F}^{n+1/2})_{FineGrids}, V^{n+1}_{MHDGrav,exp} \tag{A.47}$$

Step 12.–Project conserved baryon field quantities and electric field from fine grids to coarse grids. This is done *after* the flux correction step to avoid any bookkeeping errors. The average is taken over Δt^n and the surface of each $FineGrid$.

$$
\begin{aligned}
V^{n+1}_{ParentGrid} &= \; < V^{n+1}_{FineGrid} >_{t,surface} && \text{(A.48)}\\
E^{n+\frac{1}{2}}_{ParentGrid} &= \; < E^{n+\frac{1}{2}}_{FineGrid} >_{t,surface} && \text{(A.49)}
\end{aligned}
$$

Step 13. Update magnetic fields from electric fields for the final time.

$$
B^{n+1}_f = B^n_f - \frac{\Delta t}{a}\nabla \times E^{n+\frac{1}{2}}_{ParentGrid} \tag{A.50}
$$

Step 14. Apply expansion to the Face Centered Fields

$$
B^{n+1}_{f,exp} = \frac{1-(\Delta t^n/4)(\dot{a}^{n+1/2}/a^{n+1/2})}{1+(\Delta t^n/4)(\dot{a}^{n+1/2}/a^{n+1/2})}(B^{n+1}_f) \tag{A.51}
$$

Step 15. Compute cell centered magnetic field from face centered (with the expansion subscript from step 9 dropped for clarity)

$$
\begin{aligned}
B^{n+1}_{c,x,i,j,k} &= 0.5 * (B_{f,x,i+\frac{1}{2},j,k} + B_{f,x,i-\frac{1}{2},j,k})\\
B^{n+1}_{c,y,i,j,k} &= 0.5 * (B_{f,y,i,j+\frac{1}{2},k} + B_{f,y,i,j-\frac{1}{2},k})\\
B^{n+1}_{c,z,i,j,k} &= 0.5 * (B_{f,z,i,j,k+\frac{1}{2}} + B_{f,z,i,j,k-\frac{1}{2}})
\end{aligned} \tag{A.52}
$$

Step 16. We have now finished an update of this level. Rebuild the hierarchy from this level down.

$$
\begin{aligned}
V^{n+1}_{New\ FineGrids} &\Longleftarrow V^{n+1} && \text{(A.53)}\\
B^{n+1}_{f,New\ FineGrids} &\Longleftarrow B^{n+1}_f && \text{(A.54)}
\end{aligned}
$$

Acknowledgments: This appendix, in full, has been submitted for publication of the material as it may appear in the Astrophysical Journal Supplement Series, 2009. Collins, David C.; Xu, Hao; Norman, Michael L.; Li, Hui; Li, Shengtai, “Cosmological AMR MHD with Enzo”, IOP Publishing, 2009. The dissertation author was the primary investigator and author of this paper.

Bibliography

Abel, T., Anninos, P., Zhang, Y., & Norman, M. L. 1997, New Astronomy, 2, 181

Abel, T., Bryan, G. L., & Norman, M. L. 2000, ApJ, 540, 39

—. 2002, Science, 295, 93

Anninos, P., Zhang, Y., Abel, T., & Norman, M. L. 1997, New Astronomy, 2, 209

Anninos, W. Y., & Norman, M. L. 1994, ApJ, 429, 434

Balsara, D. S. 2001, Journal of Computational Physics, 174, 614

Balsara, D. S., & Kim, J. 2004, ApJ, 602, 1079

Balsara, D. S., & Spicer, D. S. 1999, Journal of Computational Physics, 149, 270

Bardeen, J. M., Bond, J. R., Kaiser, N., & Szalay, A. S. 1986, ApJ, 304, 15

Battaner, E., & Lesch, H. 2000, ArXiv Astrophysics e-prints: astro-ph/0003370

Baym, G., Bödeker, D., & McLerran, L. 1996, Phys. Rev. D, 53, 662

Berger, M. J., & Colella, P. 1989, Journal of Computational Physics, 82, 64

Bernet, M. L., Miniati, F., Lilly, S. J., Kronberg, P. P., & Dessauges-Zavadsky, M. 2008, Nature, 454, 302

Biermann, L. 1950, Z. Naturforsch., 5A, 65

Binney, J., & Merrifield, M. 1998, Galactic astronomy (Princeton University Press, Princeton)

Binney, J., & Tabor, G. 1995, MNRAS, 276, 663

Blandford, R. D. 1976, MNRAS, 176, 465

Blanton, E. L., Sarazin, C. L., McNamara, B. R., & Wise, M. W. 2001, ApJ, 558, L15

Boldyrev, S., & Cattaneo, F. 2004, Phys. Rev. Lett., 92, 144501

Brackbill, J. U., & Barnes, D. C. 1980, Journal of Computational Physics, 35, 426

Brandenburg, A., & Subramanian, K. 2005, Phys. Rep., 417, 1

Brio, M., & Wu, C. C. 1988, Journal of Computational Physics, 75, 400

Bromm, V., Coppi, P. S., & Larson, R. B. 2002, ApJ, 564, 23

Bromm, V., & Larson, R. B. 2004, ARA&A, 42, 79

Brüggen, M., & Kaiser, C. R. 2002, Nature, 418, 301

Bryan, G. L., Machacek, M., Anninos, P., & Norman, M. L. 1999, ApJ, 517, 13

Bryan, G. L., & Norman, M. L. 1998, ApJ, 495, 80

Bryan, G. L., Norman, M. L., Stone, J. M., Cen, R., & Ostriker, J. P. 1995, Comp. Phys. Comm, 89, 149

Burbidge, G. R. 1959, ApJ, 129, 849

Carilli, C. L., & Taylor, G. B. 2002, ARA&A, 40, 319

Cen, R., & Ostriker, J. P. 1993, ApJ, 417, 404

Churazov, E., Brüggen, M., Kaiser, C. R., Böhringer, H., & Forman, W. 2001, ApJ, 554, 261

Ciardi, B., & Ferrara, A. 2005, Space Science Reviews, 116, 625

Colella, P., & Glaz, H. M. 1985, Journal of Computational Physics, 59, 264

Colella, P., & Woodward, P. R. 1984, Journal of Computational Physics, 54, 174

Colgate, S. A., Li, H., & Pariev, V. 2001, Phys. Plasmas, 8, 2425

Croston, J. H., Hardcastle, M. J., Harris, D. E., Belsole, E., Birkinshaw, M., & Worrall, D. M. 2005, ApJ, 626, 733

Dalla Vecchia, C., Bower, R. G., Theuns, T., Balogh, M. L., Mazzotta, P., & Frenk, C. S. 2004, MNRAS, 355, 995

Daly, R. A., & Loeb, A. 1990, ApJ, 364, 451

Davies, G., & Widrow, L. M. 2000, ApJ, 540, 755

De Young, D. S. 1992, ApJ, 386, 464

Dedner, A., Kemm, F., Kröner, D., Munz, C.-D., Schnitzer, T., & Wesenberg, M. 2002, Journal of Computational Physics, 175, 645

Diehl, S., Li, H., Fryer, C. L., & Rafferty, D. 2008, ApJ, 687, 173

Dolag, K., Bartelmann, M., & Lesch, H. 1999, A&A, 348, 351

—. 2002, A&A, 387, 383

Donnert, J., Dolag, K., Lesch, H., & Müller, E. 2009, MNRAS, 392, 1008

Dubois, Y., & Teyssier, R. 2008, A&A, 482, L13

Eilek, J. A., & Owen, F. N. 2002, ApJ, 567, 202

Eisenstein, D. J., & Hu, W. 1999, ApJ, 511, 5

Elbert, J. W., & Sommers, P. 1995, ApJ, 441, 151

Evans, C. R., & Hawley, J. F. 1988, ApJ, 332, 659

Evrard, A. E. 1990, ApJ, 363, 349

Fabian, A. C., Sanders, J. S., Crawford, C. S., Conselice, C. J., Gallagher, J. S., & Wyse, R. F. G. 2003, MNRAS, 344, L48

Fabian, A. C., Sanders, J. S., Ettori, S., Taylor, G. B., Allen, S. W., Crawford, C. S., Iwasawa, K., Johnstone, R. M., & Ogle, P. M. 2000, MNRAS, 318, L65

Fan, X., Narayanan, V. K., Lupton, R. H., Strauss, M. A., Knapp, G. R., Becker, R. H., White, R. L., Pentericci, L., Leggett, S. K., Haiman, Z., Gunn, J. E., Ivezić, Ž., Schneider, D. P., Anderson, S. F., Brinkmann, J., Bahcall, N. A., Connolly, A. J., Csabai, I., Doi, M., Fukugita, M., Geballe, T., Grebel, E. K., Harbeck, D., Hennessy, G., Lamb, D. Q., Miknaitis, G., Munn, J. A., Nichol, R., Okamura, S., Pier, J. R., Prada, F., Richards, G. T., Szalay, A., & York, D. G. 2001, AJ, 122, 2833

Farrar, G. R., & Piran, T. 2000, Phys. Rev. Lett., 84, 3527

Feretti, L. 1999, in Diffuse Thermal and Relativistic Plasma in Galaxy Clusters, ed. H. Boehringer, L. Feretti, & P. Schuecker, 3–8

Feretti, L. 2005, Adv. Space Res., 36, 729

Ferrari, C., Govoni, F., Schindler, S., Bykov, A. M., & Rephaeli, Y. 2008, Space Science Reviews, 134, 93

Flower, D. R., & Pineau des Forêts, G. 2003, MNRAS, 341, 1272

Furlanetto, S. R., & Loeb, A. 2001, ApJ, 556, 619

Gardiner, T. A., & Stone, J. M. 2005, Journal of Computational Physics, 205, 509

Glover, S. 2005, Space Science Reviews, 117, 445

Godunov, S. K., Zabrodin, A. V., & Prokopov, G. P. 1961, USSR Computational Math. Math. Phys., 1, 1187

Govoni, F., Murgia, M., Feretti, L., Giovannini, G., Dolag, K., & Taylor, G. B. 2006, A&A, 460, 425

Grasso, D., & Rubinstein, H. R. 2001, Phys. Rep., 348, 163

Greisen, K. 1966, Phys. Rev. Lett., 16, 748

Guidetti, D., Murgia, M., Govoni, F., Parma, P., Gregorini, L., de Ruiter, H. R., Cameron, R. A., & Fanti, R. 2008, A&A, 483, 699

Hallman, E. J., Motl, P. M., Burns, J. O., & Norman, M. L. 2006, ApJ, 648, 852

Harris, D. E., & Grindlay, J. E. 1979, MNRAS, 188, 25

Hawley, J. F., & Balbus, S. A. 1992, ApJ, 400, 595

Heinz, S., Brüggen, M., Young, A., & Levesque, E. 2006, MNRAS, 373, L65

Hockney, R., & Eastwood, J. 1985, Computer Simulation Using Particles (McGraw Hill, New York)

Hoyle, F. 1969, Nature, 223, 936

Iapichino, L., & Niemeyer, J. C. 2008, MNRAS, 388, 1089

Jedamzik, K., Katalinić, V., & Olinto, A. V. 2000, Phys. Rev. Lett., 85, 700

Jena, T., Norman, M. L., Tytler, D., Kirkman, D., Suzuki, N., Chapman, A., Melis, C., Paschos, P., O'Shea, B., So, G., Lubin, D., Lin, W.-C., Reimers, D., Janknecht, E., & Fechner, C. 2005, MNRAS, 361, 70

Jones, T. W., & De Young, D. S. 2005, ApJ, 624, 586

Kritsuk, A. G., & Norman, M. L. 2002, ApJ, 569, L127

—. 2004, ApJ, 601, L55

Kritsuk, A. G., Norman, M. L., & Padoan, P. 2006, ApJ, 638, L25

Kronberg, P. P. 1996, Space Science Reviews, 75, 387

Kronberg, P. P., Bernet, M. L., Miniati, F., Lilly, S. J., Short, M. B., & Higdon, D. M. 2008, ApJ, 676, 70

Kronberg, P. P., Dufton, Q. W., Li, H., & Colgate, S. A. 2001, ApJ, 560, 178

Kulsrud, R. M. 2005, Plasma Physics for Astrophysics (Princeton University Press, Princeton)

Kulsrud, R. M., & Anderson, S. W. 1992, ApJ, 396, 606

Kulsrud, R. M., Cen, R., Ostriker, J. P., & Ryu, D. 1997, ApJ, 480, 481

Large, M. I., Mathewson, D. S., & Haslam, C. G. T. 1959, Nature, 183, 1663

Li, H., Lapenta, G., Finn, J. M., Li, S., & Colgate, S. A. 2006, ApJ, 643, 92

Li, H., Lovelace, R. V. E., Finn, J. M., & Colgate, S. A. 2001, ApJ, 561, 915

Li, S. 2005, Journal of Computational Physics, 203, 344

Li, S., Li, H., & Cen, R. 2008, ApJS, 174, 1

Li, S., & Liu, W. 2004, Meshfree Particle Methods (Springer, Berlin Heidelberg)

Loken, C., Norman, M. L., Nelson, E., Burns, J., Bryan, G. L., & Motl, P. 2002, ApJ, 579, 571

Lovelace, R. V. E. 1976, Nature, 262, 649

Lynden-Bell, D. 1996, MNRAS, 279, 389

Machida, M. N., Matsumoto, T., & Inutsuka, S.-i. 2008, ApJ, 685, 690

Machida, M. N., Omukai, K., Matsumoto, T., & Inutsuka, S.-i. 2006, ApJ, 647, L1

Maki, H., & Susa, H. 2007, PASJ, 59, 787

McNamara, B. R., & Nulsen, P. E. J. 2007, ARA&A, 45, 117

McNamara, B. R., Nulsen, P. E. J., Wise, M. W., Rafferty, D. A., Carilli, C., Sarazin, C. L., & Blanton, E. L. 2005, Nature, 433, 45

McNamara, B. R., Wise, M., Nulsen, P. E. J., David, L. P., Sarazin, C. L., Bautz, M., Markevitch, M., Vikhlinin, A., Forman, W. R., Jones, C., & Harris, D. E. 2000, ApJ, 534, L135

Mignone, A. 2007, Journal of Computational Physics, 225, 1427

Miyoshi, T., & Kusano, K. 2005, AGU Fall Meeting Abstracts, B1295

Motl, P. M., Burns, J. O., Loken, C., Norman, M. L., & Bryan, G. 2004, ApJ, 606, 635

Nakamura, M., Li, H., & Li, S. 2006, ApJ, 652, 1059

Narayan, R., & Medvedev, M. V. 2001, ApJ, 562, L129

Navarro, J. F., Frenk, C. S., & White, S. D. M. 1996, ApJ, 462, 563

Norman, M. L. 2005, in Background Microwave Radiation and Intracluster Cosmology, ed. F. Melchiorri & Y. Rephaeli, 1–33

Norman, M. L., Bryan, G. L., Harkness, R., Bordner, J., Reynolds, D., O'Shea, B., & Wagner, R. 2007, ArXiv e-prints: 0705.1556

Norman, M. L., Burns, J. O., & Sulkanen, M. E. 1988, Nature, 335, 146

Nulsen, P. E. J., David, L. P., McNamara, B. R., Jones, C., Forman, W. R., & Wise, M. 2002, ApJ, 568, 163

Nulsen, P. E. J., McNamara, B. R., Wise, M. W., & David, L. P. 2005, ApJ, 628, 629

Omma, H., Binney, J., Bryan, G., & Slyz, A. 2004, MNRAS, 348, 1105

Orszag, S. A., & Tang, C.-M. 1979, Journal of Fluid Mechanics, 90, 129

O'Shea, B. W., Abel, T., Whalen, D., & Norman, M. L. 2005, ApJ, 628, L5

O'Shea, B. W., & Norman, M. L. 2007, ApJ, 654, 66

Peterson, J. R., Kahn, S. M., Paerels, F. B. S., Kaastra, J. S., Tamura, T., Bleeker, J. A. M., Ferrigno, C., & Jernigan, J. G. 2003, ApJ, 590, 207

Powell, K. G., Roe, P. L., Linde, T. J., Gombosi, T. I., & de Zeeuw, D. L. 1999, Journal of Computational Physics, 154, 284

Pudritz, R. E., & Silk, J. 1989, ApJ, 342, 650

Quashnock, J. M., Loeb, A., & Spergel, D. N. 1989, ApJ, 344, L49

Quilis, V., Bower, R. G., & Balogh, M. L. 2001, MNRAS, 328, 1091

Rees, M. J. 1987, QJRAS, 28, 197

Rephaeli, Y. 1988, Comments on Astrophysics, 12, 265

Rephaeli, Y., Gruber, D. E., & Rothschild, R. E. 1987, ApJ, 320, 139

Reynolds, C. S., Heinz, S., & Begelman, M. C. 2001, ApJ, 549, L179

Reynolds, C. S., McKernan, B., Fabian, A. C., Stone, J. M., & Vernaleo, J. C. 2005, MNRAS, 357, 242

Roettiger, K., Stone, J. M., & Burns, J. O. 1999, ApJ, 518, 594

Ryu, D., Kang, H., Cho, J., & Das, S. 2008, Science, 320, 909

Ryu, D., Ostriker, J. P., Kang, H., & Cen, R. 1993, ApJ, 414, 1

Silk, J., & Langer, M. 2006, MNRAS, 371, 444

Spergel, D. N., Bean, R., Doré, O., Nolta, M. R., Bennett, C. L., Dunkley, J., Hinshaw, G., Jarosik, N., Komatsu, E., Page, L., Peiris, H. V., Verde, L., Halpern, M., Hill, R. S., Kogut, A., Limon, M., Meyer, S. S., Odegard, N., Tucker, G. S., Weiland, J. L., Wollack, E., & Wright, E. L. 2007, ApJS, 170, 377

Spitzer, L. 1962, The Physics of Fully Ionized Gases (Intersci., New York)

Stone, J. M. 2007, Scholarpedia, 2, 2419

Tamura, T., Kaastra, J. S., Peterson, J. R., Paerels, F. B. S., Mittaz, J. P. D., Trudolyubov, S. P., Stewart, G., Fabian, A. C., Mushotzky, R. F., Lumb, D. H., & Ikebe, Y. 2001, A&A, 365, L87

Tan, J. C., & Blackman, E. G. 2004, ApJ, 603, 401

Tan, J. C., & McKee, C. F. 2004, ApJ, 603, 383

Taylor, G. B., & Perley, R. A. 1993, ApJ, 416, 554

Tucker, W., & David, L. P. 1997, ApJ, 484, 602

Turk, M. J., Abel, T., & O'Shea, B. W. 2008, in American Institute of Physics Conference Series, Vol. 990, First Stars III, 16–20

Turner, M. S., & Widrow, L. M. 1988, Phys. Rev. D, 37, 3428

Vernaleo, J. C., & Reynolds, C. S. 2006, ApJ, 645, 83

Vikhlinin, A., Markevitch, M., Forman, W., & Jones, C. 2001a, ApJ, 555, L87

Vikhlinin, A., Markevitch, M., & Murray, S. S. 2001b, ApJ, 549, L47

Vogt, C., & Enßlin, T. A. 2003, A&A, 412, 373

—. 2005, A&A, 434, 67

Voit, G. M. 2005, Rev. Mod. Phys., 77, 207

Widrow, L. M. 2002, Rev. Mod. Phys., 74, 775

Willson, M. A. G. 1970, MNRAS, 151, 1

Wolfe, A. M., Jorgenson, R. A., Robishaw, T., Heiles, C., & Prochaska, J. X. 2008, Nature, 455, 638

Xu, H., Li, H., Collins, D., Li, S., & Norman, M. L. 2008a, ApJ, 681, L61

Xu, H., O'Shea, B. W., Collins, D. C., Norman, M. L., Li, H., & Li, S. 2008b, ApJ, 688, L57

Yoshida, N., Abel, T., Hernquist, L., & Sugiyama, N. 2003, ApJ, 592, 645

Zatsepin, G. T., & Kuz'min, V. A. 1966, Soviet Journal of Experimental and Theoretical Physics Letters, 4, 78

Zweibel, E. G. 1988, ApJ, 329, L1